

BOUNDARY INTEGRAL METHOD AND APPLICATIONS FOR CHAOTIC  
OPTICAL MICROCAVITIES

by

KAHLI R. BURKE

A DISSERTATION

Presented to the Department of Physics  
and the Graduate School of the University of Oregon  
in partial fulfillment of the requirements  
for the degree of  
Doctor of Philosophy

June 2020

DISSERTATION APPROVAL PAGE

Student: Kahli R. Burke

Title: Boundary Integral Method and Applications for Chaotic Optical Microcavities

This dissertation has been accepted and approved in partial fulfillment of the requirements for the Doctor of Philosophy degree in the Department of Physics by:

Daniel Steck	Chair
Jens Nöckel	Advisor
Benjamin McMorran	Core Member
Marina Guenza	Core Member

and

Kate Mondloch	Vice Provost and Dean of the Graduate School
---------------	--

Original approval signatures are on file with the University of Oregon Graduate School.

Degree awarded June 2020

© 2020 Kahli R. Burke

This work is licensed under a Creative Commons  
**Attribution-NonCommercial-NoDerivs (United States) License.**



## DISSERTATION ABSTRACT

Kahli R. Burke

Doctor of Philosophy

Department of Physics

June 2020

Title: Boundary Integral Method and Applications for Chaotic Optical Microcavities

Optical microcavities offer many application possibilities in addition to being model systems for studying chaotic dynamics in the wave regime. However these systems are only analytically solvable for the simplest geometries. In order to study strongly deformed geometries, numerical methods must be used. The open nature of cavities results in complex wavenumbers for their quasi-bound modes which makes finding resonances more difficult. We discuss the main methods available for understanding these resonances.

We implement a numerical package for finding resonances, computing their spatial field patterns and projecting onto surface of section plots via Husimi distributions. This software has been implemented in Julia, a modern programming language with performance and ease of use in mind. This software is available as open source, and is designed to be reusable for arbitrary two dimensional geometries.

Using this package we describe a novel phenomenon that can occur in strongly deformed geometries with concavities, which we name folded chaotic whispering-gallery modes. In these cavities, folded chaotic WGMs allow for



high-Q modes suitable for spectroscopy or laser applications with an important innovation, the ability to attach waveguides to the cavity. The similarities to WGMs are surprising given a theorem by Mather which rules out their existence in the ray picture. High-Q resonances occur within certain wavelength windows and we investigate the peak structure in the spectrum. The periodic orbits in the corresponding billiard system are unstable and exist within the chaotic region of phase space. The fact that such high-Q modes exist based around these orbits implies a form of wave localization.

Another geometry is investigated, deformed boundaries of constant width. These are smooth curves similar to Reuleaux polygons. They have no symmetry axis, and in the ray picture have a unidirectional nature. We investigate these in open optical cavities. We find that nearly degenerate modes of opposite rotational direction can be simultaneously present, but have emission at different boundary locations. This suggests a non-reciprocal process achieved through purely geometric means which may allow for the separation of chiral components of light and applications such as optical microdiodes.

## CURRICULUM VITAE

NAME OF AUTHOR: Kahli R. Burke

GRADUATE AND UNDERGRADUATE SCHOOLS ATTENDED:  
University of Oregon, Eugene, OR

DEGREES AWARDED:  
Doctor of Philosophy, Physics, 2020, University of Oregon  
Bachelor of Science, Physics, 2013, University of Oregon

AREAS OF SPECIAL INTEREST:  
Optical Microcavities, Nonlinear Dynamics

PROFESSIONAL EXPERIENCE:  
Owner, Wintermute Systems, Software Engineering, 2005-Present

PUBLICATIONS:  
Burke, Kahli and Nöckel, Jens U. (2019). Folded chaotic whispering-gallery modes in nonconvex, waveguide-coupled planar optical microresonators. *Physical Review A*, 100, 7–20.

## ACKNOWLEDGEMENTS

I would like to extend my gratitude to my advisor Jens Nöckel whose expertise and patient assistance has been invaluable in performing this research. Many thanks to Dan Steck whose reading course on nonlinear dynamics motivated me to learn more about this fascinating subject, the ideas presented have helped me in the course of my research. In addition I thank the physics faculty at the University of Oregon and my graduate student colleagues whom have been a pleasure to work and study with. Finally, I thank my parents Gary and Penny Burke who supported and encouraged my love of science and computers from a young age and helped me to achieve my goals.

## TABLE OF CONTENTS

Chapter		Page
I.	INTRODUCTION . . . . .	1
II.	OPTICAL MICROCAVITY MODES . . . . .	5
	2.1. Modes of the Circular Dielectric Cavity . . . . .	5
	2.2. Whispering-Gallery Modes . . . . .	10
	2.3. Visualization of Whispering-Gallery Modes . . . . .	12
	2.4. Methods for Semiclassical Treatment of Optical Cavities . . . . .	13
III.	BOUNDARY INTEGRAL METHOD IMPLEMENTATION . . . . .	24
	3.1. Time Domain Methods . . . . .	24
	3.2. Boundary Integral Method . . . . .	27
	3.3. Implementation of BIEs in Julia . . . . .	33
IV.	FOLDED CHAOTIC WHISPERING-GALLERY MODES . . . . .	49
	4.1. Cavity shape and ray phase space . . . . .	55
	4.2. Wave calculations . . . . .	57
	4.3. Discussion . . . . .	64
	4.4. Conclusions . . . . .	72

Chapter	Page
V. CONSTANT WIDTH CAVITIES . . . . .	75
5.1. Introduction . . . . .	75
5.2. Constant Width Cavity in Wave Regime . . . . .	77
5.3. Non-Reciprocity and Time-Reversal Symmetry . . . . .	79
5.4. Constant Width Optical Microcavities . . . . .	84
5.5. Deformation From Constant Width . . . . .	86
5.6. Spatial Pattern and Far Field Response . . . . .	91
5.7. Conclusion . . . . .	92
VI. CONCLUSION . . . . .	95
REFERENCES CITED . . . . .	99

## LIST OF FIGURES

Figure	Page
2.1. Scanning electron microscope image of optical microdisc from microfluidics experiments [3] . . . . .	6
2.2. Visualization of whispering gallery modes for circular cavity of $r = 1$ , $n = 1.5$ . (a, b, c) show the real part of the electric field intensity. (d, e, f) show the absolute value of the electric field intensity, highlighting the isotropic nature of emission. (g, h, i) show the absolute value of a superposition of modes with angular momentum $\pm m$ , highlighting the interference pattern that appears for the degenerate states with equal energy. . . . .	14
2.3. (a) Typical trajectory for circular billiard. (b) SOS for circular billiard showing typical trajectories in phase space . . . . .	16
2.4. (a) 6 bounce orbit with $\chi = \frac{2}{3}\pi$ . (b) SOS showing 6 bounce orbit . . . . .	17
2.5. (a) Quadrupole ( $\epsilon = 0.2$ ) showing typical trajectory in chaotic region. (b) SOS showing regions of stability surrounded by the chaotic sea. . . . .	18
2.6. (a) Elliptical cavity and typical WGM like trajectory. (b) SOS showing invariant curves of the ellipse. The shaded region shows the region that does not satisfy $\sin\chi > 1/n$ , $n = 1.5$ . This region does not support long lived resonances, only invariant curves that are entirely outside this region will support high-Q modes. . . . .	20
2.7. (a) Numerically computed resonance for the circular cavity with $k \simeq 23$ , $n = 1.5$ . (b) Husimi distribution for this resonance, note that there is energy in both the positive and negative halves of the SOS, which correspond to the degenerate modes with $m = \pm 30$ . . . . .	21
2.8. Husimi distributions for the resonance in Fig. 2.7. (a) $\rho = 1$ (b) $\rho = 50$ . . . . .	22
2.9. Husimi distributions for the elliptical cavity. (a) WGM resonance spatial intensity (b) $\rho = 5$ (c) $\rho = 1$ (d) $\rho = 10$ . . . . .	23
3.1. Green's function Eq. (3.2) plotted in complex plane. Note singularity at origin. . . . .	31

Figure	Page
3.2. Error vs. discretization for circular cavity resonance $m = 30, \nu = 0, k \simeq 23$ , showing exponential convergence. . . . .	41
4.1. Spatial structure of a folded chaotic whispering-gallery mode (insets), and Q factor of the mode versus deformation parameter $\epsilon$ at refractive index $n = 2.4$ . The resonator deformation is defined in Eq. (4.2); attached waveguides of finite lengths are shown horizontal; their lengths are slightly unequal to remove reflection symmetry. False color represents field intensity. The real part of $k$ (not shown) decreases approximately linearly from 14 to 12.5 as $\epsilon$ increases. . . . .	52
4.2. Poincaré surface of section with the curve parameter $\phi$ as position and $\sin \chi$ as momentum variable. Here, $\chi$ is the angle between incident rays and the surface normal, so that $\sin \chi = 1$ corresponds to grazing incidence. Ray trajectories show up as point clouds in the chaotic sea, or as one-dimensional lines for regular motion. The only regular regions are created by bouncing-ball orbits (top left); there are no invariant curves in the whispering-gallery region near $\sin \chi \rightarrow 1$ . Shaded boxes indicate the intervals of $\phi$ which describe the attached waveguides. Rays entering these regions will escape the resonator. The thin horizontal lines mark the critical angle for total internal reflection, $ \sin \chi_c  = 1/n$ . Here and in all subsequent results, $n$ can be viewed as the interior refractive index while the exterior refractive index is unity. Arrows identify the real-space orbits belonging to specific points in the Poincaré section. . .	54
4.3. (a-c): Two self-intersecting unstable periodic orbits with angles of incidence $\sin \chi \geq 0.6$ in the billiard shape given by Eq. (4.2) with $\epsilon = 0.43$ . The lengths $L_1, L_2$ of the orbits are slightly different. The same topology of orbits persists for a wide range of deformations. (c) is obtained from (b) by adjusting the initial conditions to generate eight instead of three reflections in the top half. For the rectangular unstable periodic orbit in (d), the increasing proximity to the corners of the waveguide aperture is illustrated for increasing $\epsilon$ . (e) A ray trajectory launched in the cavity (green dot) and escaping through the waveguide opening (red dot). It retains the folded character of the orbits in (a), (b) for a short time. . . . .	56
4.4. Small-cavity limit of the folded chaotic WGM, showing only low Q factors as the transverse width of the mode is comparable to the cavity size. Below $k \approx 7$ , the wavelength is too long to observe the WGM like concentration of intensity near the top and bottom of the cavity. The horizontal waveguide stubs are attached in a way that smoothly	

- matches the shape given by Eq. (4.2) for the vertical lobes. The refractive index is  $n = 2.4$  inside and  $n = 1$  outside, and the vertical lobes are described by Eq. (4.2) with  $\varepsilon = 0.444$ . In this and the following plots, one can discern even and odd parity with respect to reflections at the horizontal axis. Although we intentionally break reflection symmetry across the vertical axis by making the horizontal waveguide lengths unequal, the modes still show approximate antinodes (left) or nodal lines (right) along the vertical axis. This is because the cavity supporting most of the intensity is still left-right symmetric. . . . 58
- 4.5. Wavenumber sweeps of the Q factor for different refractive indices  $n$ , discarding low-Q modes with  $\kappa \geq 0.05$  (for  $n = 1.6$ , only modes with  $\kappa \geq 0.2$  are shown). The deformation is  $\varepsilon = 0.444$ . The appearance of distinct Q-factor peaks as a function of quasi-bound state wavenumber is most pronounced at the largest refractive index,  $n = 2.4$ , and becomes nearly unobservable at  $n = 1.6$  (therefore, data for  $n = 1.6$  were not collected beyond  $nk \approx 106.5$ ). The peaks that do remain observable are approximately at the same values of  $nk$  for all  $n$ . . . . . 59
- 4.6. Q-factor scan versus interior wave number at deformation  $\varepsilon = 0.52$  and refractive index  $n = 2.4$ , showing modes with decay rate  $\kappa < 0.05$ . . . . 61
- 4.7. Field intensities for the modes corresponding to the first four Q-factor peaks in Fig. 4.5 at  $n = 2.4$ ,  $\varepsilon = 0.444$ . . . . . 62
- 4.8. Field intensities for folded WGMs at different deformations: (a)  $\varepsilon = 0.52$ , (b)  $\varepsilon = 0.6$ , (c)  $\varepsilon = 0.7$ . The refractive index is  $n = 2.4$ . In (c), a smaller wavenumber is chosen, whereas (a) and (b) have comparable wavenumbers. The narrowing of the horizontal stubs is a result of the requirement that its tangents must match the curve described by Eq. (4.2) at the corners. . . . . 63
- 4.9. (a) Folded chaotic whispering-gallery mode as obtained in a finite-difference time domain computation for the same deformation  $\varepsilon = 0.444$  and refractive index  $n = 2.4$  shown in Fig. 4.5. The wave number corresponds to the top of the first Q-factor peak,  $k \approx 13.6$  ( $Q = 2612$ ). Waveguide and resonator structure are underlaid as green shading, and the false-color scale represents the electric field. (b) Same deformation and refractive index, but approximately ten times shorter wavelength,  $k \approx 116.0$  and  $Q = 9898$ . (b) is discussed in section 4.3. . . . . 64
- 4.10. Two different modes with thinner waveguides, obtained by introducing a vertical offset between the two lobes of Eq. (4.2) and adjusting  $\varepsilon$  to



Figure	Page
<p>match them smoothly to the horizontal waveguides. The refractive index is <math>n = 2.4</math>. In (a) <math>k \approx 13.3</math> and <math>Q \approx 1580</math>, in (b) <math>k \approx 22.4</math> and <math>Q \approx 2550</math>. . . . .</p>	65
<p>4.11. (a) Stable and unstable manifolds around an unstable periodic orbit. The zoomed-in region shown in (a) corresponds to the top left quadrant of the Husimi projection in (b). The real-space wave intensity of the mode in (b) is shown in the inset to (a). It is obtained for <math>n = 2.4</math> and <math>\epsilon = 0.444</math>. Shaded regions in (b) mark the waveguides, which were treated as escape windows in (a). Refractive escape is not considered in the ray simulation for (a), to get a more complete picture of the manifolds. Note the similarity in shape between the phase space structure and the areas of large Husimi weight. . . . .</p>	67
<p>4.12. Comparison of Husimi plots for the same states shown in Fig. 4.8. Only the positive-sin <math>\chi</math> half of the phase space is displayed. The low wavenumber (<math>k \approx 17.2</math>) in (c) leads to lower phase-space resolution than in (a) and (b) where <math>k \approx 31.4</math> and <math>k \approx 31.2</math>. . . . .</p>	69
<p>5.1. Reuleaux triangle . . . . .</p>	76
<p>5.2. Smooth curve of constant width based on Eq. (5.1) . . . . .</p>	76
<p>5.3. (a) Curve of constant width and typical chaotic trajectory. (b) SOS for the shape. . . . .</p>	78
<p>5.4. (a) Typical bouncing ball trajectory (b) SOS in the KAM barrier region for bouncing ball orbits. . . . .</p>	78
<p>5.5. Mode families for the constant width cavity (a) Barrier KAM mode (b) WGM mode (c) Island mode (d) Hybrid mode . . . . .</p>	80
<p>5.6. Husimi distribution for the mode families for the constant width cavity, corresponding to the modes in Fig. 5.5 (a) Barrier KAM mode (b) WGM mode (c) Island mode (d) Hybrid mode . . . . .</p>	81
<p>5.7. Wave functions and Husimi distributions for quasi-degenerate doublet at <math>k \simeq 45.73</math> . . . . .</p>	86
<p>5.8. Wavefunctions and Husimi distributions for superpositions of modes from Figure 5.7 with phase factors <math>\phi = i</math> in (a), (c), <math>\phi = -i</math> in (b), (d). . . . .</p>	87
<p>5.9. SOS for vertical deformation of constant width billiard. (a) <math>\eta = -0.001</math> (b) <math>\eta = -0.02</math> . . . . .</p>	87

Figure	Page
5.10. Combined plot of Husimi imbalance for each mode in the doublet, the mode overlap and difference in wavenumber as a function of deformation parameter $\eta$ . . . . .	89
5.11. Wave functions and Husimi distributions for deformed cavity with $\eta = -0.038$ . Both modes in doublet show increased weight in the anti-clockwise chiral mode. . .	90
5.12. Far field response for chiral modes in the doublet resonance with $k \simeq 45.73 - 0.068i$ . . . . .	92

## CHAPTER I

### INTRODUCTION

Optical microcavities are tiny structures that provide both tantalizing application possibilities and a rich testbed for the exploration of chaotic dynamics in the wave regime. They have a long history, having been extensively studied from the 1990s to the present. Interest in these structures continues as we expand our ability to control the coupling of light inside and outside the cavity. By altering the geometry and material of optical microcavities, a diverse set of resonance patterns and behavior can be achieved.

The key feature of an optical microcavity is the ability to trap light energy inside via long-lived quasibound resonances. These resonances are peaked at specific frequencies due to interference effects and since the size of these systems is on the order of a few wavelength, the spacing of individual resonances is much larger than would be found in a macroscopic optical cavity, e.g. a Fabry–Pérot cavity employed as a laser or interferometer[1]. Because optical microcavities are open systems, i.e. they allow light energy in and out, resonances can be characterized by their lifetime. This is typically expressed by the “quality factor”  $Q$  and is one of the main figures of merit for a cavity. The resonant wavenumber can be expressed as a complex number  $k_{res} = k - i\kappa$ , where the imaginary part determines the time dependent decay factor of an oscillating wave,  $e^{ik_{res}\vec{x}} = e^{-\kappa t} e^{-ik\vec{x}}$ . Then the quality factor is defined as

$$Q = \frac{k}{2\kappa}. \tag{1.1}$$

When studying the behavior of optical microcavities, small changes in the geometry of the cavity have large effects. Since manufacturing all possible variations is impractical, we would like to have methods for predicting and modeling their behavior which can inform our understanding and allow us to develop applications. In many settings, Maxwell's equations, Eq. (1.2), provide the basic tools for understanding the dynamics of the electromagnetic fields inside the cavities and how they couple to the outside world. So in principle, it is simply a matter of solving these equations for whatever cavity design we imagine. Maxwell's equations will then tell us the resonant frequencies, time-dependent behavior and spatial field intensities

$$\begin{aligned}
 \nabla \cdot \vec{E} &= \frac{\rho}{\epsilon_0} \\
 \nabla \cdot \vec{B} &= 0 \\
 \nabla \times \vec{E} &= -\frac{\partial \vec{B}}{\partial t} \\
 \nabla \times \vec{B} &= \mu_0 \vec{J} + \epsilon_0 \frac{\partial \vec{E}}{\partial t}.
 \end{aligned}
 \tag{1.2}$$

However, Maxwell's equations are a set of coupled partial differential equations that have analytic solutions in only the simplest of geometries. As in many areas of physics, it is possible to determine behavior for simple three-dimensional shapes like spheres and two-dimensional shapes such as circles, and rectangles. The main reason for the success in these cases is that the differential equations become *separable* and can be solved as ODEs for the respective coordinate parameters. This separability breaks down when the symmetries in these special cases is broken. It is possible to understand the behavior for small

deformations as an expansion in perturbation theory, but for large deformations perturbation theory breaks down. Especially in strongly deformed cavities such as those with concavities, methods are needed to solve these equations numerically.

Several methods have been developed for solving Maxwell's equations in a numeric, discretized form. These can be divided into methods that attempt to solve the equations in the time-domain and those that attempt to solve the equations in the frequency-domain. While both approaches have their merits, frequency-domain methods have some decided advantages when the goal of a solution is to understand the frequency dependent response of the system, where the resonances exist, and the overall spectrum. Since the methods are distinct in their approach, they serve as a good cross-check for each other.

In this thesis, we describe an implementation of the Boundary Integral Method (BIM), a frequency-domain method for finding the resonant frequencies and lifetimes of resonances. The implementation we describe is suitable for pseudo two-dimensional cavities, those that are planar in nature with small vertical extent. These systems are useful because two-dimensional fabrication techniques are used widely in the manufacturing of semiconductors and other integrated microelectronics. The package is written in the Julia programming language and is designed to allow any two-dimensional shape to be used. This package was developed using an implementation of the BIM described by P. Heider [2] and uses a singularity subtraction method that provides exponential convergence for the number of discretized points. This is important because the matrices used by BIM are fully populated and the number of calculations scales as  $O(N^2)$ . The software is provided as open source

(<https://github.com/kahliburke/BoundaryIntegralMethod.jl>) and we hope that others may find it useful.

Chapter 2 describes some preliminary technical background on two-dimensional cavities, whispering-gallery modes, and tools from the field of chaotic billiards that can be used to understand the semi-classical behavior of cavities which can predict or enhance the understanding of behavior in the wave regime.

Chapter 3 describes the implementation of the BIM and details some lessons learned along the way. It also contains some corrections to the original paper by Heider and clarifies some ambiguities in the description of the BIM equations. The hyper-singular nature of the BIM Green's functions requires some special treatment and these points are elucidated.

Chapter 4 describes the use of this software to discover and describe a novel phenomenon which we name “folded chaotic whispering-gallery modes”, which allow the connection of high-Q resonators with an important innovation, the ability to attach waveguides as input/output channels.

Chapter 5 describes an additional investigation using the BIM software, this one for a Reuleaux boundary, a curve of constant width with no rotational symmetry. We describe how this shape can separate the left and right chiral components of light which allows for a non-reciprocal optical cavity. We propose this may allow for the creation of an optical micro-diode.

## CHAPTER II

### OPTICAL MICROCAVITY MODES

#### 2.1. Modes of the Circular Dielectric Cavity

It is instructive in the theory of optical microcavities, as in other areas of physics, to explore the simplest systems first. By doing so, we gain an understanding of some of the fundamental properties of the more complex systems we hope to understand. Therefore this chapter serves as an introduction to the simplest of planar optical cavities, a circular disk made of a dielectric material such as glass. We assume that the cavity has a small extent vertically and can be treated as a two dimensional geometry with a constant index of refraction inside, which is higher than that of the air or vacuum outside.

An optical cavity such as the one depicted in Fig. 2.1 has a special property that enables a simple solution to its behavior. It has a continuous rotational symmetry which from Noether's theorem implies a conserved quantity [4]. The conserved current in this case is the angular momentum of a photon inside the cavity. Because the angular momentum is conserved, it acts as a good quantum number and partially characterizes the resonances of the circular optical microcavity.

We will assume a TE polarization for the EM field, with the electric field perpendicular to the cavity plane. We can simplify Maxwell's equations in vector form to the scalar Helmholtz equation, where we separate the time dependent field as  $E(x) = e^{-ikt}u(x)$ . Then the Helmholtz equation is

$$\Delta u(x; k) + k^2 n^2(x) u(x; k) = 0. \tag{2.1}$$

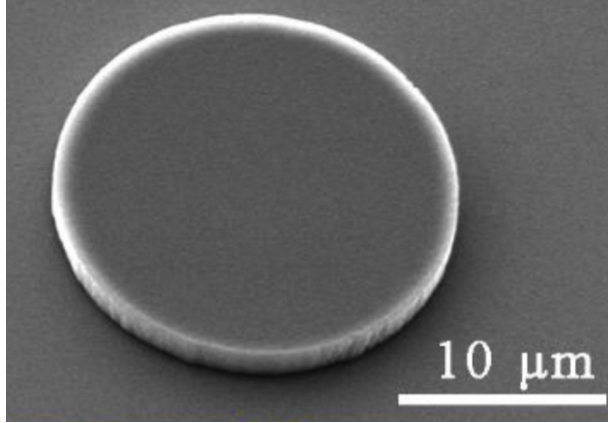


FIGURE 2.1. Scanning electron microscope image of optical microdisc from microfluidics experiments [3]

In addition, we impose the Sommerfeld radiation condition, which provides a direction to the emitted radiation,

$$\lim_{r \rightarrow \infty} \sqrt{r} \left( \frac{\partial u}{\partial r} - iku \right) = 0. \quad (2.2)$$

Eq. (2.2) guarantees that at a large distance the field is an outgoing cylindrical wave [2].

In this system the equation is separable in polar coordinates, which can be solved as in [5],

$$u(x; k) = R(r; k)\Phi(\phi; k).$$

Then the Helmholtz equation can be written as

$$\frac{d^2 R}{dr^2} \Phi + \frac{1}{r} \frac{dR}{dr} \Phi + \frac{1}{r^2} \frac{d^2 \Phi}{d\phi^2} R + k^2 R \Phi = 0.$$

By multiplying both sides by  $r^2/(R\Phi)$ , we get the result

$$\left( \frac{r^2}{R} \frac{d^2 R}{dr^2} + \frac{r}{R} \frac{dR}{dr} + k^2 r^2 \right) + \frac{1}{\Phi} \frac{d^2 \Phi}{d\phi^2} = 0.$$



Then the two parts are separable,

$$\frac{1}{\Phi} \frac{d^2 \Phi}{d\phi^2} = -m^2 \quad (2.3)$$

$$r^2 \frac{d^2 R}{dr^2} + \frac{r}{R} \frac{dR}{dr} + k^2 r^2 = m^2. \quad (2.4)$$

Eq. (2.3) has a periodic solution

$$\Phi(\phi; k) = A_m \cos(m\phi) + B_m \sin(m\phi).$$

Eq. (2.4) is Bessel's differential equation, which has as a solution

$$R(r; k) = C_m J_m(kr) + D_m Y_m(kr),$$

where  $J_m(kr)$  is the Bessel function of the first kind and  $Y_m(kr)$  is the Bessel function of the second kind.

Therefore for the circular optical microcavity the resonant modes may be written as

$$u(r, \phi; k) = \sum_{m=0}^{\infty} (A_m \cos(m\phi) + B_m \sin(m\phi)) \times (C_m J_m(kr) + D_m Y_m(kr)). \quad (2.5)$$

What remains is to use the matching conditions for the electric field inside and outside the cavity in order to fix the general coefficients in Eq. (2.5). The two general conditions in a TM polarized wave are that the electric field intensity and its derivative must be continuous at the interface. In the circular cavity, these

conditions are

$$\begin{aligned} E_{inside}(x) &= E_{outside}(x) \\ \frac{\partial E_{inside}}{\partial r} &= \frac{\partial E_{outside}}{\partial r}. \end{aligned}$$

We assume for the moment (without loss of generality) that the refractive index inside the cavity is  $n$  and outside the cavity is 1 (air or vacuum). Looking at the radial equation inside the cavity, we can eliminate one of the coefficients because  $\lim_{r \rightarrow 0} Y_m(kr) = \infty$ . Therefore,

$$R_{inside}(r; k) = C_m J_m(nkr).$$

It is also helpful to use the Hankel functions instead of the Bessel functions for the field outside the cavity, although they diverge at the origin these functions have well behaved asymptotic behavior far from the origin, and act like incoming ( $H_m^{(1)}$ ) and outgoing ( $H_m^{(2)}$ ) cylindrical waves. Since the resonance can be viewed as an outgoing wave being present without an incoming wave (as to satisfy Eq. (2.2)), we can use only  $H_m^{(1)}$  and

$$R_{outside}(r; k) = D_m H_m^{(1)}(kr).$$

To find a solution that satisfies the matching conditions, we must solve the system of equations

$$\begin{aligned} A_m J_m(nkr) &= B_m H_m^{(1)}(kr) \\ C_m \frac{\partial J_m(nkr)}{\partial r} &= D_m \partial H_m^{(1)}(kr). \end{aligned}$$

In this equation the variables are the values  $A_m B_m, C_m, D_m$ , the coefficients are the Bessel and Hankel functions themselves. A nontrivial solution exists only for special values of  $k$  and a solution to this set of equations is equivalent to finding the non-trivial zeroes of the determinant

$$D = \begin{vmatrix} J_m(nkr) & H_m^{(1)}(kr) \\ \frac{\partial J_m(nkr)}{\partial r} & \frac{\partial H_m^{(1)}(kr)}{\partial r} \end{vmatrix}$$

$$J_m(nkr) \frac{\partial H_m^{(1)}(kr)}{\partial r} - \frac{\partial J_m(nkr)}{\partial r} H_m^{(1)}(kr) = 0.$$

Since the derivatives of the Bessel and Hankel functions satisfy the same recursion relationships for the derivative and for combinations of the functions,

$$\begin{aligned} J_{m-1}(x) + J_{m+1}(x) &= 2J'_m(x) \\ J_{m-1}(x) - J_{m+1}(x) &= \frac{2m}{x} J_m(x), \end{aligned}$$

we can evaluate the derivatives and then eliminate the  $J_{m-1}, H_{m-1}$  functions through the following algebra,

$$\begin{aligned} J_m(nkr) H_m^{(1)}(kr) - J'_m(nkr) H_m^{(1)}(kr) &= 0 \\ J_m(nkr) \frac{1}{2} (H_{m-1}^{(1)}(kr) + H_{m+1}^{(1)}(kr)) \\ - n \frac{1}{2} (J_{m-1}(nkr) + J_{m+1}(nkr)) H_m^{(1)}(kr) &= 0 \\ J_m(nkr) \frac{1}{2} \left( \frac{2m}{kr} H_m^{(1)}(kr) + 2H_{m+1}^{(1)}(kr) \right) \\ - n \frac{1}{2} \left( \frac{2m}{nkr} J_m(nkr) + 2J_{m+1}(nkr) \right) H_m^{(1)}(kr) &= 0 \\ \frac{m}{kr} J_m(nkr) H_m^{(1)}(kr) - \frac{m}{kr} J(nkr) H_m^{(1)}(kr) - n J_{m+1}(nkr) H_m^{(1)}(kr) &= -J_m(nkr) H_{m+1}^{(1)}(kr) \end{aligned}$$

$$nJ_{m+1}(nkr)H_m^{(1)}(kr) = J(nkr)H_{m+1}^{(1)}(kr), \quad (2.6)$$

thus arriving at this transcendental equation in  $k$ . The complex roots of this equation represent resonant wavenumbers  $k$  for the circular dielectric cavity.

## 2.2. Whispering-Gallery Modes

The modes that are found at the resonant frequencies described above are known as whispering-gallery modes (WGMs). First described by Lord Rayleigh in the late 1800s in the case of St. Paul's Cathedral, this phenomenon was noticed in acoustic waves. Sounds that seemed too faint to travel across a large expanse could be heard along the edges of the circular dome of the cathedral. Rayleigh argued that if the sound stayed on the boundary as a series of specularly reflected sound rays, the intensity would fall off as the inverse distance instead of the inverse square distance.

WGMs are, however, a general wave phenomenon and can be observed in optical systems. These modes have attracted a fair amount of attention due to their potential to create very high-Q resonances, effectively trapping light for extended periods of time [6]. Interactions that the light has with the cavity medium and with small objects outside the cavity but near enough to the boundary to interact with the evanescent field are resonantly enhanced, which allows for applications in sensing and spectroscopy.

The resonant condition in the circular cavity allows for solutions that can be described by two quantum numbers,  $m$  being the angular momentum and counting the number of nodes around the circle, and  $\nu$  which counts the number of radial nodes. These modes can exist as both broad and narrow resonances, the condition

separating the two being whether  $m > kr$  (broad) or  $m < kr$  (narrow). It is useful to examine the broad resonances to determine the dependence of the resonance width on the index of refraction.

In the case where  $kr \gg m$ , a large argument expansion of Eq. (2.6) may be used, which can be simplified to

$$\tan(nkr - \frac{\pi}{2}m - \frac{\pi}{4}) = -\frac{i}{n}.$$

This can be solved for the real and imaginary parts of  $kr = x + iy$ , where the imaginary part determines the resonance decay lifetime.

$$\begin{aligned} x &= \frac{\pi}{n}(\frac{m}{2} + l + \frac{1}{4}) \\ y &= \frac{1}{2n} \ln \frac{1 - 1/n}{1 + 1/n}. \end{aligned}$$

The resonance lifetime is independent of the resonance location, and for a large refractive index the logarithm can be expanded to obtain

$$y = -\frac{1}{n^2}.$$

This shows that for large refractive index, the resonance decay becomes vanishingly small. This has an analog with the Fresnel formula for reflections from a dielectric interface, where for a normal incidence the reflection probability is

$$p = \left| \frac{E_{refl}}{E_{incident}} \right|^2 = \frac{(1 - n)^2}{(1 + n)^2},$$

as described in [7].

### 2.3. Visualization of Whispering-Gallery Modes

Figure 2.2 displays a selection of whispering gallery modes for a circular cavity with inside index of refraction  $n = 1.5$  and radius  $r = 1$ . The angular momentum is chosen to be  $m = 30$  in all the resonances. The first column of resonances is for the  $\nu = 0$  mode, while the second and third columns display the  $\nu = 1, 2$  modes, respectively. Note that the quality factor for the  $\nu = 0$  mode is much higher ( $Q \simeq 22000$ ) than for the other modes. This is a general property of WGMs, those that are most tightly confined to the boundary are the narrowest for a given angular momentum. When one additional radial node is present, the quality factor drops precipitously to  $Q \simeq 500$ . Note how tightly the field is contained for the resonances in the first column, there is very little evanescent field leakage.

The rows in the figure display three ways of visualizing the electric field intensity. The first row shows  $\text{Re}(E)$ , here it is possible to see how the Bessel function inside the resonator connects to the Hankel function which behaves like an outgoing cylindrical wave as the distance from the cavity increases. In a time dependent visualization, the nodes and anti-nodes would be seen to oscillate with time dependence  $\exp(-ikt)$ . The second row shows the absolute value of electric field intensity  $\text{abs}(E)$ . Here the isotropic nature of emission can be seen. This is a natural consequence of the rotational symmetry of the system; there can be no angular dependence as such a dependence would break the rotational symmetry. The third row again shows  $\text{abs}(E)$ , however in this case an equal superposition of states with  $m = \pm 30$  is shown. Since the system has rotational symmetry, there exist two degenerate states with equal energy (and wavenumber). Therefore any linear combination of these states satisfies the differential equation just as well as

one or the other singly. They can both be excited simultaneously and in the generic case could both be present. This is worth mentioning because in cases where modes are determined numerically, the most likely case to encounter is a superposition of degenerate states based on the symmetry of the system. In cases where rotational symmetry is broken, but some other mirror symmetry is present, similar solutions of equal and odd parity may present themselves. When visualizing these solutions, it is important to remember that although the emission in the third row appears to have nodes and anti-nodes, this is an artifact of the interference pattern and for a single mode the emission is truly isotropic.

#### 2.4. Methods for Semiclassical Treatment of Optical Cavities

Here we will discuss some methods that have emerged from the study of Hamiltonian systems. In the study of dynamical systems, a particular set of model systems that have been studied extensively since the 1920s are known as dynamical “billiards” [8]. These are (often 2D) closed boundaries with specular reflection laws, where a particle is imagined to travel at a constant velocity with no loss of energy, and reflect off the boundary when colliding with it. As such, they resemble an idealization of a billiards table.

While this classical system may at first glance seem to have little relevance for an optical cavity, it proves to be quite useful in understanding the behavior of the cavity in the limit that  $kr \rightarrow \infty$ , at which point the wave nature of the light becomes less important and the ray approximation becomes justifiable. Since the resonance condition represents a case where the light is confined inside the cavity, in the ray picture we think of the confinement being provided by total internal reflection. As long as the angle the ray keeps with cavity edge is sufficiently close to

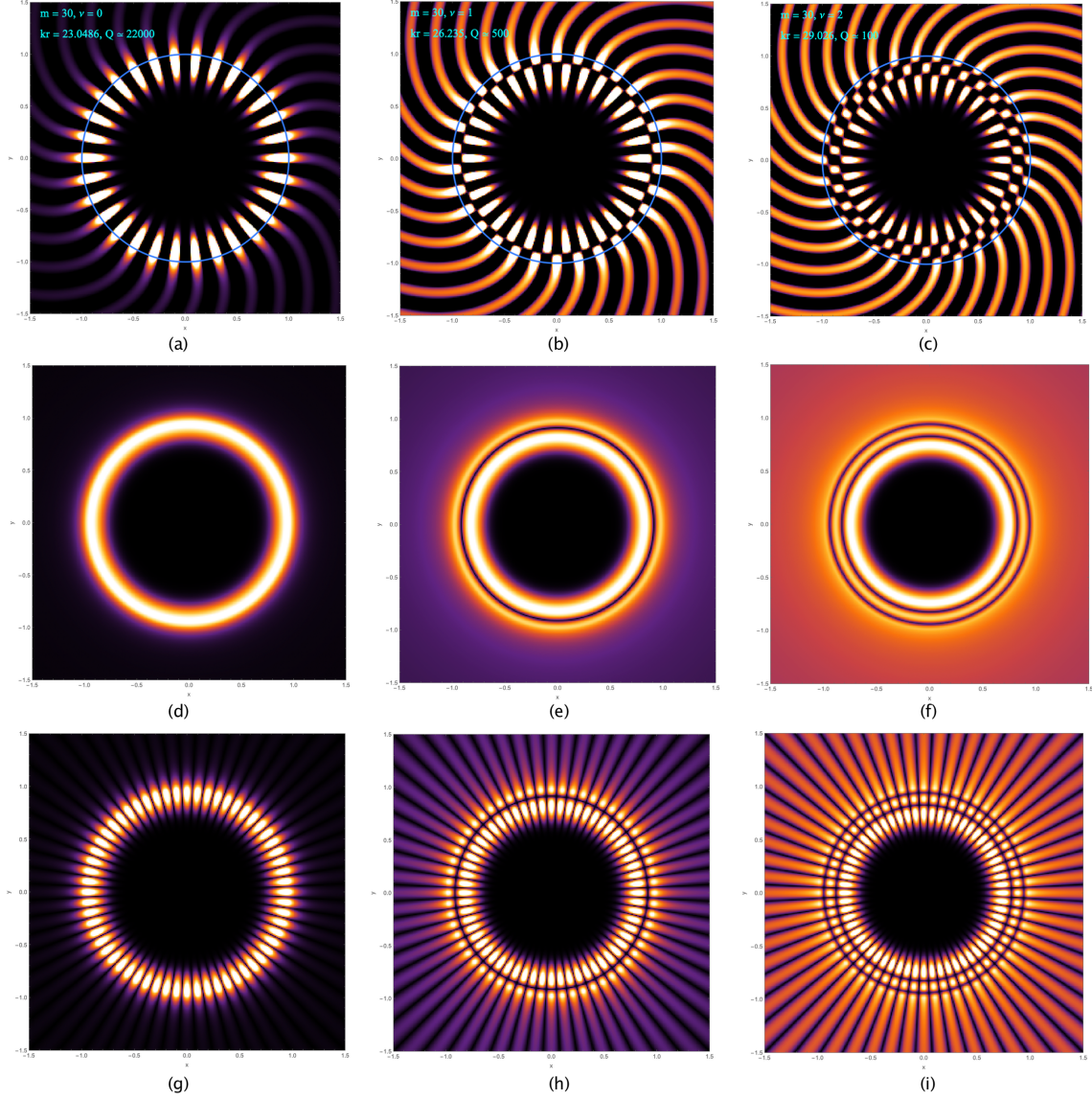


FIGURE 2.2. Visualization of whispering gallery modes for circular cavity of  $r = 1$ ,  $n = 1.5$ . (a, b, c) show the real part of the electric field intensity. (d, e, f) show the absolute value of the electric field intensity, highlighting the isotropic nature of emission. (g, h, i) show the absolute value of a superposition of modes with angular momentum  $\pm m$ , highlighting the interference pattern that appears for the degenerate states with equal energy.



grazing to satisfy the condition of internal reflection

$$\theta > \theta_c = \sin^{-1} \frac{n_{out}}{n_{in}},$$

the light will remain confined inside, with the exception of evanescent leakage which is not accounted for in the ray approximation.

Billiards models have been used to study the behavior of various categories of dynamical systems which can be discerned from one another based on their overall behavior in phase space. This abstract space representing the position and momentum for each degree of freedom can be complicated to visualize and understand. In the case of our two-dimensional billiards table, there are two degrees of freedom, either the  $x, y$  coordinates of the Cartesian plane, or as is more fitting for the circular case the polar coordinates  $r, \phi$ . For each coordinate we need to track two variables, so the phase space of our billiards system is four-dimensional. Since a four-dimensional surface is obviously difficult or impossible to visualize directly, we must find one or more lower dimensional representations.

In the present case, because the motion in the interior of the table is fixed and well defined, it can be ignored completely and instead the system can be understood in a lower dimensional embedding where we track only two variables. The motion of the “ball” only changes when hitting a wall. So the natural pieces of information to keep are the positions of wall bounces, and the angle at which the ball hits the wall. By tracking this information, the complete trajectory of the ball can be reconstructed. We have lost nothing and gained a mapping that is much easier to understand. Such transformations were studied by Poincaré and thus bear the name of Poincaré surface of section (SOS) or Poincaré map [9]. Typically the two coordinates used are the angle  $\phi$  (or alternatively the arc length along the

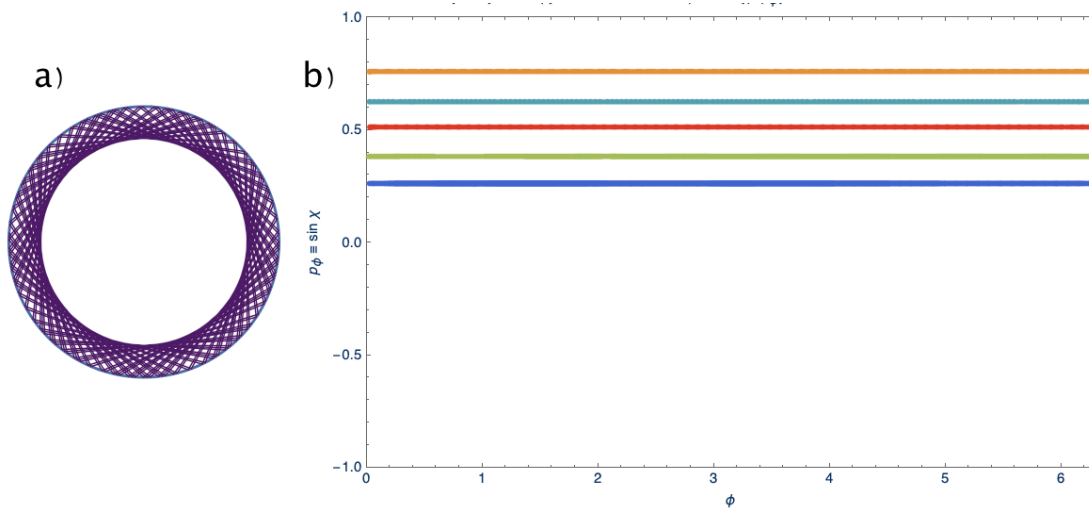


FIGURE 2.3. (a) Typical trajectory for circular billiard. (b) SOS for circular billiard showing typical trajectories in phase space

boundary  $s$ ) and the sine of the angle with respect to the vector normal to the boundary at the point of the bounce  $\sin \chi$ . By starting at any point in phase space and adding a point at each subsequent reflection, we can follow the evolution of a trajectory.

Fig. 2.3 shows such a section and some trajectories for various starting angles. As the figure shows, the trajectories follow horizontal lines in the SOS, due to the conservation of angular momentum. Most starting angles will not close back on themselves after bouncing around the boundary, and will eventually produce a dense set of points along the  $\phi$  axis. There are some special angles that are rational submultiples of  $\pi$ , where  $\chi = \pi K/N$ ,  $K, N$  mutually prime, that will end at the same starting position after  $K \cdot N$  bounces [10]. These produce a trajectory as shown in Fig. 2.4.

The circular cavity is a system with a symmetry that has an analytic solution and simple trajectories in phase space in its billiards analog. These statements are all related by the fact that the circular cavity is an “integrable” system. Such

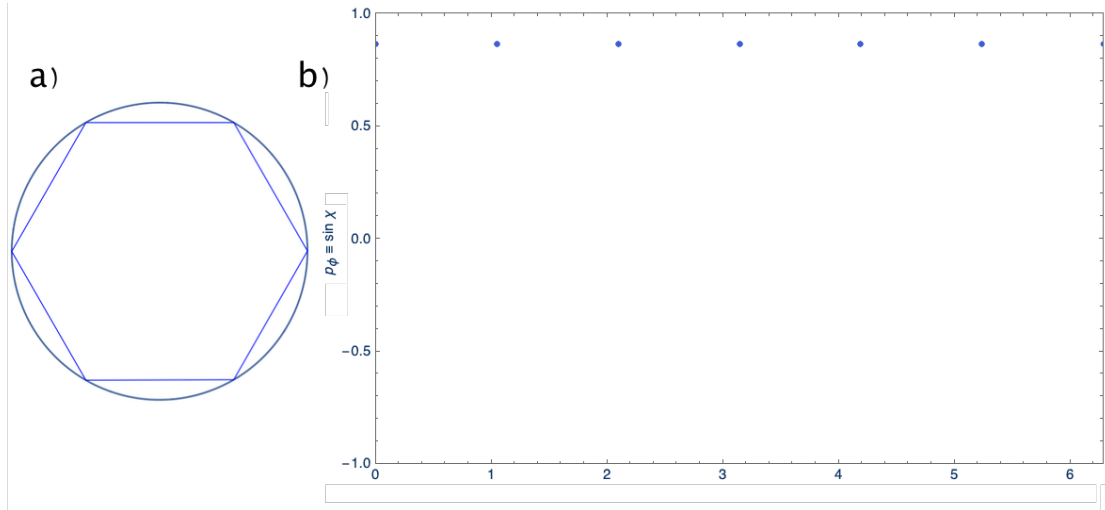


FIGURE 2.4. (a) 6 bounce orbit with  $\chi = \frac{2}{3}\pi$ . (b) SOS showing 6 bounce orbit

systems have a constant of motion (here the angular momentum or  $\sin\chi$ ), which causes the system to follow invariant curves of measure zero in phase space. The trajectory stays confined to these curves and does not spread out over an area or visit the entirety of phase space.

### 2.4.1. Chaotic Dynamics

In reference [10], Berry outlines various deformations of the simple circular billiard and the resulting dynamics. For ellipses, angular momentum is no longer conserved but the system is still integrable and the straight line trajectories of Fig. 2.3 are bent into curves that are nonetheless followed smoothly without diffusion. For the stadium billiard, where two semi circles are connected via a straight line segment, the system becomes non-integrable and the trajectories no longer follow invariant curves but instead chaotically move around. There are no stable orbits for the stadium and almost all trajectories explore the whole phase space. Many systems fall into the middle of these examples and have a mixture of stable orbits, unstable orbits and chaotic regions. As an example of this type of billiard, we can

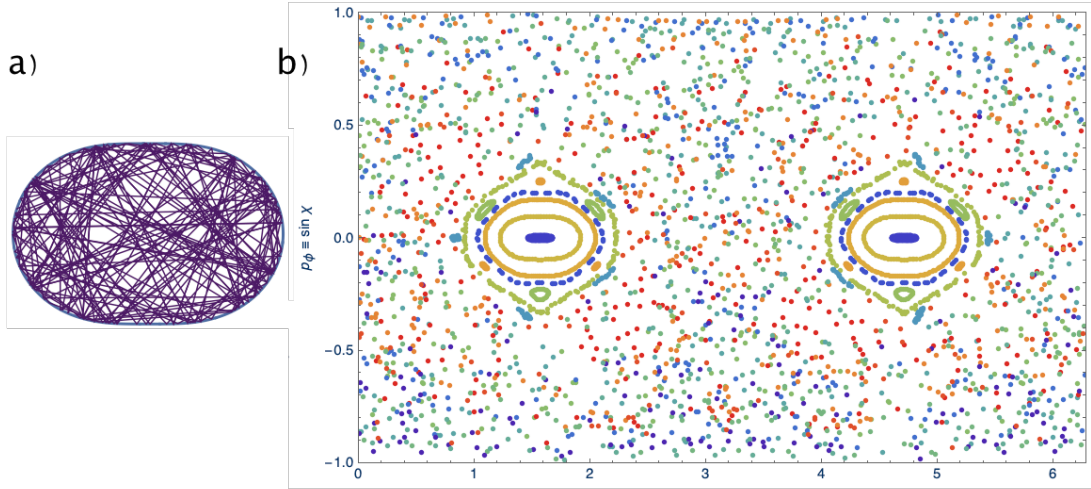


FIGURE 2.5. (a) Quadrupole ( $\epsilon = 0.2$ ) showing typical trajectory in chaotic region. (b) SOS showing regions of stability surrounded by the chaotic sea.

look at a deformation of the circle into a quadrupole, where the radius is no longer constant but instead is defined as

$$r(\phi) = 1 + \epsilon \cos(2\phi).$$

In Fig. 2.5, we see an example of chaotic behavior in phase space. Although there are some orbits that follow stable bouncing ball orbits, most of the phase space is referred to as the chaotic or stochastic sea [11], trajectories that start somewhere in the chaotic sea bounce around unpredictably and pepper the SOS with points that display no clear pattern.

#### 2.4.2. Classical Escape Condition

One way to make a connection between closed billiard systems and open microcavities is made by associating narrow resonances with rays that are trapped via total internal reflection. The condition for this is that  $\sin\chi > 1/n$ . Therefore we

can imagine a cutoff in the SOS where any bounce that lands in the central region of  $\pm 1/n$  leads to the light escaping the cavity. The closed billiards do not know anything about this condition, but we can superimpose this on our understanding of the SOS and see that if there are invariant curves or other structures like stable or unstable periodic orbits, they must exist in the region of the SOS that satisfies the internal reflection condition in order to produce a narrow resonance in the open system.

Figure 2.6 illustrates this principle for the elliptical billiard. Plotted on the SOS are invariant curves associated with the resonances of the corresponding optical cavity. This system is integrable like the circular cavity, but angular momentum is not a conserved quantity because the rotational symmetry is broken. For any curve that starts outside the shaded region, if on successive bounces it enters the shaded region, we would expect the light to escape the cavity. Therefore if the goal is to find narrow resonances, we should look for the structures in the SOS that exist outside the region of refractive escape.

### 2.4.3. Husimi Distributions

Given that the billiards picture gives us information about dynamics in the ray approximation, we desire other ways to connect this more concretely with the wave dynamics. One such method is known as a Husimi distribution. The Husimi distribution is a quasi-probability distribution first utilized in analyzing properties of the density matrix in quantum mechanics [12]. In that context it is used in quantum optics and quantum tomography to project a quantum mechanical Hilbert space onto phase space in a positive definite form. It also is useful in the context of microcavity optics because the Helmholtz equation has a formal mathematical

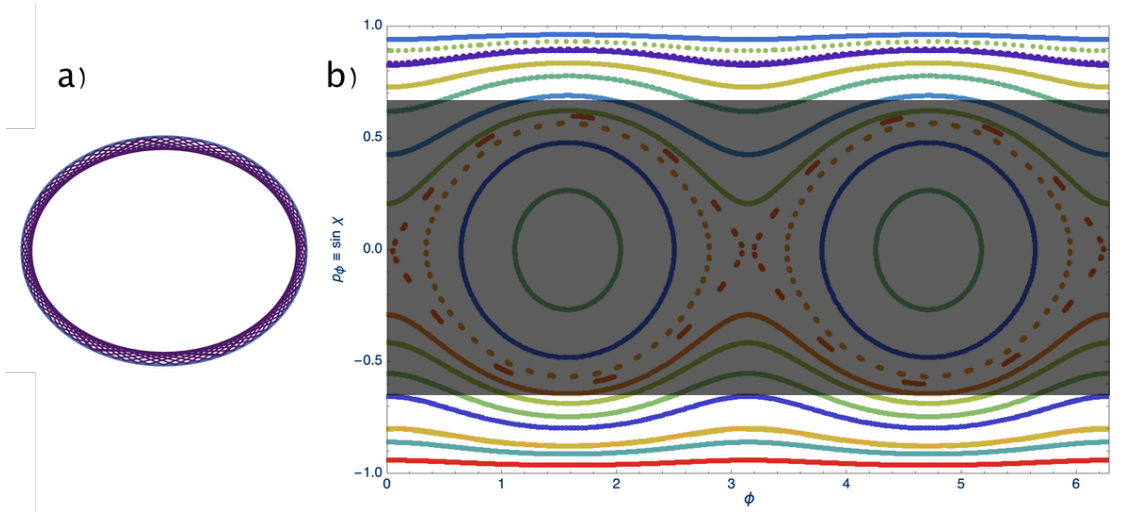


FIGURE 2.6. (a) Elliptical cavity and typical WGM like trajectory. (b) SOS showing invariant curves of the ellipse. The shaded region shows the region that does not satisfy  $\sin \chi > 1/n$ ,  $n = 1.5$ . This region does not support long lived resonances, only invariant curves that are entirely outside this region will support high-Q modes.

analog with the Schrödinger equation [13]. In this setting, the Husimi distribution acts as a projection of the normal derivative of the resonant wave function at the boundary of a cavity onto a coherent state (Gaussian mode) in the phase space described by the Poincaré section. In the context of this work and the numerical computations, we use the form of the Husimi distribution described by B. Dietz, et al. in [14, 15],

$$H_n(p, q) = \frac{1}{2\pi k_n} \frac{1}{\int_0^L dq' \left| \langle \hat{n}(q'), \vec{\nabla} \Psi_n(q') \rangle \right|^2} \left| \int_0^L dq' \langle \hat{n}(q'), \vec{\nabla} \Psi_n(q') \rangle C_{(p,q)}^\rho(q'; k_n) \right|^2$$

where

$$C_{(p,q)}^\rho(q'; k_n) = \left( \frac{k_n}{\pi \rho^2} \right)^{1/4} \sum_{m=-\infty}^{\infty} \exp(ipk_n(q' - q + mL) - \frac{k_n}{2\rho^2}(q' - q + mL)^2).$$

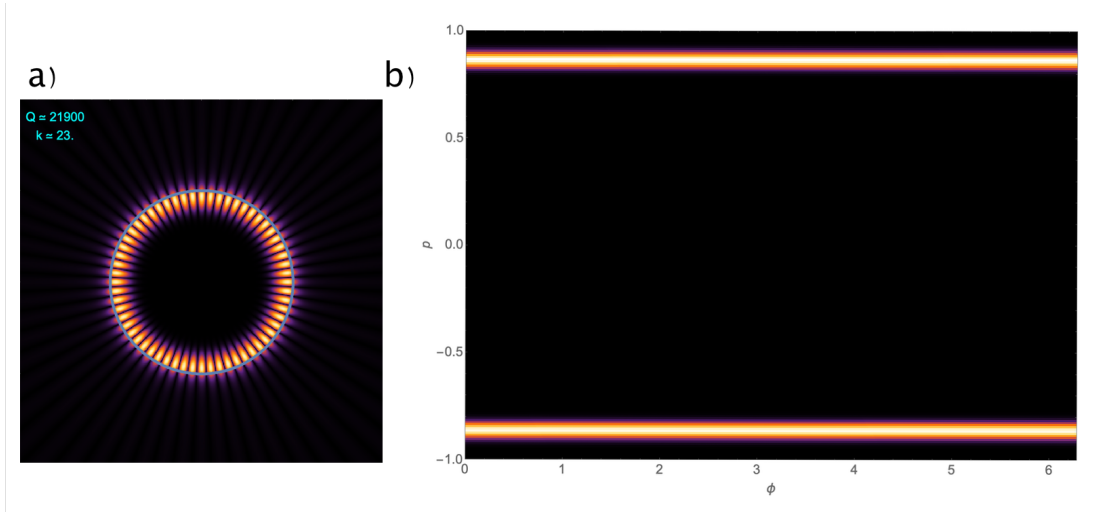


FIGURE 2.7. (a) Numerically computed resonance for the circular cavity with  $k \simeq 23$ ,  $n = 1.5$ . (b) Husimi distribution for this resonance, note that there is energy in both the positive and negative halves of the SOS, which correspond to the degenerate modes with  $m = \pm 30$ .

The function  $C_{(p,q)}^\rho$  represents the coherent state that the distribution projects onto, where  $\rho$  is the resolution of the Husimi distribution. There is a tradeoff with the resolution defined by  $\rho$  because as a wave equation there is an uncertainty limit in phase space between position along the boundary and the angular momentum analogous to the Heisenberg uncertainty principle from quantum mechanics. This is a simple consequence of the Fourier uncertainty between conjugate variables in phase space.

Figure 2.7 shows an example of a Husimi distribution for the circular cavity. The resonance and corresponding field on the boundary was calculated numerically (using the package described in Chapter 3). As described in section (2.3), the resonance field pattern shows both the  $\pm m$  contributions and this is reflected in the Husimi distribution which shows a signal in both the positive and negative halves of the SOS. The resolution in this example was chosen arbitrarily to highlight the location of the resonance in the angular momentum dimension, this choice can

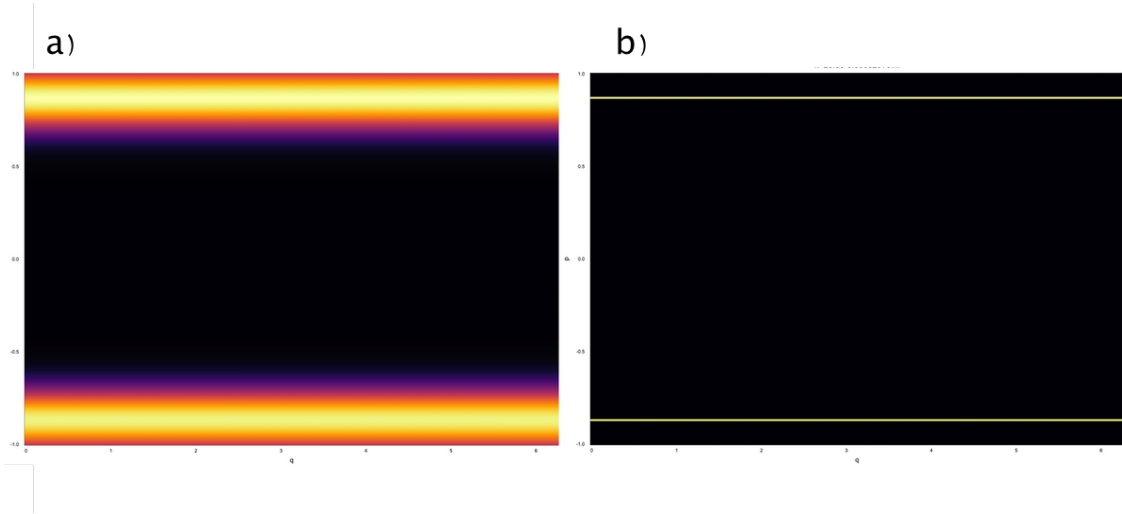


FIGURE 2.8. Husimi distributions for the resonance in Fig. 2.7. (a)  $\rho = 1$  (b)  $\rho = 50$

be made differently which would result in more (or less) certainty in the angular momentum at the expense (or benefit) of certainty in position space. In this case since the projection over the position is evenly and continuously distributed, the impact of this choice is not visible. However in cases where the angular momentum is not a constant function of position, some tradeoff must be made in order to balance the information gained in each dimension. Figure 2.8 shows the difference in angular momentum resolution for two choices of  $\rho$ .

This tradeoff is more visible in the context of the elliptical billiard. Since angular momentum is not preserved, it is not possible to choose an arbitrarily fine resolution for it and still get accurate position information. In Figure 2.9, a WGM type mode is shown along with three Husimi distributions of varying  $\rho$ . The choice of  $\rho = 5$  in Fig. 2.9.b shows an appropriate balance of position and angular momentum resolution, and the invariant curve associated with the resonance is clear. In Fig. 2.9.c, the areas of greatest leakage where the curvature is greatest can be seen, but the angular momentum is smeared. In Fig. 2.9.d, the angular



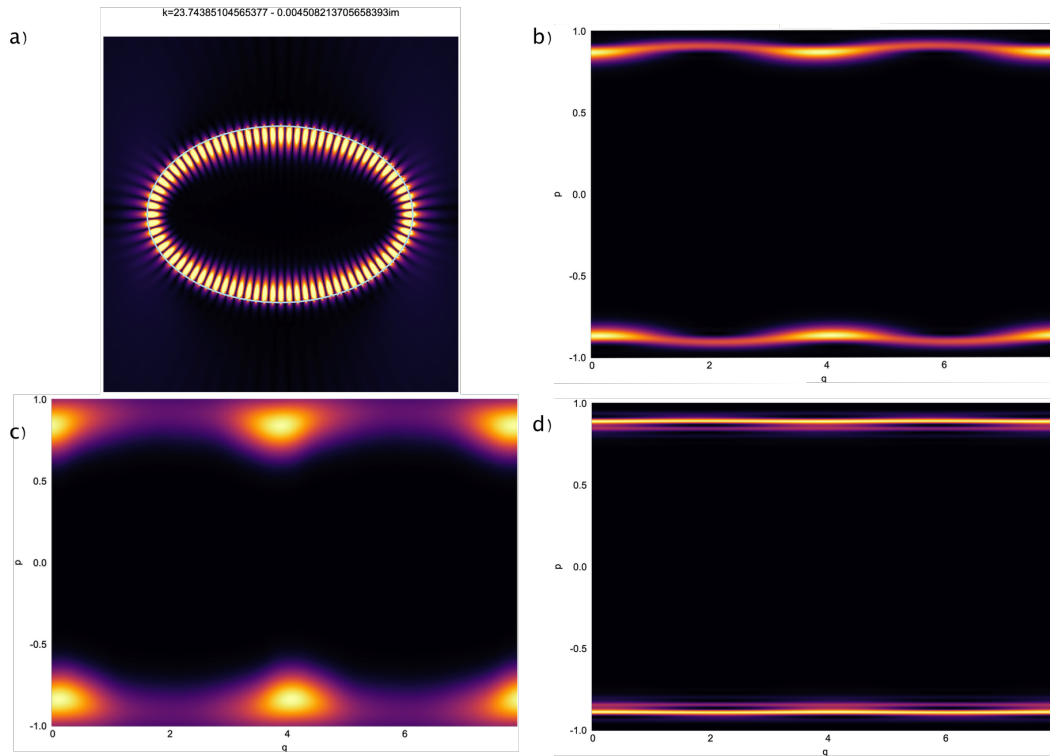


FIGURE 2.9. Husimi distributions for the elliptical cavity. (a) WGM resonance spatial intensity (b)  $\rho = 5$  (c)  $\rho = 1$  (d)  $\rho = 10$

momentum components that most strongly contribute to the resonance are visible, but the position information has been lost.

## CHAPTER III

### BOUNDARY INTEGRAL METHOD IMPLEMENTATION

Having seen in Chapter 2 that analytic solutions for resonances in optical microcavities are only present for a small number of geometries which have special symmetries and are “integrable”, we now shift attention to methods for analyzing general two-dimensional cavities. For small deformations from the circle, perturbation theory may be used. However many geometries lie far outside the regime where perturbation theory is predictive. We would like to have robust methods for finding the resonance wavenumbers and quality factors accurately and quickly. Often, individual resonances do not reveal the behavior of the system and information on the overall spectral response of the system over a wide range of frequencies is more helpful. This requires discovering and computing many resonances.

#### **3.1. Time Domain Methods**

The methods for computing resonances rely on numeric approximations for solving Maxwell’s equations and can broadly be split into two categories: time domain methods and frequency domain methods. Time domain methods have been in use for a long time, utilizing Yee’s algorithm which was published in 1966 [16]. This algorithm discretizes time and space in a way that turns Maxwell’s equations into a set of finite difference equations. By choosing an appropriately fine grid spacing and time step, it can be shown that evolving the electric and magnetic fields in time in a “leapfrog” manner can result in a stable and accurate solution. Since that time, many improvements and innovations have been found and mature

implementations of FDTD software packages are available both commercially and as open source. One popular open source framework from MIT is MEEP [17].

This method is quite useful and general purpose, but there are some drawbacks. The entire spatial domain of the simulation must be discretized in a grid, so empty or homogenous regions of space end up being just as expensive computationally as those with interfaces or boundaries. Often, the relevant behavior occurs at these boundaries so computation in other regions is in some sense wasteful. Since the domain of the simulation must itself be bounded, EM fields that travel to the edges experience a sharp impedance mismatch and in naive implementations this causes reflections which will back-propagate into the system in an artificial way causing inaccurate results. Methods have been devised to reduce these reflections, one such method is the so called “perfectly matched layer” (PML) which acts as a region of finite thickness placed near the edges which absorb the outgoing radiation in an impedance matched way, thus effectively absorbing and therefore drastically reducing (but not entirely eliminating) reflections. However the PML itself must take up some simulation space to be effective and therefore it increases the computational cost. The structure of interest must be surrounded with some empty space and then additional space for the PML to ensure that reflections do not couple back into the structure. Methods for adaptive grid spacing are available in some commercial packages, which can offset some of these issues, but one must be careful to avoid artifacts caused by numerical dispersion from too coarse a grid.

When studying microcavities, the main results one hopes to find are the resonant frequencies, cavity lifetimes and field patterns for those specific frequencies. FDTD provides a proxy to those results but as a time based method

does not directly provide them. When studying scattering or resonances, a time dependent EM field must be created somewhere inside the simulation domain. Since the field is not present at the start of the simulation, it must be turned on and then evolved in time. If one desires to simulate the system at a defined frequency, the field cannot be turned on abruptly, since the sharp change in the time domain would imply a very broad excitation in the frequency domain. Instead the field must be slowly ramped up, the rate of which depends on how narrow a frequency range is desired. In the limit of a monochromatic field, the field would take an infinite time to ramp up so there is always a tradeoff between pulse width and simulation time. In some cases, it is easier to choose a relatively broad and short pulse, which can potentially excite many resonances simultaneously. Although this complicates the response if one is simply examining the field patterns manually, the field may be measured somewhere in the cavity and the frequencies extracted via Fourier transform or other similar technique. In MEEP, an auxiliary package is included that utilizes a harmonic inversion based on the filter diagonalization method. While a Fourier transform would require a sampling rate sufficient to satisfy the Nyquist condition, this sparse sampling approach allows accurate estimation of periodic components when only a few strong frequency signals are expected [18]. Even with this approach, spurious frequencies can be found so if a broad pulse is used to find initial candidates, it is often necessary to run the simulation again with a narrow pulse to confirm the initial findings and to visualize the field patterns isolated from other resonances. These consequences of the indirect nature of finding resonances using FDTD suggest that working in the frequency domain may be a better fit for the understanding the physics of microcavities.

### 3.2. Boundary Integral Method

Frequency domain methods are also varied and include finite element modeling (FEM) and finite difference frequency domain (FDTD) algorithms. FEM methods can be quite effective especially in cases where the boundary conditions are of Dirichlet form. These are closed systems where the wavefunction vanishes at the boundary and can describe the resonant vibrational modes of two-dimensional membranes. As an aside, the question of how the geometry of such membranes affects their spectrum has been the subject of inquiry for some time [19]. However for open systems like optical cavities there exists another method that can be used to find resonances based on solving the wave equation on the boundary of interfaces between regions of homogenous material properties. This approach is called the boundary integral method (BIM).

The boundary conditions for dielectric cavities is neither Dirichlet or Neumann; instead, as described in Chapter 2, for a TE polarization, the wavefunction and its normal derivative are continuous across the interface between regions of homogenous dielectric constant. As such, the modes are not bounded but instead are the quasi-bounded modes with complex wavenumber  $k = k_r - \kappa i$ . In ref. [20], a general derivation of the boundary integral equations is given for the case of two-dimensional dielectric resonators. The method transforms the two-dimensional Helmholtz equation into one-dimensional integral equations, using a Green's function approach.

### 3.2.1. Green's Functions and Boundary Integral Equations

The Green's function for a differential equation encodes the impulse response of the system. Given a differential operator  $\mathcal{L}$  for a linear differential equation,

$$\mathcal{L}G(x, y) = \delta(x - y)$$

In the present case, our differential operator is that of the Helmholtz equation, so here

$$[\nabla^2 + n_j^2 k^2]G(\mathbf{r}, \mathbf{r}'; k) = \delta(\mathbf{r} - \mathbf{r}'). \quad (3.1)$$

Given the condition on outgoing radiation only for resonant solutions, the two-dimensional Green's function is

$$G(\mathbf{r}, \mathbf{r}'; k) = -\frac{i}{4}H_0^{(1)}(n_j k |\mathbf{r} - \mathbf{r}'|) \quad (3.2)$$

where  $H_0^{(1)}$  is the zeroth-order Hankel function of the first kind, and  $n_j$  is the index of refraction in a homogenous region  $j$ . Given a wavefunction  $\psi$  that solves the Helmholtz equation,

$$\nabla^2 \psi + n^2 k^2 \psi = 0 \quad (3.3)$$

we can apply the impulse response of the Green's function to turn the differential equation for the unknown solution into an integral equation.

In two dimensions Stokes' theorem can be used to produce Green's first identity,

$$\oint (\psi \nabla \phi - \phi \nabla \psi) \cdot \hat{\mathbf{n}} ds = \iint (\psi \nabla^2 \phi - \phi \nabla^2 \psi) dA$$

Choosing  $\phi = G$ ,

$$\oint(\psi\nabla G - G\nabla\psi) \cdot \hat{\mathbf{n}}ds = \iint(\psi\nabla^2 G - G\nabla^2\psi)dA \quad (3.4)$$

Then using Eq. (3.1),

$$\nabla^2 G = \delta(\mathbf{r} - \mathbf{r}') - (nk)^2 G$$

which we can insert into Eq. (3.4),

$$\oint(\psi\nabla G - G\nabla\psi) \cdot \hat{\mathbf{n}}ds = \iint(\delta(\mathbf{r} - \mathbf{r}')\psi - (nk)^2 G\psi - G\nabla^2\psi)dA$$

Using the delta function,

$$\oint(\psi\nabla G - G\nabla\psi) \cdot \hat{\mathbf{n}}ds = \psi(\mathbf{r}') - (\iint G(nk)^2\psi + G\nabla^2\psi)dA$$

And since we assume  $\psi$  is a solution to the Helmholtz equation, we find that

$$\psi(\mathbf{r}') = \oint(\psi\nabla G - G\nabla\psi) \cdot \hat{\mathbf{n}}ds$$

Therefore, by calculating the line integral of the wavefunction on the boundary times the normal derivative of the Green's function minus the Green's function on the boundary minus the normal derivative of the wavefunction, we can calculate the wavefunction at another point away from the boundary. One complication is that in doing the contour integral it is necessary to evaluate the Green's function and its normal derivative at identical points on the boundary where  $\mathbf{r} - \mathbf{r}' = 0$ , and there the Green's function has a singularity, see Fig. 3.1.

However, these singularities can be handled by using the Cauchy principal value for the improper integral. An excellent description of the mathematical details for this is given in [21]. In calculating the principal value of this integral on the boundary, the result is the average of the boundary field value on either side of the interface,

$$\frac{1}{2}\psi(\mathbf{r}') = \mathcal{P} \oint (\psi(s)\partial_\nu G(s, \mathbf{r}'; k) - G(s, \mathbf{r}'; k)\partial_\nu \psi) ds$$

When considering a circle far away from the cavity  $\Gamma_\infty$ , it is possible to show that the wavefunction vanishes on this boundary, and thus it is possible to cast the BIEs in each region as a matrix equation of integral operators on each boundary. The integral operators

$$\begin{aligned} B(s, s') &= -2G(s, s'; k) \\ C(s, s') &= -2\partial_\nu G(s, s'; k) - \delta(s - s') \end{aligned}$$

can be used along with the the normal derivative of the wavefunction  $\psi$  defined as  $\phi = \partial_\nu \psi$  to arrive at the matrix equation

$$\begin{pmatrix} B_1 & C_1 \\ B_2 & C_2 \\ \vdots & \vdots \\ B_j & C_j \end{pmatrix} \begin{pmatrix} \phi \\ \psi \end{pmatrix} = 0$$

A search for the resonant values that satisfy this equation is then a nonlinear eigenvalue problem to find the non-trivial solutions as a parameter of the complex valued  $k$ .



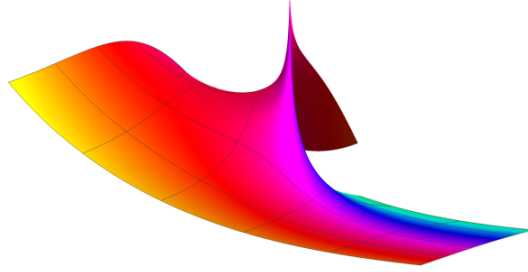


FIGURE 3.1. Green's function Eq. (3.2) plotted in complex plane. Note singularity at origin.

### 3.2.2. Issues With This Approach

We experienced some problems when using this direct and somewhat simple method to find resonances as described in [20]. The author mentions the existence of spurious solutions because these equations also simultaneously solve an interior Dirichlet problem, where the boundary is closed and the wavefunction vanishes there. Although the author mentions this issue and dismisses it as generally not a problem, when implementing this approach and testing with a circular cavity, we experienced problems with these spurious solutions being present around other valid resonances, and the modified Newton's method used to converge on a resonance would be compromised by their presence. If valid and spurious solutions existed closely in the complex plane, the extremely deep minimum of the spurious solution would tend to pull the solver away from the real solution which often had a less steep gradient. The convergence properties and required discretization were also not as good as those in the methods to be introduced below.

### 3.2.3. BIEs Based On Potential Theoretic Operators

Applied mathematicians have spent a great deal of time studying the properties of linear differential equations like the Helmholtz equation, including methods that guarantee uniqueness of solutions, optimize the convergence properties and properly handle formally infinite values that come about in the BIEs [22]. In reference [2], Heider describes an approach based on potential theory utilizing the concepts of single layer and double layer potentials and the jump conditions that occur from the inside of a boundary to the other side.

The complexity of this approach is surely greater than the simpler derivation directly using the Green's function BIEs above, as the operators need a more careful treatment to avoid singularities that occur in the Green's functions and their derivatives when  $\mathbf{r} = \mathbf{r}'$ . In particular, this method utilizes a set of integral operators,

$$\begin{aligned}
 (K_{i/e}\psi)(x) &= 2 \int_{\Gamma} \frac{\partial G_{i/e}(x, y; k)}{\partial \nu_y} \psi(y) ds_y \\
 (K_{i/e}^*\phi)(x) &= 2 \int_{\Gamma} \frac{\partial G_{i/e}(x, y; k)}{\partial \nu_x} \phi(y) ds_y \\
 (S_{i/e}\phi)(x) &= 2 \int_{\Gamma} G_{i/e}(x, y; k) \phi(y) ds_y \\
 (T_{i/e}\psi)(x) &= 2 \frac{\partial}{\partial \nu_x} \int_{\Gamma} \frac{\partial G_{i/e}(x, y; k)}{\partial \nu_y} \psi(y) ds_y
 \end{aligned} \tag{3.5}$$

where the subscripts  $i/e$  refer to the internal and external domains, i.e. inside and outside the cavity,  $\psi$  is the wavefunction solution, and  $\phi$  is the normal derivative of  $\psi$ . While the Green's function itself and its first derivative have weak and Cauchy singularities, respectively, the  $T$  operator is known as a hyper-singular integral operator as it includes the second normal derivative of the Green's function.

Due to the singularities present in these BIEs, Heider’s approach uses a singularity subtraction method combined with quadratures to tame the singularities in a Nyström discretization. These methods are shown to produce exponential convergence properties as a function of discretized points along the boundary. Then an application of Green’s theorem in terms of the integral operators in Eq. (3.5) shows that

$$u_{i/e}(x; k) = \frac{1}{2}(K_{i/e}\psi + S_{i/e}\phi)$$

Given the continuity conditions for the field and normal derivative at the boundary, the system of equations for the unknowns  $\psi, \phi$  are

$$\left( 2 \cdot \begin{pmatrix} I & 0 \\ 0 & I \end{pmatrix} - \begin{pmatrix} -(K_e - K_i) & -(S_e - S_i) \\ T_e - T_i & K_e^* - K_i^* \end{pmatrix} \right) \begin{pmatrix} \psi \\ \phi \end{pmatrix} = A(k) \begin{pmatrix} \psi \\ \phi \end{pmatrix} = 0$$

This is a non-linear eigenvalue problem for the matrix  $A$  as a function of  $k$ . This is also described in the literature as a Calderón projector.

### 3.3. Implementation of BIEs in Julia

Starting from the algorithm described in [2], our goal was to implement a reusable open source software package that would allow us to explore new geometries, especially those inaccessible through other methods such as concave geometries. The result of this work is available at <https://github.com/kahliburke/BoundaryIntegralMethod.jl>. The use of this package is based on the algorithm described by Heider. Given a candidate complex wavenumber  $k$ , the Direct Sweep Algorithm is used to find approximate resonance wavenumbers and boundary field values near to the starting point. Once a set of approximate

wavenumbers have been calculated, the wavenumbers and boundary field values are used as input to the Residual Inverse Iteration algorithm. This algorithm uses a Newton step method to refine the input data until the desired convergence is found, or the procedure fails to converge. Once a resonance is found, the surrounding field intensity can be calculated from the boundary value using the Green's function to propagate the field from the boundary to the desired point. We also implemented a procedure to create Husimi projections from the resulting boundary field values.

### **3.3.1. Julia Language**

The Julia language [23] is a relative newcomer in the area of scientific computing. First revealed in 2012, it has gained significant traction since that time and at the time of writing has been downloaded millions of times, and is in use at thousands of universities worldwide. Julia was envisioned as a project to create a language informed by modern compiler techniques and language features, while retaining the performance of low-level programming languages traditionally used for scientific and other performance conscious applications such as C, and Fortran. At the time that we began on an implementation of a package to investigate new microcavity geometries, initial prototyping in Mathematica encouraged us to look at more performant languages. At this time Julia was becoming mature enough to consider and was ultimately chosen.

Julia provided access to the required special functions, Bessel and Hankel functions for complex arguments as well as integration with longstanding standard packages for linear algebra like BLAS and LINPACK. Julia provides convenient and performant access to libraries written in C and Fortran, and even Python, so it is possible to leverage existing scientific code. Although it is a compiled language, it

has excellent dynamic language features such as a REPL and the ability to program interactively using the Jupyter environment. This provision also makes it easy to use on a remote system because the Jupyter environment may be run on the remote system and connected to via a browser.

### 3.3.2. Example of Usage

A boundary is defined by extending the SimpleBoundary type and defining a couple of functions for the points on the boundary given the parameter  $t$  which contains points in the range  $[0, 2\pi)$ . Given a discretization  $N$ , there are  $2N$  points chosen in this range. In the case of the circle, these points can just refer to the polar angle  $\phi$  and are evenly spaced, but for other geometries they can represent any choice of discretization along the boundary. This can be useful to place more points in areas of higher curvature where the field could be expected to change rapidly. Listing 1 shows an example of defining a circular boundary (this is already available in the package so defining it again is not necessary). The boundary is expected to have two properties “ni” and “ne” which determine the index of refraction inside and outside the boundary.

Once the boundary geometry has been defined, the Direct Sweep and RII procedures may be used. This is outlined below in the included *Jupyter* kernel session, which also serves to demonstrate the key features of the API exposed by the Julia package.

```
using Logging
logger = ConsoleLogger(stdout, Logging.Warn)
global_logger(logger)
using ProgressMeter
ProgressMeter.ijulia_behavior(:clear)
using Revise
using Printf
```

Here we import the packages we'll use in the example

```
using BoundaryIntegralMethod
using BoundaryIntegralMethod.DirectSweep
using BoundaryIntegralMethod.Husimi
using BoundaryIntegralMethod.Utilities
```

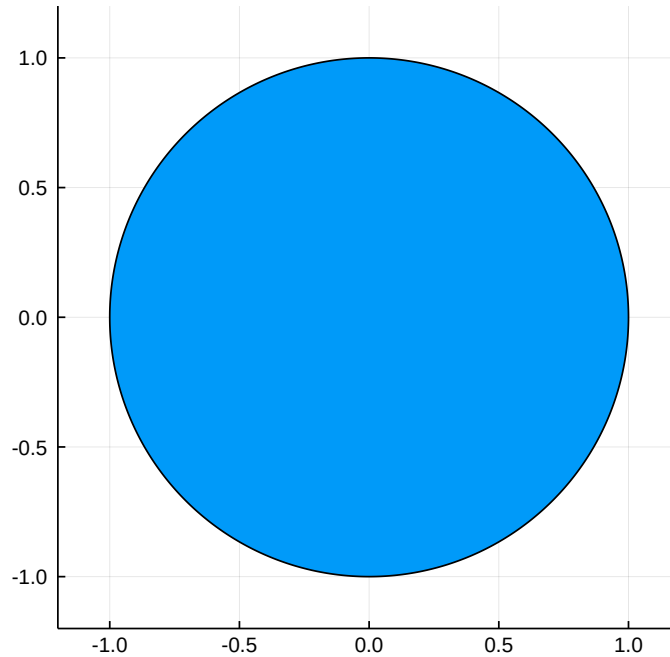
Create a circular cavity of radius 1 with inside index of refraction  $n=1.5$

```
# Create a circular boundary
# Internal n
ni=1.5
# External n
ne=1.0
# Radius
r = 1.0
b = BoundaryIntegralMethod.Circle(r, ni, ne)
```

```
Circle(Point2D(0.0, 0.0), 1.0, 1.5 + 0.0im, 1.0 + 0.0im)
```

We can use the `plotBoundary` function to see the boundary geometry

```
using Plots
plotBoundary(b; lims=(-1.2,1.2))
```



Starting from an initial guess of resonance position, calculate the approximate nearby resonances

```
k0= 23.04 - 0.0001im
n=100
(ks, xs) = directSweep(b, n, k0)
ks[1:6]
```

```
6-element Array{Complex{Float64},1}:
 23.048608753331553 - 0.0004904433281194082im
 23.048608753331575 - 0.0004904433281181643im
 23.271785585683357 - 0.021256297006020997im
 23.27178558568336 - 0.021256297006018474im
 22.83354194488385 - 0.3293855164414596im
 22.83354194488385 - 0.3293855164414624im
```

The results are sorted with the narrowest candidates first. Note that the candidates appear to come in pairs, this is due to the degeneracy of clockwise and anti-clockwise traveling waves. We see here 3 resonances in the vicinity where there is a very narrow one at the top and broader resonances at the bottom.

Choosing the first candidate in the list, now use the RII algorithm to refine the estimated  $k$  and field values and get a more exact answer. This is always necessary because some of the candidates found by direct sweep algorithm may not converge. This is more common the further away from the initial guess we get.

```

i = 1
convergence = 1e-8
maxIters = 10
(kf, xf) = residualInverseIteration(maxIters, convergence, b, n, ks[i],
→xs[i,:]);

```

Finding resonance: Time: 0:00:09 (3 iterations)

```

iter:          3
dk:           5.448280157862642e-10 +
3.8805671283451203e-10im
kl:           23.04860545975862 -
0.0005266205152489876im
|A(kl+1).x_1|/|x_1|: 4.3199947119530777e-11
|A(kl+1).x_1+1|/|x_1+1|: 2.9324941822471615e-15

```

```

kf

```

```

23.048605459758623 - 0.0005266205152496217im

```

```

qFactor(kf)

```

```

21883.5050974357

```

We have found a resonance with  $Q \approx 22000$

Now let's visualize the field, calculating it from the final boundary field value

```

field = exportTotalField(b, xf, kf, outFile="output/circle-$kf.h5";
→xRange=(-2.0,2.0), yRange=(-2.0,2.0), dx=.01, dy=.01);

```

```

Progress: 49%|-----| | ETA:

```

```

0:00:35

```

```

Error: SpecialFunctions.AmosException(1)
@ BoundaryIntegralMethod

```

```

~/julia/dev/BoundaryIntegralMethod/src/totalField.jl:55

```

```

Progress: 100%|-----| Time:

```

```

0:01:07

```

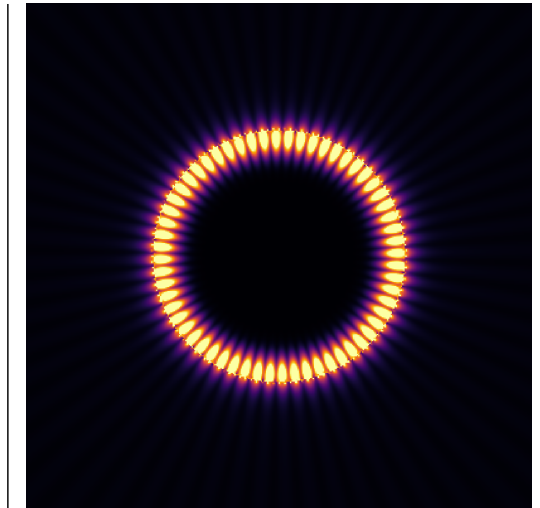
```

kfStr = @sprintf("%0.2f%0.8fim", real(kf), imag(kf))
Plots.heatmap(clamp.(abs.(field), 0, .5), cbar=false, aspect_ratio=1,
→size=(400,400), ticks=nothing, title=kfStr)

```



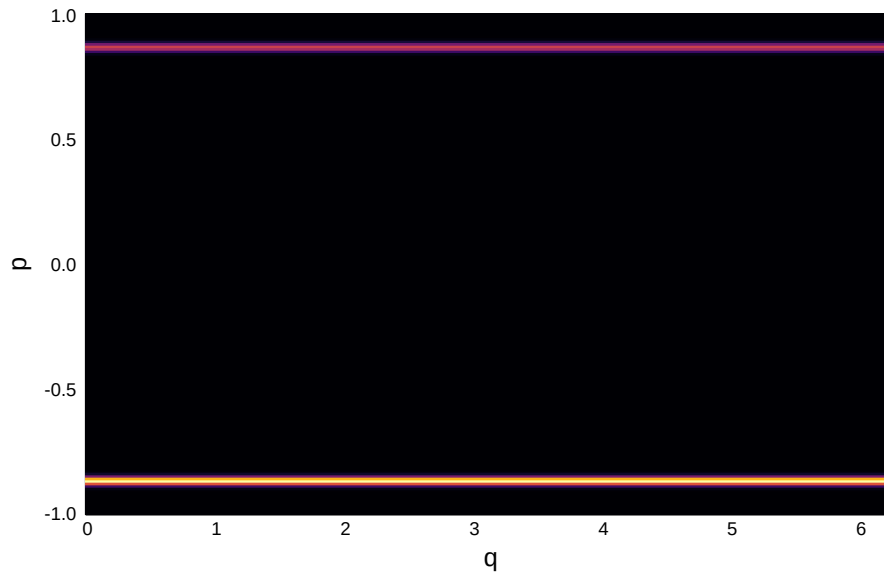
23.05-0.00052646im



We can also compute the Husimi distribution from the field values

```
(qs, ps, hVals) = husimiDistribution(kf, xf, b; I=10, pStep=.01, mTerms=5);  
heatmap(qs, ps, (hVals.^1), size=(600,400), title="k=$kfStr", cbar=false)  
xaxis!("q")  
yaxis!("p")
```

k=23.05-0.00052646im



---

```

1 struct Circle <: SimpleBoundary
2   # Center of circle
3   center::Point2D
4   # Radius
5   r::Float64
6   # Internal index of refraction
7   ni::Complex{Float64}
8   # External index of refraction
9   ne::Complex{Float64}
10 end
11
12 function boundaryPoint(c::Circle, t::Float64)
13   Point2D(c.center.x+cos(t)*c.r, c.center.y+sin(t)*c.r)
14 end
15
16 function boundaryPointDeriv(c::Circle, t::Float64)
17   c.r*[-sin(t), cos(t)]
18 end

```

---

Listing 1 Defining Boundary Geometry

### 3.3.3. Validation

In order to validate the accuracy of the code, we compared results for resonances known for the circular dielectric cavity with our numerical results. Fig. 3.2 shows the absolute error  $|k - k^*|$  where  $k^*$  is the true resonance value as calculated using the methods described in Chapter 2. This error is calculated for a narrow resonance ( $Q \simeq 22000$ ) as a function of the discretization value  $N$ . This shows both that the implementation is capable of finding narrow resonances with the correct wavenumber. A comparison of the calculated field to the exact solution was also made, ensuring that the spatial pattern matched and the number of azimuthal nodes was correct for the chosen value of  $m = 30$ . The error drops off very rapidly for this case and by the time  $N = 70$  we can already calculate the sensitive imaginary part of  $k$  to six decimal places. The time required to

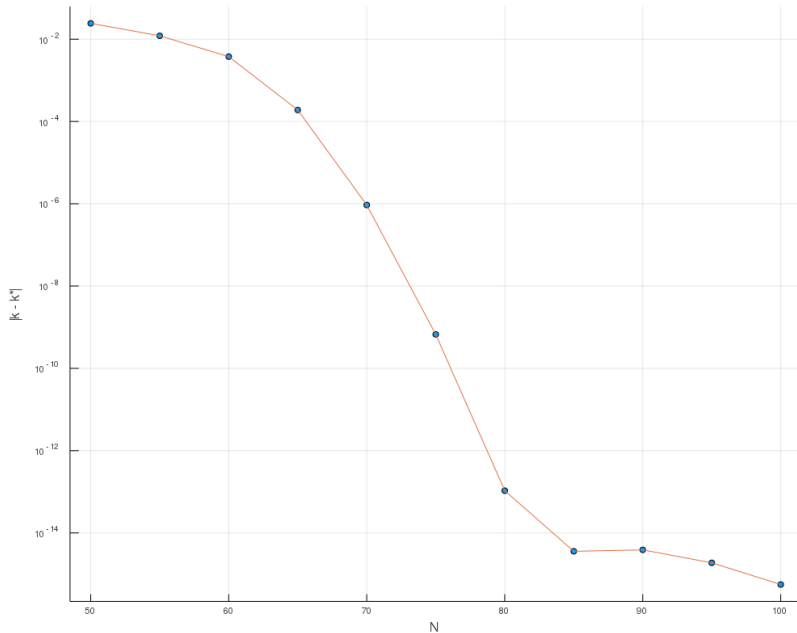


FIGURE 3.2. Error vs. discretization for circular cavity resonance  $m = 30, \nu = 0, k \simeq 23$ , showing exponential convergence.

converge to this solution including the Direct Sweep and RII algorithms is only a few seconds.

We also validated the code against other geometries such as the quadrupole billiard for which solutions for bow-tie resonances are available and found similar agreement.

### 3.3.4. Algorithm for Scanning Spectral Response

To characterize the spectral patterns for cavities it is often necessary to scan a wide range of  $k$ -space. Although the direct sweep method has the ability to find multiple resonances near an initial starting guess  $k_0$ , we observed that the ability to discern and identify relevant starting  $k$  values for the secondary RII step decreases rapidly as  $\|k_0 - k\|$  increases. This is especially true for high-Q modes, as the resonance width for these modes are very narrow and we empirically observed

that the direct sweep method discovers wider resonances in the vicinity of narrow resonances more easily which may mask the presence of the narrow resonances. Therefore, in order to reliably find the high-Q modes it is necessary to adopt a scanning procedure in which small regions of  $k$ -space are examined piecewise and candidate high-Q modes are identified within those small regions. The procedure we use is described in Algorithm 1.

Because candidate  $k$  values are retained both above and below the center point  $k_0$ , there is overlap between adjacent center points and most of the resonances which will eventually be discovered by the RII procedure will appear twice in the list of candidates. However, since different starting  $k_0$  values are used in the direct sweep procedure, the exact values of these “duplicate”  $k_{\text{cand}}$  are numerically slightly different as the candidates are discovered by a linear approximation to the eigenvalue problem around the vicinity of the initial guess  $k_0$ . In practice, when resolving the more accurate  $k_f$  and the boundary field  $x_f$  using the RII procedure, these slightly different starting points will converge to the same resonance within the numerical tolerances specified for the RII algorithm as well as display an identical spatial field pattern so we conclude that they are in fact the same mode. Therefore in many cases it is possible to be more computationally efficient by combining or averaging very close candidate  $k$  values found in adjacent regions of  $k$ -space spanned by Algorithm 1, or in eliminating the overlap and keeping candidates at each step in the range  $k_0 - k_{\text{step}}/2 \leq k_{\text{cand}} \leq k_0 + k_{\text{step}}/2$  or  $k_0 \leq k_{\text{cand}} \leq k_0 + k_{\text{step}}$ . We generally choose to err on the side of the extra computation in the interest of not missing any important resonances in the scan. It should be noted that some boundary geometries (such as the Reuleaux billiard[14]) exhibit very closely spaced doublets, and a careful approach may be necessary to avoid missing resonances.

1. Given a large  $k$  range of interest from  $k_{\min}$  to  $k_{\max}$ , choose a small step size ( $k_{\text{step}} = .02$ ) as a discretization.
2. Choose a target  $\kappa$  for the imaginary part of  $k$ . We choose a small value ( $\kappa = .0001$ ) to target high-Q modes.
3. Starting at  $k_0 = k_{\min} - i \kappa$ , execute the direct sweep procedure to generate candidate resonances.
4. Filter the candidate resonances to keep only those where  $k_0 - k_{\text{step}} \leq k_{\text{cand}} \leq k_0 + k_{\text{step}}$ , as they will be found again by a closer  $k_0$  if outside that range and are less likely to converge to a valid resonance further away from  $k_0$ .
5. Increment  $k_0$  by  $k_{\text{step}}$  and repeat this procedure until the desired range has been covered.

#### Algorithm 1 $k$ -space scan for high-Q modes

Once the list of candidate  $k_0$  values have been generated, the final  $k_f$  and  $x_f$  values are determined by first filtering the candidates to exclude very low-Q modes with  $\kappa > 1.0$  and then running the direct sweep procedure with starting guess  $k_0 = k_{\text{cand}}$  for each remaining candidate. The reason for the repeated direct sweep procedure is that since a large number of candidates are initially generated, we do not store the boundary fields  $x$  associated with them. Since the input to the RII algorithm requires both the starting  $k_0$  and the boundary field  $x_0$ , we need to regenerate the boundary field. Since the initial candidates  $k_0$  were already close to their final  $k$ , the subsequent direct sweep will in general produce inputs to the RII procedure that are even closer to the final convergent values and thus few iterations of the RII loop are required.

### 3.3.5. Corrections to Boundary Integral Equations

In the process of implementing our package, we discovered some errors in reference [2]. These initially caused us some delays as we attempted to debug the software. In order to prevent such frustration to future research, here are the corrections to Heider's publication.

We discovered two errors in the equations listed in the Appendix of [2]. The first appears in the description of  $\tilde{N}$  below equation (A.6). There is a sign error in the last term. The corrected equation is:

$$\begin{aligned} \tilde{N}(t, \tau) = & \frac{i}{2} \bar{N}(t, \tau) \left\{ (k n_e)^2 H_0^{(1)}(k n_e |x(t) - x(\tau)|) \right. \\ & \left. - \frac{2k n_e H_1^{(1)}(k n_e |x(t) - x(\tau)|)}{|x(t) - x(\tau)|} \right\} \\ & + \frac{i k n_e x'(t) x'(\tau)}{2 |x(t) - x(\tau)|} H_1^{(1)}(k n_e |x(t) - x(\tau)|) \\ & - \frac{i}{2} \bar{N}(t, \tau) \left\{ (k n_i)^2 H_0^{(1)}(k n_i |x(t) - x(\tau)|) \right. \\ & \left. - \frac{2k n_i H_1^{(1)}(k n_i |x(t) - x(\tau)|)}{|x(t) - x(\tau)|} \right\} \\ & - \frac{i k n_i x'(t) x'(\tau)}{2 |x(t) - x(\tau)|} H_1^{(1)}(k n_i |x(t) - x(\tau)|) \end{aligned}$$

The other error is in the equation for the diagonal terms  $\tilde{N}_2(t, t)$ , where the log terms should not use the norm of  $x'(t)$  squared, but simply the norm. The

corrected equation is:

$$\begin{aligned} \tilde{N}_2(t, t) = & \frac{|x'(t)|^2}{4\pi} [(kn_e)^2 - (kn_i)^2](\pi i - 1 - 2C) \\ & + \frac{|x'(t)|^2}{4\pi} \left[ -2(kn_e)^2 \ln \left( \frac{kn_e |x'(t)|}{2} \right) + 2(kn_i)^2 \ln \left( \frac{kn_i |x'(t)|}{2} \right) \right] \end{aligned}$$

### 3.3.6. Derivatives

Heider's boundary integral approach describes the  $A$  matrix and its use in iteratively finding a resonant solution to the boundary integral equations. This iterative procedure requires the use of  $A'(k)$ , both in the direct sweep procedure (Algorithm 3) and the Newton's iteration step in the RII procedure (Algorithm 1). The derivation of the derivative matrix is straightforward and the results are outlined below, in terms of the constituent equations provided in the paper's appendix.

The  $A'(k)$  matrix is defined as

$$A'(k) = \begin{bmatrix} -(K'_e(k) - K'_i(k)) & -(S'_e(k) - S'_i(k)) \\ T'_e(k) - T'_i(k) & K_e^{*'}(k) - K_i^{*'}(k) \end{bmatrix}$$

with the  $K, S, T$ , and  $K^*$  integral operators being expressed after singularity subtraction in terms of equations

$$\tilde{H}_1(k), \tilde{H}_2(k), \tilde{H}(k), \tilde{M}_1(k), \tilde{M}_2(k), \tilde{M}(k), \tilde{N}_1(k), \tilde{N}_2(k), \tilde{N}(k), \tilde{L}_1(k), \tilde{L}_2(k), \tilde{L}(k).$$

All other equations given in the appendix are independent of the wavenumber  $k$ .

First the  $\tilde{H}$  equations:

$$\begin{aligned}\partial_k \tilde{H}_1(t, \tau, k) &= -\frac{1}{2\pi} n(\tau) (x(t) - x(\tau)) \left[ k n_e^2 J_0(k n_e |x(t) - x(\tau)|) \right. \\ &\quad \left. - k n_i^2 J_0(k n_i |x(t) - x(\tau)|) \right].\end{aligned}$$

$$\partial_k \tilde{H}_1(t, t, k) = 0$$

$$\partial_k \tilde{H}_2(t, \tau, k) = \partial_k \tilde{H}(t, \tau, k) - \partial_k \tilde{H}_1(t, \tau, k) \ln \left( 4 \sin^2 \frac{t - \tau}{2} \right)$$

$$\partial_k \tilde{H}_2(t, \tau, k) = \partial \tilde{H}(t, \tau, k) - \partial_k \tilde{H}_1(t, \tau, k) \ln \left( 4 \sin^2 \frac{t - \tau}{2} \right)$$

$$\partial_k \tilde{H}_2(t, t, k) = 0$$

$$\begin{aligned}\partial_k \tilde{H}(t, \tau, k) &= \frac{i}{2} n(\tau) (x(t) - x(\tau)) \left[ k n_e^2 H_0^{(1)}(k n_e |x(t) - x(\tau)|) \right. \\ &\quad \left. - k n_i^2 H_0^{(1)}(k n_i |x(t) - x(\tau)|) \right]\end{aligned}$$

The  $\tilde{H}_1^*$ ,  $\tilde{H}_2^*$ , and  $\tilde{H}^*$ , equations used in the starred operators  $K^*$  are defined in terms of the unstarred equations with no additional  $k$  dependence so their derivatives can use the results above.

The  $\tilde{M}$  equations are:

$$\partial_k \tilde{M}_1(t, \tau, k) = \frac{|x(t) - x(\tau)|}{2\pi} [n_e J_1(k n_e |x(t) - x(\tau)|) - n_i J_1(k n_i |x(t) - x(\tau)|)]$$

$$\partial_k \tilde{M}_1(t, t, k) = 0$$

$$\partial_k \tilde{M}_2(t, \tau, k) = \partial_k \tilde{M}(t, \tau, k) - \partial_k \tilde{M}_1(t, \tau, k) \ln \left( 4 \sin^2 \frac{t - \tau}{2} \right)$$

$$\partial_k \tilde{M}_2(t, t, k) = 0$$

$$\begin{aligned}\partial_k \tilde{M}(t, \tau, k) &= -\frac{i |x(t) - x(\tau)|}{2} \left[ n_e H_1^{(1)}(k n_e |x(t) - x(\tau)|) \right. \\ &\quad \left. - n_i H_1^{(1)}(k n_i |x(t) - x(\tau)|) \right]\end{aligned}$$



The  $\tilde{N}$  equations are:

$$\begin{aligned}
\partial_k \tilde{N}(t, \tau, k) &= -\frac{i}{2} |x(t) - x(\tau)| \bar{N}(t, \tau) \left[ k n_e^3 H_1^{(1)}(k n_e |x(t) - x(\tau)|) \right. \\
&\quad \left. - k n_i^3 H_1^{(1)}(k n_i |x(t) - x(\tau)|) \right] \\
&\quad + \frac{i}{2} x'(t) x'(\tau) \left[ k n_e^2 H_1^{(1)}(k n_e |x(t) - x(\tau)|) \right. \\
&\quad \left. - k n_i^2 H_1^{(1)}(k n_i |x(t) - x(\tau)|) \right] \\
\partial_k \tilde{N}_1(t, \tau, k) &= \frac{1}{2\pi} |x(t) - x(\tau)| \bar{N}(t, \tau) \left[ k^2 n_e^3 J_1(k n_e |x(t) - x(\tau)|) \right. \\
&\quad \left. - k^2 n_i^3 J_1(k n_i |x(t) - x(\tau)|) \right] \\
&\quad - \frac{1}{2\pi} x'(t) x'(\tau) \left[ k n_e^2 J_0(k n_e |x(t) - x(\tau)|) \right. \\
&\quad \left. - k n_i^2 J_0(k n_i |x(t) - x(\tau)|) \right] \\
\partial_k \tilde{N}_1(t, t, k) &= \frac{|x'(t)|^2 k (n_i^2 - n_e^2)}{2\pi} \\
\partial_k \tilde{N}_2(t, \tau, k) &= \partial_k \tilde{N}(t, \tau, k) - \partial_k \tilde{N}_1(t, \tau, k) \ln \left( 4 \sin^2 \frac{t - \tau}{2} \right) \\
\partial_k \tilde{N}_2(t, t, k) &= \frac{|x'(t)|^2}{2\pi} \left[ -2k n_e^2 \ln \left( \frac{k n_e |x'(t)|}{2} \right) \right. \\
&\quad \left. + 2k n_i^2 \ln \left( \frac{k n_i |x'(t)|}{2} \right) - k(n_e^2 - n_i^2)(2 + 2C - \pi i) \right]
\end{aligned}$$

As in the reference,  $C \approx 0.5772156649$  refers to the Euler–Mascheroni constant.

Finally, the  $\tilde{L}$  equations:

$$\begin{aligned}
\partial_k \tilde{L}_1(t, \tau, k) &= \frac{|x(t) - x(\tau)|}{2\pi} \left[ (k^2 n_e^3 J_1(k n_e |x(t) - x(\tau)|) \right. \\
&\quad \left. - k^2 n_i^3 J_1(k n_i |x(t) - x(\tau)|)) \right] \\
&\quad - \frac{1}{\pi} \left[ k n_e^2 J_0(k n_e |x(t) - x(\tau)|) \right. \\
&\quad \left. - k n_i^2 J_0(k n_i |x(t) - x(\tau)|) \right] \\
\partial_k \tilde{L}_1(t, t, k) &= \frac{k(n_i^2 - n_e^2)}{\pi} \\
\partial_k \tilde{L}_2(t, \tau, k) &= \partial_k \tilde{L}(t, \tau, k) - \partial_k \tilde{L}_1(t, \tau, k) \ln \left( 4 \sin^2 \frac{t - \tau}{2} \right) \\
\partial_k \tilde{L}_2(t, t, k) &= -\frac{1}{\pi} \left[ 2k n_e^2 \ln(k n_e) - 2k n_i^2 \ln(k n_i) \right. \\
&\quad \left. + k(n_e^2 - n_i^2) \left( 2 \ln \left( \frac{|x'(t)|}{2} \right) - \pi i + 2C + 1 \right) \right] \\
\partial_k \tilde{L}(t, \tau, k) &= -\frac{i}{2} |x(t) - x(\tau)| \left[ k^2 n_e^3 H_1^{(1)}(k n_e |x(t) - x(\tau)|) \right. \\
&\quad \left. - k^2 n_i^3 H_1^{(1)}(k n_i |x(t) - x(\tau)|) \right] \\
&\quad + i \left[ k n_e^2 H_0^{(1)}(k n_e |x(t) - x(\tau)|) \right. \\
&\quad \left. - k n_i^2 H_0^{(1)}(k n_i |x(t) - x(\tau)|) \right]
\end{aligned}$$

## CHAPTER IV

### FOLDED CHAOTIC WHISPERING-GALLERY MODES

Wave-chaotic optical cavities are of interest in applications because of the novel degrees of design freedom that are opened up when the geometric constraints of separability and symmetry are removed: spectral density, lifetimes and emission directionality can all be tailored in sometimes dramatic ways that go far beyond perturbative effects around separable special cases. Among the first examples are planar dielectric ovals that support *chaotic whispering-gallery modes* (WGMs)[24], where the anisotropic shape gives rise to highly universal directional emission patterns that can be explained based on the classical phase-space structure of the ray dynamics. From a theoretical point of view, this connection to classical ray physics is intriguing because the transition to chaos that occurs in generic nonseparable systems must now be studied in the presence of openness. The wave equation in this scenario exhibits quasibound states at complex wavenumber  $k = k_r - i\kappa$ ; here  $\kappa$  measures the escape rate which is related to the quality factor via

$$Q = \frac{k}{2\kappa}. \quad (4.1)$$

WGMs in oval resonators are special states that preserve long lifetimes comparable to those found in circular dielectrics [25], due to the fact that they are predominantly localized in the phase-space region corresponding to grazing incidence and hence total internal reflection at the dielectric boundary. When the invariant curves (tori) that foliate this phase-space region in the limit of circular symmetry are gradually broken up following the KAM theorem as applied to

convex billiards [26], regular WGMs become *chaotic* WGMs in which rays explore regions of phase space that may overlap with the escape window defined by the critical angle for total internal reflection. In Ref. [24], an approximate semiclassical quantization of these unconventional modes was proposed based on a separation of time scales between the fast whispering-gallery circulation and a slower spiraling-in toward the escape window, making it possible to identify *adiabatic invariant curves*. Their location then served as an initial condition for ray simulations of the escape directionality, caused by the mixed phase space in the vicinity of the escape window.

It has long been understood that no true WGMs can be sustained in circular domains if *waveguides* are attached, because this creates openings in the boundary that interrupt the whispering-gallery circulation. For a detailed study of this breakdown in the context of electronic microstructures with otherwise impenetrable walls, see Ref. [27]. This can be viewed as a special case of a theorem by Mather[28], who proved the non-existence of whispering-gallery invariant curves in planar billiards when the boundary is not everywhere convex. An example for Mather's theorem is the Bunimovich stadium (two semicircles joined by straight, parallel sides) [29], whose ray dynamics does not permit whispering-gallery orbits even if  $\ell$  is arbitrarily short, even though the weaker condition of non-concavity still holds. Strict convexity is therefore required in order to sustain WG circulation, but any waveguide openings will necessarily introduce corners where this condition breaks down.

By exploiting the preferential emission directions of chaotic WGMs in the near or far field, light can be coupled into and out of the resonator without contacting (and thereby perturbing) the boundary geometry directly. However,

monolithically attached waveguides offer some distinct advantages from an engineering point of view. In laser applications, they allow both efficient optical pumping and more complete collection of the emission. Although directional emission patterns from planar cavities can be made highly directional *in the plane* [30], losses by out-of-plane diffraction can be significant [31, 32, 33, 34]. With attached waveguides, such losses are minimized. Moreover, waveguides afford precise control over the number of input/output channels.

This has motivated several recent proposals to integrate chaotic cavities with waveguides [35, 36, 37, 38, 39, 40]. Because of Mather's theorem, however, almost all such proposals involve modes that are *not* of whispering-gallery type, achieving good confinement instead with states localized on periodic orbits: stable and unstable periodic ray orbits whose reflections occur far enough away from any waveguide openings will be insensitive to the boundary shape at the waveguide apertures. These periodic orbits exist with or without the presence of attached waveguides, and they make lasing possible even in the free-standing Bunimovich stadium [41].

The appearance of wavefunction scarring due to unstable periodic orbits in [41] illustrates that wave solutions of the Helmholtz equation can defy ray-optics predictions. This is also true for the predictions of Mather's theorem, and again the stadium billiard is a case in point: numerical solutions for closed (hard-wall) cavities [42] show that a form of chaotic WGM exists if the straight sides are sufficiently short.

We will describe whispering-gallery type behavior with a different topology, which can be described as *folded* chaotic whispering-gallery modes, cf. Fig. 4.1. This refers to the fact that the direction of whispering-gallery ray circulation

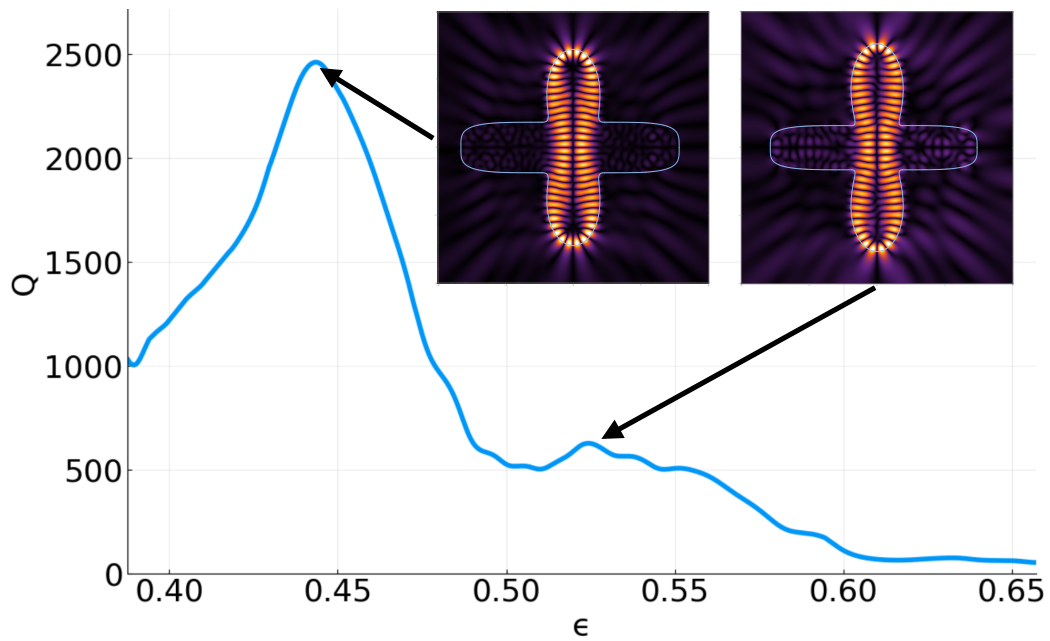


FIGURE 4.1. Spatial structure of a folded chaotic whispering-gallery mode (insets), and Q factor of the mode versus deformation parameter  $\epsilon$  at refractive index  $n = 2.4$ . The resonator deformation is defined in Eq. (4.2); attached waveguides of finite lengths are shown horizontal; their lengths are slightly unequal to remove reflection symmetry. False color represents field intensity. The real part of  $k$  (not shown) decreases approximately linearly from 14 to 12.5 as  $\epsilon$  increases.

underlying the modes reverses due to a self-intersection near the center of the cavity. The bowtie orbit of Ref. [43] also exhibits a self-intersection, but it – like all other such orbits we are aware of – gives rise to modes that explore the boundary only at isolated points corresponding to the discrete vertices where ray reflections occur. In Ref. [43],  $Q > 1000$  was obtained at relatively high refractive index contrast of  $n \gtrsim 3$ , corresponding to a critical angle for total internal reflection of  $\chi_c \approx \arcsin 1/n \approx 0.34$ . For such high index contrast, even Fabry-Perot cavities with near-normal angle of incidence provide similar Q-factors without the need for additional mirrors.

By contrast, all the high-Q modes in our design are localized predominantly in the whispering-gallery region of phase space, much further from the critical angle, even when the index contrast is below  $n = 2$ . The light is then well-confined by total internal reflection. Reminiscent of a figure-eight shape, folded chaotic WGMs have a waist that allows them to avoid two isolated sections of the boundary; but unlike stable periodic orbits such as the bowtie, folded chaotic WGMs explore the remainder of the perimeter in the same way as would be expected for conventional WGMs. In this sense, these types of modes come as close as possible to the circulating ray patterns that are strictly ruled out by Mather’s theorem.

The self-intersecting topology makes our design amenable to the incorporation of waveguides because the openings have only small overlap with the waist of the folded chaotic WGMs. Although the mode looks similar to Gaussian beam in the waist region, the latter are fundamentally different because they are always built upon stable periodic orbits, which in the simplest case requires a configuration corresponding to two focusing mirrors [44]. In our design, the reflections are near-

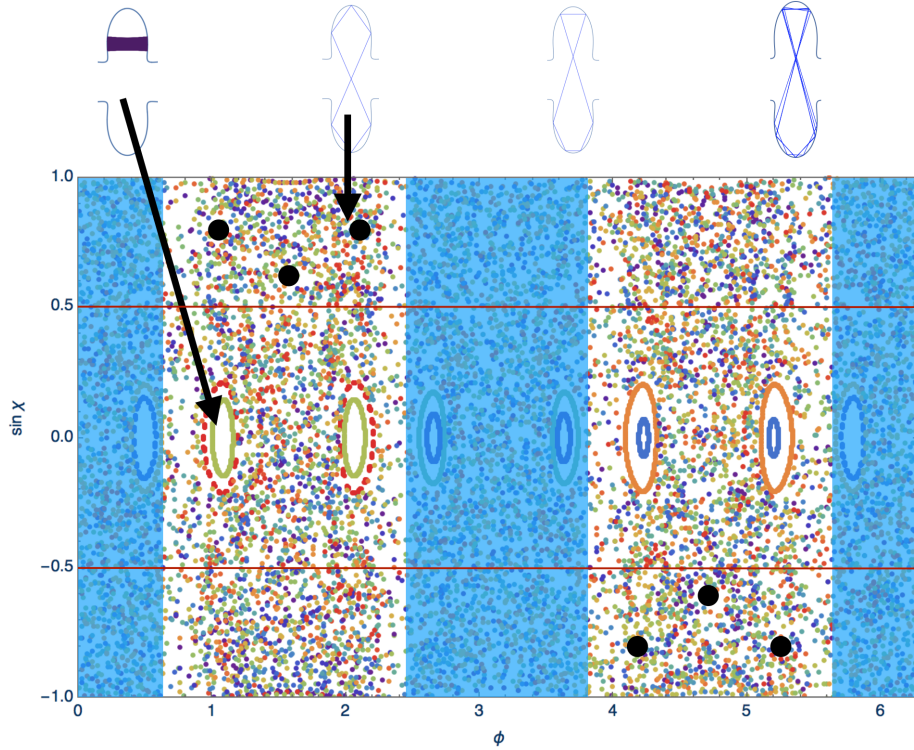


FIGURE 4.2. Poincaré surface of section with the curve parameter  $\phi$  as position and  $\sin \chi$  as momentum variable. Here,  $\chi$  is the angle between incident rays and the surface normal, so that  $\sin \chi = 1$  corresponds to grazing incidence. Ray trajectories show up as point clouds in the chaotic sea, or as one-dimensional lines for regular motion. The only regular regions are created by bouncing-ball orbits (top left); there are no invariant curves in the whispering-gallery region near  $\sin \chi \rightarrow 1$ . Shaded boxes indicate the intervals of  $\phi$  which describe the attached waveguides. Rays entering these regions will escape the resonator. The thin horizontal lines mark the critical angle for total internal reflection,  $|\sin \chi_c| = 1/n$ . Here and in all subsequent results,  $n$  can be viewed as the interior refractive index while the exterior refractive index is unity. Arrows identify the real-space orbits belonging to specific points in the Poincaré section.



grazing along the entire convex part of the boundary, and there is no focusing-mirror configuration so the modes are not paraxial.

#### 4.1. Cavity shape and ray phase space

By folding a WGM over itself and attaching waveguides in the avoided regions of the boundary, two distinct escape windows in phase space are created: one bounded by the critical line for refractive escape, and the other by the real-space locations of the waveguide openings. This is illustrated in the Poincaré surface of section of Fig. 4.2, depicting the phase space of a billiard parametrized in polar coordinates by

$$r(\phi) \propto 1 + \epsilon \cos(4\phi) \quad (4.2)$$

The curve parameter  $\phi$  is recorded on the horizontal axis, and  $\sin \chi$  is a measure of the conjugate momentum variable.

For the numerical wave calculations of Fig. 4.1, the parameter intervals omitted in the insets of Fig. 4.2 were replaced by waveguide segments whose shape is modeled as a “squircle”[45]. This curve has a polar-coordinate representation

$$r_{\text{WG}}(\phi) = \sqrt{a^2 |\cos \phi| + b^2 |\sin \phi|}$$

but was also shifted horizontally in order to connect smoothly with the unshifted curve of Eq. (4.2).

The waveguide portions of the boundary are shaded in the Poincaré section because they are irrelevant to the interior ray dynamics that makes the folded orbits possible. Figure 4.3 (e) illustrates a ray in the chaotic interior region that escapes into the waveguide opening after several reflections. The two self-

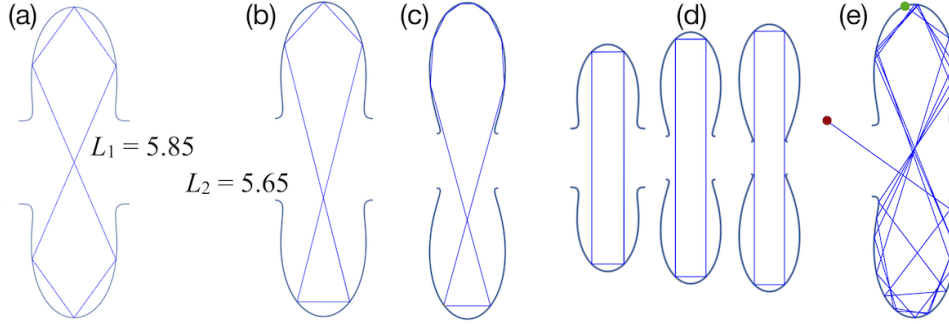


FIGURE 4.3. (a-c): Two self-intersecting unstable periodic orbits with angles of incidence  $\sin \chi \geq 0.6$  in the billiard shape given by Eq. (4.2) with  $\epsilon = 0.43$ . The lengths  $L_1, L_2$  of the orbits are slightly different. The same topology of orbits persists for a wide range of deformations. (c) is obtained from (b) by adjusting the initial conditions to generate eight instead of three reflections in the top half. For the rectangular unstable periodic orbit in (d), the increasing proximity to the corners of the waveguide aperture is illustrated for increasing  $\epsilon$ . (e) A ray trajectory launched in the cavity (green dot) and escaping through the waveguide opening (red dot). It retains the folded character of the orbits in (a), (b) for a short time.

intersecting periodic orbits shown in Fig. 4.3 (a - c) and in the inset to Fig. 4.2 have incident angles satisfying  $\sin \chi \geq 0.6$ , as exemplified for the six-bounce orbit by the black dots in the Poincaré section. Half of the bounce points occur at negative  $\sin \chi$ , corresponding to the reversal of angular momentum taking place at the self-intersection. There are no stable islands associated with any periodic orbits other than the bouncing-ball trajectories (leftmost inset) whose perpendicular angle of incidence precludes long-lived stable modes from forming.

The geometry also permits a rectangular periodic orbit whose angle of incidence has the fixed value  $\sin \chi \approx 0.707$ , but Fig. 4.3 (d) shows an important distinction to the self-intersecting orbits: as  $\epsilon$  increases, the corners of the waveguide aperture encroach on the orbit and eventually touch it. The resulting corner diffraction[46] will degrade the lifetime of any modes based on this orbit. The numerical computations to be described in the following have revealed high-

Q modes in cavities of the shape (4.2), that do show enhanced intensity near the rectangle orbit, but never exclusively on that orbit. Instead, the folded chaotic states consistently show high intensity overlapping with the folded orbits over a wide range of deformations  $\epsilon$  and attached waveguide widths.

## 4.2. Wave calculations

The wave patterns in Fig. 4.1 indicate that the mode is not supported by any one of the self-intersecting periodic orbits in Fig. 4.1 alone, but by a more extended phase-space region in their vicinity. The main panel of Fig. 4.1 follows a single mode over a range of deformations  $\epsilon$ , revealing an optimal deformation of  $\epsilon \approx 0.44$  at which this particular mode reaches  $Q \approx 2500$ . To characterize the parameter-dependence of the Q factor further, we carry out numerical simulations of the wave equation using two different methods. The first approach is a version of the boundary-integral method described by Heider [2] in which we directly search for the quasibound states satisfying outgoing-wave boundary conditions at infinity [47]. The second approach isolates the high-Q modes by harmonic inversion [48] of temporal field variation collected in a finite-difference time domain simulation with perfectly matched layer boundary condition (MEEP with post-processing by Harminv) [17]. In the direct quasibound-state calculation, we obtain complex wavenumbers  $k_{\text{QB}} = k - i\kappa$  to determine Q using Eq. (4.1).

### 4.2.1. Quasibound states

In the boundary-integral approach, we leverage the fact that the dielectric defining the billiard is uniform so that a Green-function description of the interior and exterior fields purely in terms of the boundary is possible. At the dielectric

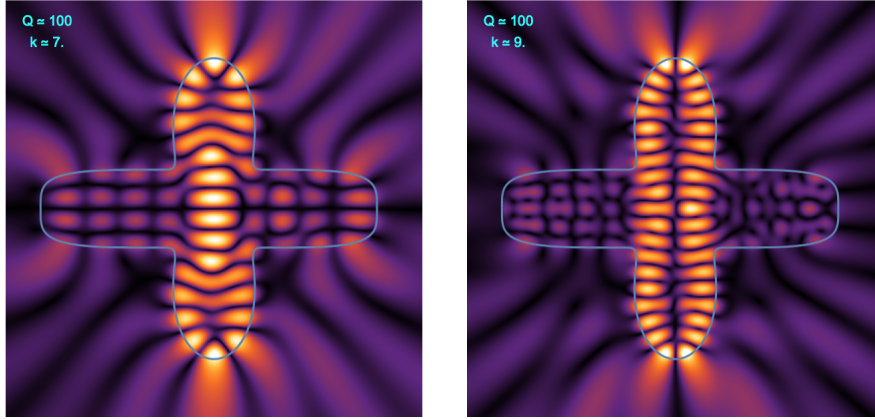


FIGURE 4.4. Small-cavity limit of the folded chaotic WGM, showing only low  $Q$  factors as the transverse width of the mode is comparable to the cavity size. Below  $k \approx 7$ , the wavelength is too long to observe the WGM like concentration of intensity near the top and bottom of the cavity. The horizontal waveguide stubs are attached in a way that smoothly matches the shape given by Eq. (4.2) for the vertical lobes. The refractive index is  $n = 2.4$  inside and  $n = 1$  outside, and the vertical lobes are described by Eq. (4.2) with  $\varepsilon = 0.444$ . In this and the following plots, one can discern even and odd parity with respect to reflections at the horizontal axis. Although we intentionally break reflection symmetry across the vertical axis by making the horizontal waveguide lengths unequal, the modes still show approximate antinodes (left) or nodal lines (right) along the vertical axis. This is because the cavity supporting most of the intensity is still left-right symmetric.

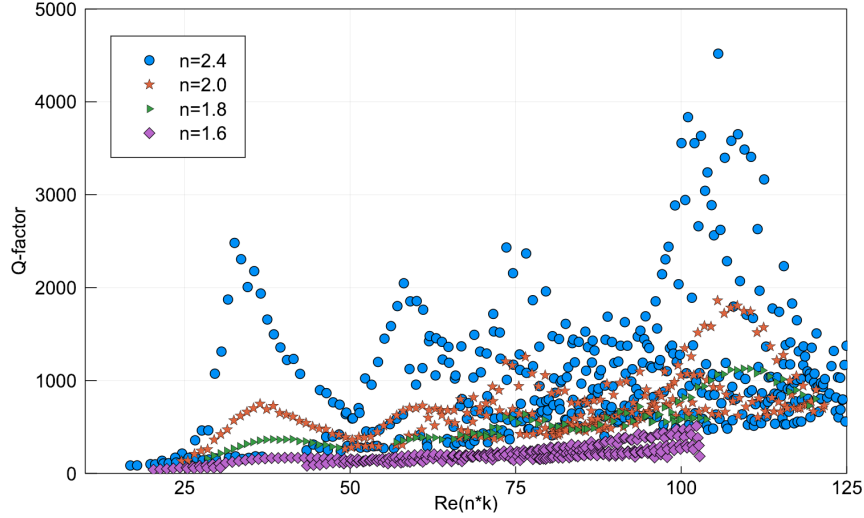


FIGURE 4.5. Wavenumber sweeps of the Q factor for different refractive indices  $n$ , discarding low-Q modes with  $\kappa \geq 0.05$  (for  $n = 1.6$ , only modes with  $\kappa \geq 0.2$  are shown). The deformation is  $\varepsilon = 0.444$ . The appearance of distinct Q-factor peaks as a function of quasi-bound state wavenumber is most pronounced at the largest refractive index,  $n = 2.4$ , and becomes nearly unobservable at  $n = 1.6$  (therefore, data for  $n = 1.6$  were not collected beyond  $nk \approx 106.5$ ). The peaks that do remain observable are approximately at the same values of  $nk$  for all  $n$ .

interface, the electric field is assumed to satisfy the boundary conditions for TM polarization (electric field perpendicular to the plane). After discretization along the interface, this leads to a nonlinear eigenvalue problem  $A(k_{\text{QB}}) \mathbf{u} = \mathbf{0}$  where  $\mathbf{u}$  contains the source values of the electric field and its normal derivative, and  $A$  is a matrix obtained from the field matching equations. A non-trivial solution requires searching for  $k_{\text{QB}}$  in the complex plane, which we do using a predictor-corrector method [2]. The method requires discretization of the boundary curve, and we generally found good convergence up to wavenumbers of  $k \approx 60$  by choosing 580 points. For additional analysis of the exponential convergence of the method with discretization density, see Ref. [2].

By definition, the boundary-integral method assumes that regions of uniform dielectric constant are bounded by closed curves, so we model the waveguides as

finite-length attachments, see Fig. 4.1. By varying the lengths of these waveguides (either together or independently of each other) we verified that the finiteness of the stubs has no significant effect on the mode structure: neither real parts nor imaginary parts of  $k_{\text{QB}}$  for the modes with figure-eight topology were affected unless their Q factor was below approximately 200 to begin with. Because the modes are built on classical ray orbits, they will not be found (with appreciable lifetimes) in small cavities. This is illustrated in Fig. 4.4 where the self-intersecting topology is barely discernible in the wave intensities. This raises the question whether the Q factors of such modes will increase *monotonically* with increasing cavity size, or equivalently with shorter wave length. To address this dependence, we fix the cavity geometry at  $\epsilon = 0.444$  to identify all the modes with lifetimes above a threshold of  $|\text{Im}(k_{\text{QB}})| = \kappa < 0.05$  with wavenumber  $k \lesssim 60$ . The particular choice of deformation corresponds to the maximum in Fig. 4.1 at  $n = 2.4$ , but the same phenomenology is observed at other values of  $\epsilon$ .

Figure 4.5 shows that the Q factors display a *non-monotonic* peak structure. The data are plotted for four different resonators with refractive indices of  $n = 1.6, 1.8, 2.0$  and  $2.4$ . The peaks are more pronounced for larger refractive index because the critical angle for total internal reflection decreases with  $\sin \chi_c = 1/n$ . By choosing the horizontal axis to display  $nk$  instead of the free-space wavenumber  $k$ , the peak positions for different  $n$  moreover line up to a good approximation. Since  $nk$  is the wave number inside the cavity, this indicates that the high-Q peak *locations* are determined by the interior wave patterns, not the monotonically  $n$ -dependent coupling to the surrounding free space. The absolute length scale of the cavity drops out of  $Q$  as per Eq. (4.1).

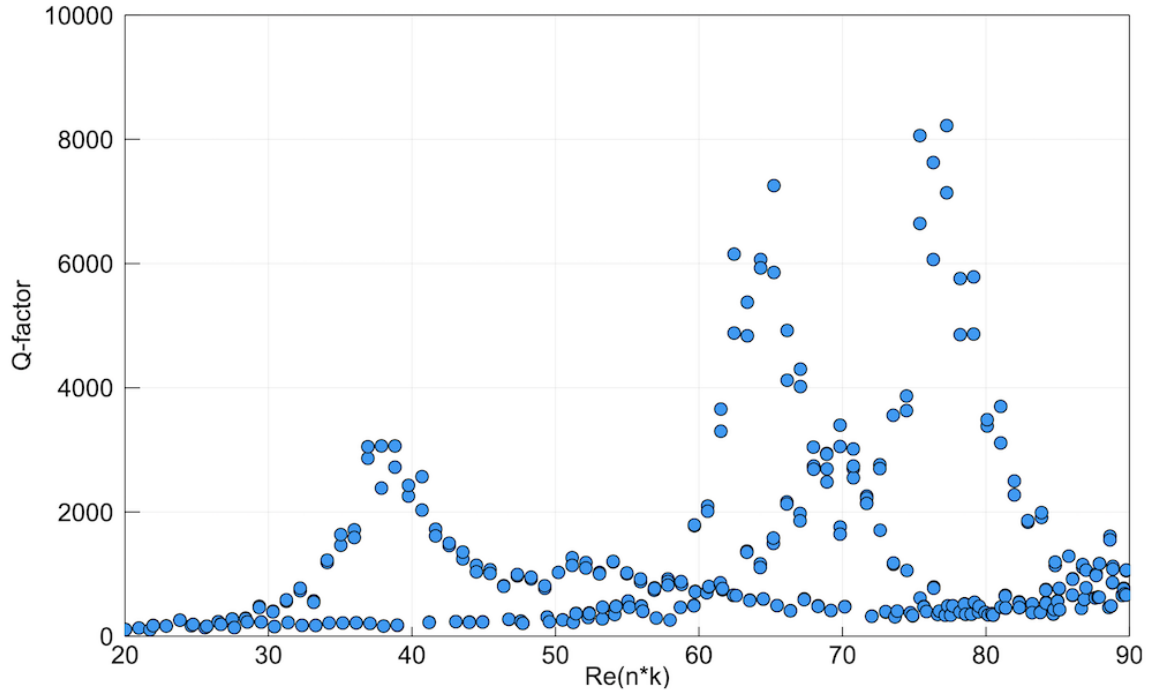


FIGURE 4.6. Q-factor scan versus interior wave number at deformation  $\varepsilon = 0.52$  and refractive index  $n = 2.4$ , showing modes with decay rate  $\kappa < 0.05$ .

The folded chaotic whispering-gallery modes are surprisingly resilient even to large waveguide openings. For practical applications, much narrower waveguides will typically be desirable because the input and output should be single mode. We show results for large openings because that is the regime in which the coexistence of whispering-gallery modes with an apparent violation of Mather's theorem is clearest. In particular, the openings are much wider than the wavelength, so they cannot be treated as small perturbations. We also observe the non-monotonic distribution of  $Q$ -factors shown in Fig. 4.5 at  $\varepsilon = 0.444$  for other deformations and waveguide widths. Figure 4.6 shows this for a higher deformation of  $\varepsilon = 0.52$ .

Figure 4.7 depicts the wave intensities of the highest- $Q$  folded chaotic WGMs in Fig. 4.5, with wavenumbers ranging from  $k \approx 13.6 \dots 44$  at  $n = 2.4$ . Each image represents a single quasibound state, not a superposition. The nodal structure

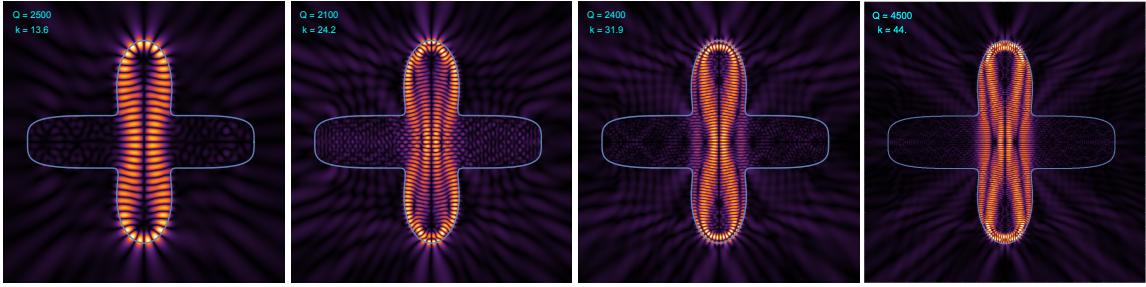


FIGURE 4.7. Field intensities for the modes corresponding to the first four Q-factor peaks in Fig. 4.5 at  $n = 2.4$ ,  $\epsilon = 0.444$ .

that decorates the underlying figure-eight patterns becomes more complex with increasing  $k$ , in much the same way that transverse nodes appear in higher-order Gaussian beams or radial nodes appear in whispering-gallery modes. The difference between those examples and the folded chaotic WGMs is that the nodal lines show wave dislocations typical of non-separable wave equations. Non-separability goes along with the chaotic ray dynamics of Fig. 4.2. Despite the increasingly complex nodal structure, all modes share the whispering-gallery like wave propagation along the convex parts of the boundary.

The Q-factor of any given mode may depend non-monotonically on the deformation parameter  $\epsilon$  of Eq. (4.2), as shown in Fig. 4.1. However, we find other high-Q modes over the entire range of deformations in Fig. 4.1, as illustrated by the examples in Fig. 4.8. The robustness of the folded morphology against deformation is another interesting feature that these modes share with conventional whispering-gallery modes in convex resonators.

#### 4.2.2. Time-domain results

To further validate the results of the boundary-integral method, we repeated the calculations for some of the modes using MEEP, which in particular allows



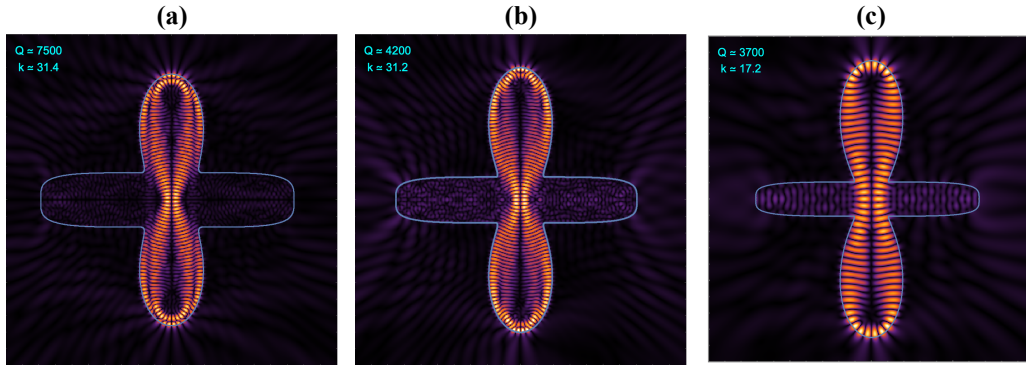


FIGURE 4.8. Field intensities for folded WGMs at different deformations: (a)  $\varepsilon = 0.52$ , (b)  $\varepsilon = 0.6$ , (c)  $\varepsilon = 0.7$ . The refractive index is  $n = 2.4$ . In (c), a smaller wavenumber is chosen, whereas (a) and (b) have comparable wavenumbers. The narrowing of the horizontal stubs is a result of the requirement that its tangents must match the curve described by Eq. (4.2) at the corners.

for a different modeling of the waveguide attachments. Instead of assuming them to be finite stubs, we allowed them to extend to the boundary of the simulation domain which includes a perfectly matched layer that prevents back-reflections of a wavepacket which was launched in one arm of the structure. After settling into a late-time decaying state, the wave field of a typical high-Q mode displays the same pattern found in the previous section, cf. Fig. 4.9 (a). Shown in Fig. 4.9 (b) is the same resonator at a roughly tenfold shorter wavelength. The comparison illustrates why we make a distinction between folded chaotic WGMs as in Fig. 4.9 (a) and scarred states. The concentration of intensity on the six-bounce unstable periodic orbit of Fig. 4.3 (a) identifies the mode of Fig. 4.9 (b) as a scarred state, whereas there is no single periodic orbit that describes the intensity of a folded chaotic WGM.

Having convinced ourselves that the same results can be obtained with both numerical approaches (boundary-integral and finite-difference time domain), we proceed with MEEP to look for folded chaotic WGMs in resonators with

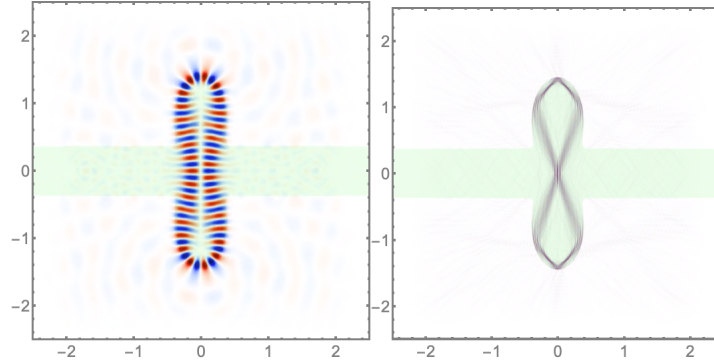


FIGURE 4.9. (a) Folded chaotic whispering-gallery mode as obtained in a finite-difference time domain computation for the same deformation  $\epsilon = 0.444$  and refractive index  $n = 2.4$  shown in Fig. 4.5. The wave number corresponds to the top of the first Q-factor peak,  $k \approx 13.6$  ( $Q = 2612$ ). Waveguide and resonator structure are underlaid as green shading, and the false-color scale represents the electric field. (b) Same deformation and refractive index, but approximately ten times shorter wavelength,  $k \approx 116.0$  and  $Q = 9898$ . (b) is discussed in section 4.3.

thinner waveguides, cf. Fig. 4.10. The size of the opening in Fig. 4.10 (a) is comparable to the wavelength, whereas it is approximately twice the wavelength in (b). The whispering-gallery circulation along the boundary, characteristic of the earlier results in Fig. 4.1, shows that the phenomenon is quite robust not only to variations in the refractive index, but also to changes in waveguide width.

### 4.3. Discussion

#### 4.3.1. Folded chaotic whispering-gallery modes in phase space

Individual modes of the folded chaotic WGM type do not shift or broaden significantly when the attached waveguides are shortened into stubs. From this we conclude that leakage into the waveguides is not the limiting factor for the lifetimes of individual folded chaotic WGMs. However, this is not straightforward to reconcile with the ray-tracing results depicted in Figs. 4.2 and 4.3 (e):

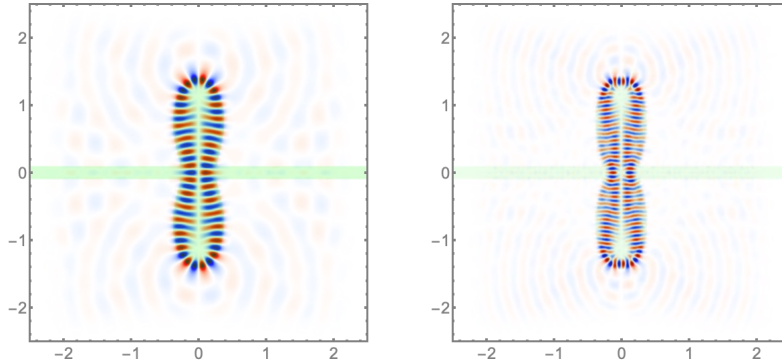


FIGURE 4.10. Two different modes with thinner waveguides, obtained by introducing a vertical offset between the two lobes of Eq. (4.2) and adjusting  $\epsilon$  to match them smoothly to the horizontal waveguides. The refractive index is  $n = 2.4$ . In (a)  $k \approx 13.3$  and  $Q \approx 1580$ , in (b)  $k \approx 22.4$  and  $Q \approx 2550$ .

A comparison between the numerically observed peak  $Q$  factors in Fig. 4.5 and the classical ray escape into the waveguides provides a first indication that dynamical wave localization is essential in the formation of folded chaotic WGMs. We find that up to a set of measure zero (the trapped unstable periodic orbits), no matter where in the classical phase space we launch a ray, it escapes into the waveguide openings much too fast to explain the  $Q$  factor found in the wave calculations.

The rapid ray escape can be viewed as a result of Mather's theorem, because the non-convex billiard shape implies that the bounce dynamics does not constitute a twist map, and consequently neither the Lazutkin nor the Poincaré-Birkhoff theorems apply [26]. What remains is a largely chaotic phase space as in Fig. 4.2, and no stable ray orbits around which high- $Q$  modes can be formed by the mechanism of paraxial optics [44].

However, as suggested by Fig. 4.3 (e), even in a chaotic region of phase space, the motion is nevertheless organized by the periodic orbits: each unstable periodic orbit is a periodic point of the Poincaré map which has stable and one

unstable manifolds. In the linear regime near a periodic point, they correspond to trajectories that either converge on, or recede from, that point. By launching a large number of rays from a small neighborhood of the periodic point and iterating the billiard map forward and backward in time, these manifolds are traced out, revealing a characteristic web of intersections [49] – the homoclinic tangle. In the main panel of Fig. 4.11 (a), this has been done for the six-bounce orbit corresponding to the thick solid dots in Fig. 4.2. Embedded in the intersections between the manifolds are higher-order periodic points corresponding to orbits such as the one shown in Fig. 4.3 (c). Guided by the homoclinic tangle, the phase space flow is far from random on intermediate time scales and in fact helps explain the directional emission from free-standing asymmetric cavities [50] by predicting at what positions the condition for total internal reflection is first violated for a chaotically diffusing trajectory.

To expose the relationship between the observed modes and the underlying ray phase space structure exemplified in Fig. 4.2, it is useful to project the numerical wave results onto the phase space by means of the Husimi function. Choosing  $\phi$  and  $\sin \chi$  as the coordinates for this projection, only the boundary fields are needed, and this is just what the boundary-integral approach provides [14]. Therefore, Fig. 4.11 shows one of the high-Q modes as obtained with this method. It corresponds to the top of the second peak in Fig. 4.5, and the second plot of Fig. 4.7. The wave intensity shown in the inset illustrates the appearance of nodal lines which in a conventional WGM would be the radial zeros. As seen in Fig. 4.7, successive Q-factor peaks at higher  $nk$  in Fig. 4.11 show additional such “radial” nodes, but the chaotic nature of the underlying phase space makes a rigorous classification in terms of radial nodal lines ambiguous.

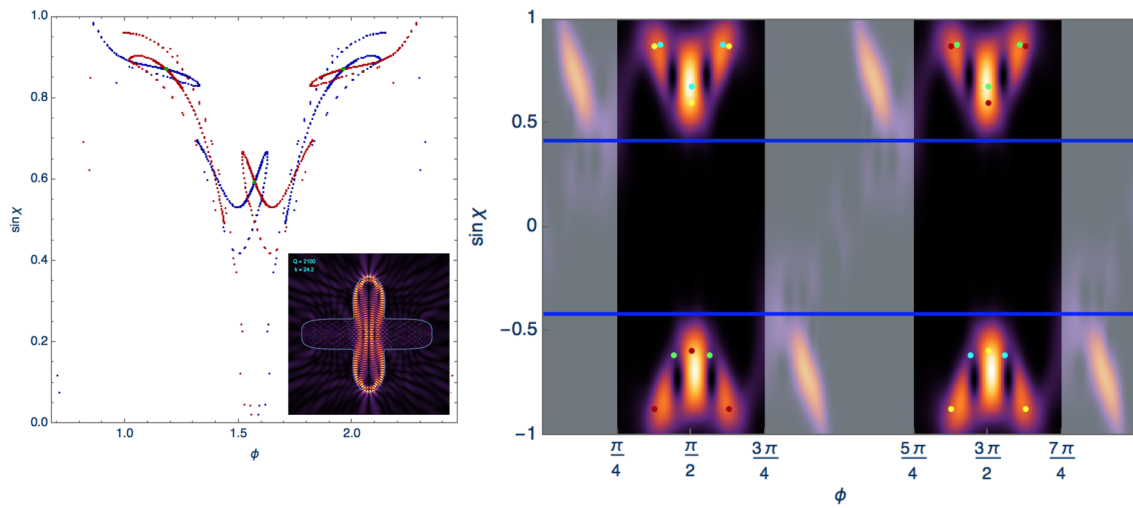


FIGURE 4.11. (a) Stable and unstable manifolds around an unstable periodic orbit. The zoomed-in region shown in (a) corresponds to the top left quadrant of the Husimi projection in (b). The real-space wave intensity of the mode in (b) is shown in the inset to (a). It is obtained for  $n = 2.4$  and  $\epsilon = 0.444$ . Shaded regions in (b) mark the waveguides, which were treated as escape windows in (a). Refractive escape is not considered in the ray simulation for (a), to get a more complete picture of the manifolds. Note the similarity in shape between the phase space structure and the areas of large Husimi weight.

The Husimi plot in Fig. 4.11 (b) instead classifies the mode according to the region of phase space by which it is supported – a procedure that is especially useful in this case because there are no stable ray orbits in the regions of the Poincaré section bounded by the escape conditions. The six-bounce periodic orbit whose manifolds are explored in Fig. 4.11 (b) is also shown in Fig. 4.11 (b), colored yellow and red overlaying the Husimi intensity of the wave solution (the two colors belonging to the two opposite senses in which the figure-eight is traversed). Shown in green and cyan are the self-intersecting period-five orbits. We have identified other periodic orbits with four to six bounces that are confined by total internal reflection in the same area of phase space, and it is not possible to uniquely assign regions of high Husimi intensity to a single orbit. However, Fig. 4.11 (b) does indicate unambiguously that the wave solution is in fact extended over a region of phase space bounded away from the critical angle  $\chi_c$  by the V-shaped tangle of manifolds of Fig. 4.11 (a).

Figure 4.12 illustrates the common phase-space region shared between all high-Q modes. Just like the real-space wave functions, the Husimi intensity shows some variability between different modes. In particular, the areas of highest Husimi intensity are not centered on any particular one of the many figure-eight type periodic orbits that exist in the cavity.

When interpreting the Husimi projection, the question arises whether our inability to assign a given mode to a unique unstable periodic orbit is merely a consequence of phase-space resolution. If this were true, it would mean that all the high-Q modes in our geometry are really of the scarred kind shown in Fig. 4.9 (b). However, this is not the conclusion we draw. With the length scale used here,  $k$  ranges from  $k \approx 7$  in Fig. 4.4 to  $k \approx 116$  in Fig. 4.9 (b). Within this approximate

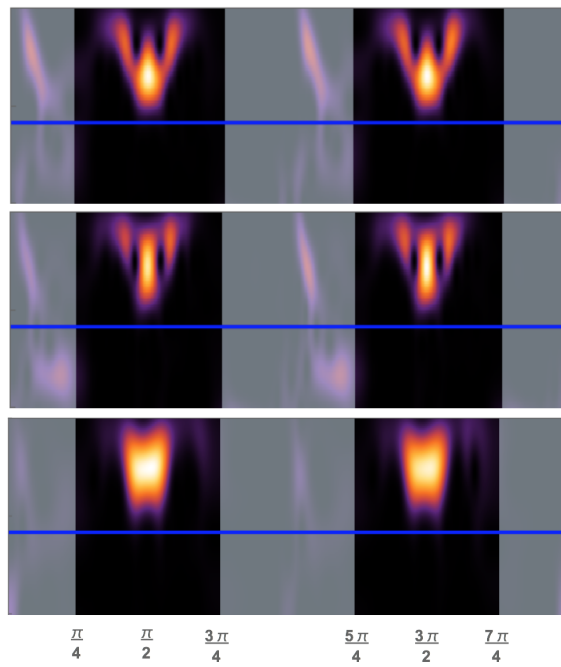


FIGURE 4.12. Comparison of Husimi plots for the same states shown in Fig. 4.8. Only the positive- $\sin \chi$  half of the phase space is displayed. The low wavenumber ( $k \approx 17.2$ ) in (c) leads to lower phase-space resolution than in (a) and (b) where  $k \approx 31.4$  and  $k \approx 31.2$ .

window, scarred modes belonging to a single unstable periodic orbit were not found below  $k \approx 70$ . The common feature of those lower- $k$  modes is instead the appearance of a caustic-like concentration of intensity following the curvature of the surface at  $\phi \approx \pi/2, 3\pi/2$  (the top and bottom in the wave plots).

In a convex billiard, whispering-gallery circulation leads to true caustics, but there is also a dense set of periodic orbits in the shape of inscribed polygons with lengths that accumulate at the circumference of the billiard. This particular property of inscribed polygonal orbits in the whispering-gallery region of phase space finds its counterpart in our non-convex geometry: there is a similar accumulation of periodic orbits with figure-eight topology, characterized by an increasing number of bounces along *either* the top *or* the bottom portion of the billiard. The orbit displayed in Fig. 4.3 (c) is an example.

Two other possible scenarios are known to produce wave solutions localized on phase-space regions where the classical billiard shows no stable structure: marginally stable periodic orbits [51, 52], and ray orbits that become stabilized only due to the “softness” of the dielectric billiard boundary as a function of incident angle [53, 54]. In these cases, the wave intensity is “scar-like” in the sense that it again coalesces onto identifiable periodic orbits, which is not the case for the folded chaotic WGMs.

### 4.3.2. Q-factor oscillations

The results shown in Figs. 4.5 and 4.6 are of particular practical importance: in designing resonators that exhibit modes with a folded topology, the geometric shape alone doesn’t guarantee that  $Q$  factors will increase monotonically with  $k$ , so the operating wavelength is constrained to match one of the  $nk$  ranges where



modes with high  $Q$  can be found. Whispering-gallery modes of the perfect circle do *not* show any comparable grouping into peaks of higher and lower  $Q$ ; instead, maximum attainable  $Q$  factors grow monotonically with  $nk$  because the modes with the lowest radial node number grow more and more concentrated at the surface, corresponding to grazing angle of incidence. Therefore, Figs. 4.5 and 4.6 show an aspect of the folded modes that distinguishes them from the conventional WGMs in convex resonators.

By varying the widths and lengths of the attached waveguides, we have ruled out that the periodicity in  $nk$  is due to threshold effects associated with the opening of new propagation channels. In an attempt to understand the  $Q$ -factor oscillations at the level of individual modes, we have singled out some high- $Q$  examples for closer investigation. In Fig. 4.5, the highest- $Q$  mode occurs at  $nk \approx 105.6$ . It is also shown in the right-most plot of Fig. 4.7 at  $k \approx 44$ . By following this mode over a neighborhood of deformation parameters  $\epsilon$  around the shown values, we found that no crossings or anticrossings with other modes occur. Such anticrossings can in principle lead to non-monotonic  $Q$ -factors as a function of a system parameter, in particular when whispering-gallery and chaotic modes coexist because they often depend differently on said parameters [55].

Husimi plots provide phase-space information about the classical structures supporting the folded chaotic WGMs, but their resolution is limited by the Fourier uncertainty relation between position  $\phi$  and angular momentum as measured by  $\sin \chi$  [50]. Individual modes also vary in the relative weighting between the neighborhoods of the five- and six-bounce orbits, suggesting that an analysis of the  $Q$ -factor oscillations in Fig. 4.5 is best done not at the level of individual modes, but by adopting a more global point of view.

Such a global perspective can often be obtained by investigating the connection between the classical periodic orbits and the density of states [56]. In open systems, the density of states is continuous but can exhibit resonant structure because it is proportional to the Wigner-Smith delay time [50]. Oscillations in the number of high- $Q$  modes could be interpreted as oscillations in a density of states in which short-lived resonances are not counted. In order to relate these oscillations to periodic orbits, we explored the approach of reference [57], where beats between a small number of trajectories with similar actions in the periodic orbit sum were successfully used to interpret structure in the density of states for a Hénon-Heiles Hamiltonian. Using the period-orbit lengths  $L_1$  and  $L_2$  from Fig. 4.3 (a, b) to obtain the actions  $S_{1,2} = nkL_{1,2}$ , we arrive at an estimate for the beating period in Fig. 4.5 of

$$\Delta(nk) \approx \frac{2\pi}{|L_1 - L_2|} \approx 30 \quad (4.3)$$

at refractive index  $n = 2.4$ . Although this is in reasonable agreement with the spacing between the first two peaks in Fig. 4.5, we have not yet been able to reproduce the correct dependence of the numerically observed peak positions on deformation parameter  $\epsilon$ . In particular, we have found additional periodic orbits with larger values of  $|L_1 - L_2|$  that should appear with comparable amplitudes in the periodic-orbit sum for the density of states, so it remains to be seen if a refined version of Eq. (4.3) will be able to preserve the appealing simplicity of this interpretation in terms of periodic-orbit beats.

#### 4.4. Conclusions

We have numerically calculated the quasi-bound state wave functions of a series of planar dielectric cavities with attached waveguides that support the

formation of folded chaotic whispering-gallery modes. We found that for a large range of wavelengths, refractive indices as well as shape deformations it is possible to sustain high quality factors despite the fact that the ray dynamics permits long-lived, trapped trajectories only for a discrete set of unstable periodic orbits. The figure-eight topology of these orbits imprints itself on the wave solutions even though there is no one-to-one correspondence between individual modes and single periodic orbits.

As a result of this folding, the modes are confined by total internal reflection in the uninterrupted convex parts of the resonator boundary, while at the same time exhibiting a waist that reduces their overlap with the opening to the attached waveguides. Because these openings are necessarily in violation of Mather's theorem, the existence of folded chaotic WGMs with Q-factors larger than  $10^3$  is a wave localization effect. This localization is visualized with the help of Husimi projections which show that the long-lived modes are supported by a region of the ray phase space that coincides with the heteroclinic/homoclinic tangles of the unstable periodic orbits whose intensity pattern is also discernible in the real-space wave plots.

As seen in the real-space plots, there are varying degrees of emission into the free space surrounding the structures. In this paper, the focus has been on the fact that high Q can be preserved in the presence of waveguide openings, because the latter are more intrusive than the curvature-induced violation of the total-internal reflection condition at the dielectric-air interface. Having characterized the long-lived states for a range of deformations based on the resonator shape given in Eq. (4.2), an important next step is to investigate the emission from the whispering-

gallery portions of the modes for other resonator shapes while still preserving the phenomenology of the folded chaotic WGMs presented here.

Explorations of modified shapes are currently in progress, with the additional goal of further elucidating the Q-factor peaks discussed in subsection 4.3.2. By breaking the reflection symmetry of the cavity and going to higher wavenumbers in the wave simulations, we expect to improve upon the diagnostic value of the Husimi projections. We have already performed simulations for structures without spatial symmetries in order to make contact with previous work on unidirectional coupling [37], but additional work is needed to optimize the Q factors of those shapes.

An alternative to the quasibound-state analysis presented here is to investigate the resonances in transmission or reflection with the waveguides as input and output. In the stadium as the prototypical chaotic billiard, the transmission through attached leads has been studied in [58] in the context of electronic transport, i.e., with impenetrable walls. Sharp resonances are found to be associated with all regions of the chaotic phase space, leading to spectral statistics governed by level repulsion. In our system, the only long-lived modes are of the quasi-WGM type described here, and their groupings shown in Fig. 4.5 are not described by a universal random-matrix distribution. This goes hand in hand with the observation that no anti-crossings occur when varying the deformation parameter  $\epsilon$  of Eq. (4.2), indicating that all modes respond to such variations in unison. A study of the transmission statistics for waveguide-coupled resonators of this type will provide insight into the interplay of the two types of escape windows in the phase space depicted in Fig. 4.2, where chaotic ray dynamics dominates similarly to the stadium, while at the same time the mode structure appears to be much simpler provided that low-Q states are discarded.

## CHAPTER V

### CONSTANT WIDTH CAVITIES

#### 5.1. Introduction

The wheel is one of the most useful inventions in history, primarily because of its circular geometry. It is a shape of constant width, rotate it by any amount and its height remains the same, which makes for a smooth ride. Although the circle is the most well known shape of constant width, there are others. The Reuleaux triangle is a three “sided” shape similar to a triangle but with rounded edges. It retains the property of constant width and has found some applications in the rotary engine. Other odd-sided polygons can also be transformed in a similar way.

While these shapes have mainly been geometric curiosities, smooth curves of constant width have been studied in the context of microwave cavities and have rather interesting properties [14]. An unlimited number of different smooth curves of constant width can be created where the  $x, y$  coordinates are the real and imaginary parts of a complex function

$$z(t) = -ia_0 - i \sum_{n \in \mathbb{Z}} \frac{a_n}{n+1} (e^{i(n+1)t} - 1), \quad t \in [0, 2\pi), \quad (5.1)$$

with the constraints that  $a_{-n} = a_n^*$ ,  $a_1 = 0$ , and  $a_{2n} = 0$  for  $n > 0$  [59]. If the constants are chosen properly, the curve will have completely smooth edges at all points, unlike the Reuleaux triangle in Fig. 5.1. These curves have no continuous or discrete rotational symmetry and no mirror symmetries. An example of this boundary shape is shown in Fig. 5.1 and this parameterization is used throughout this chapter.

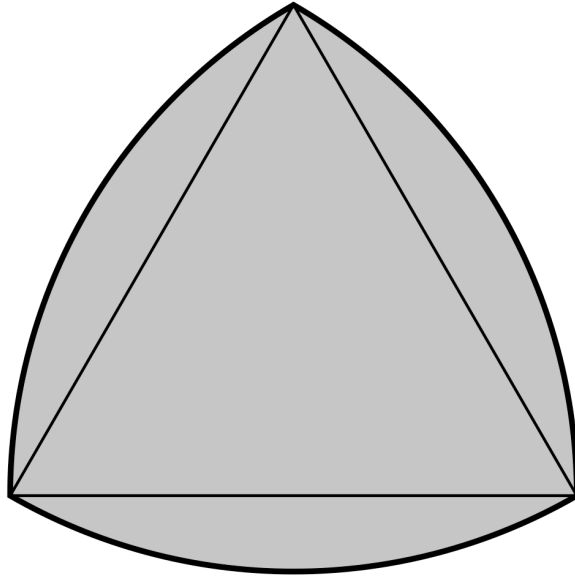


FIGURE 5.1. Reuleaux triangle

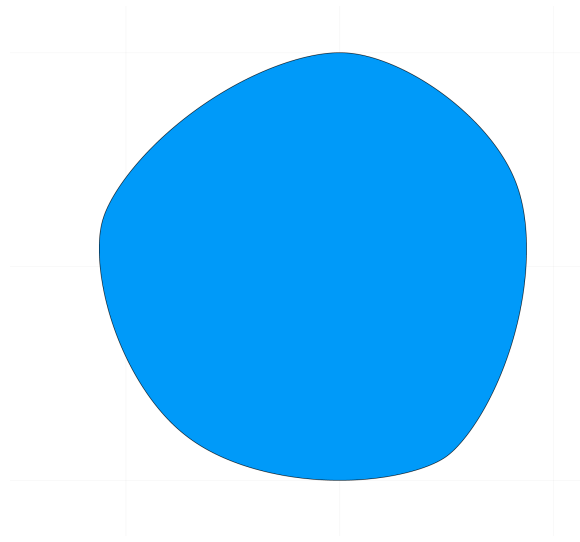


FIGURE 5.2. Smooth curve of constant width based on Eq. (5.1)

In the context of billiards, these shapes have a unidirectional property such that if the particle in a billiards simulation is released with a clockwise or anti-clockwise rotational direction, it will preserve that rotational direction at all future times. This is a property that we are familiar with in the case of a circular billiard, because due to conservation of angular momentum the trajectories follow invariant curves that are simply straight lines. However in the case of these shapes the SOS is nearly completely chaotic. Nevertheless when calculating an SOS for a constant width billiard, if a point begins in the upper half of the SOS its trajectory will remain there, and likewise for the lower half. Fig (5.3) shows the SOS for a curve with parameters (as described in Eq. (5.1))  $a_0 = 12, a_2 = 3i/2, a_5 = 3$  and all other coefficients zero. Other than some structures around  $\sin \chi = 0$  which correspond to bouncing ball orbits and  $\sin \chi = 1$  which are WGM type patterns, the SOS is chaotic. The lower half representing clockwise rotation is completely empty. The figure also shows the KAM barrier region at  $\sin \chi = 0$ , these correspond to bouncing ball orbits that remain stable under the deformation from the circle. In the classical case, they are impenetrable.

## 5.2. Constant Width Cavity in Wave Regime

Given this interesting behavior in the billiards picture, we would like to understand how it behaves in the wave regime. For a closed cavity system, this has been previously investigated [14]. Superconducting microwave cavities were constructed using the shape above and excited at various frequencies to interrogate the spectrum. While classically, crossing the KAM barrier at  $\sin \chi = 0$  is forbidden, in the wave regime this can take place via tunneling. While the spectrum appeared to contain sharp single resonances, most resonances turned out to be composed

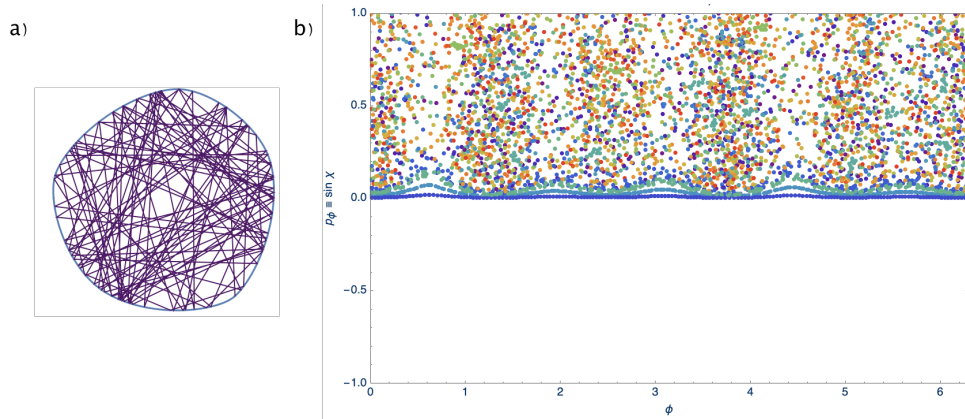


FIGURE 5.3. (a) Curve of constant width and typical chaotic trajectory. (b) SOS for the shape.

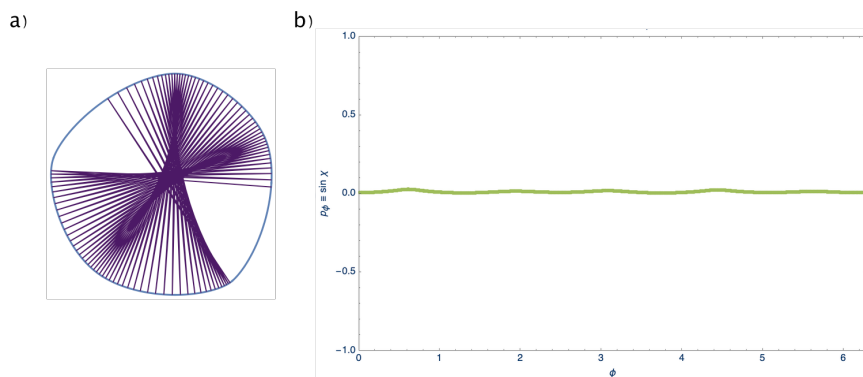


FIGURE 5.4. (a) Typical bouncing ball trajectory (b) SOS in the KAM barrier region for bouncing ball orbits.



of narrowly separated quasi-degenerate doublets. These doublets are associated with tunneling from one half of the SOS through the barrier to the other half, thus representing a switch of rotational direction. A complementary form of chaos-assisted tunneling and the resulting splittings of eigenvalues was first seen in a microwave cavity experiment for the annular billiard [60]. However in this context the tunneling occurred between two regions of regular dynamics separated by a region with chaotic dynamics. In the constant width billiard, the tunneling occurs between states that exist in the chaotic sea and tunnel through a region of regular dynamics.

The study in the closed microwave system was able to categorize the resonances into different types based on their occupation of phase space. These include the bouncing ball around the KAM barrier, WGM type modes with wave functions localized close to the boundary, island modes which are localized around small periodic orbit islands but away from the  $\sin \chi = 0$  line, and hybrid modes which have wave functions mainly away from the KAM barrier but also some amount around  $\sin \chi = 0$ . In the open system we were able to find resonances similar to these families, as shown in Fig. 5.5. The corresponding Husimi distributions are shown in Fig. 5.6.

### 5.3. Non-Reciprocity and Time-Reversal Symmetry

Under most normal circumstances, the laws governing the time evolution of electromagnetic waves ensure the reciprocal response of a system. Intuitively, this implies that given an optical system with a source at one input port and a detector at one output port, if one measures the optical response of the system and then exchanges the input and the detector, thus running the system in reverse,

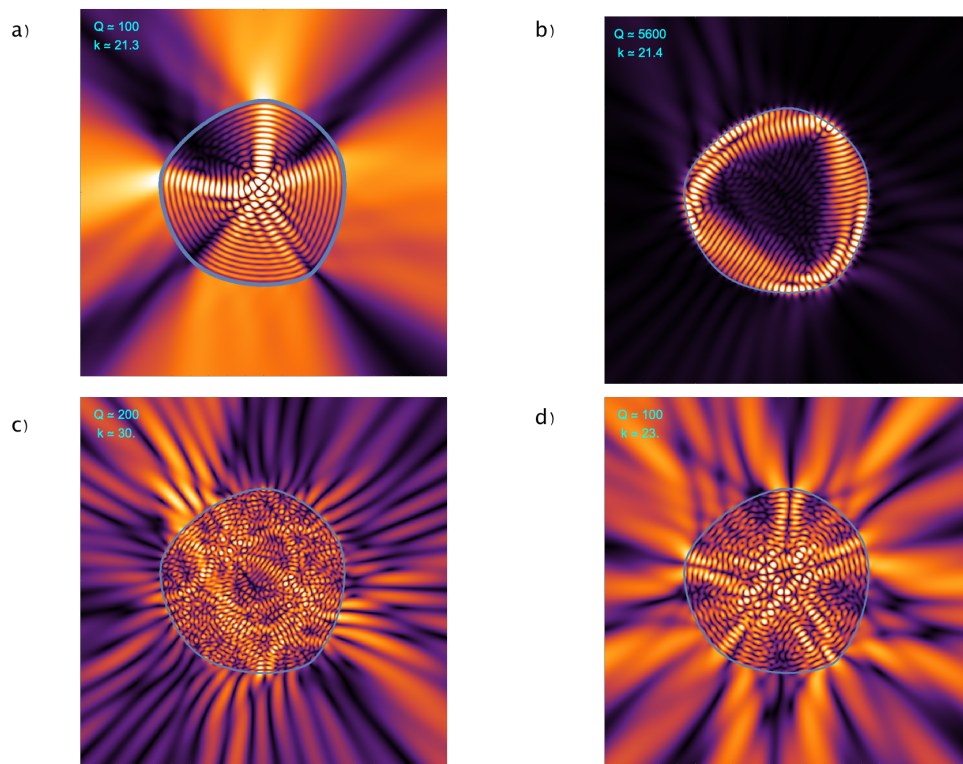


FIGURE 5.5. Mode families for the constant width cavity (a) Barrier KAM mode (b) WGM mode (c) Island mode (d) Hybrid mode

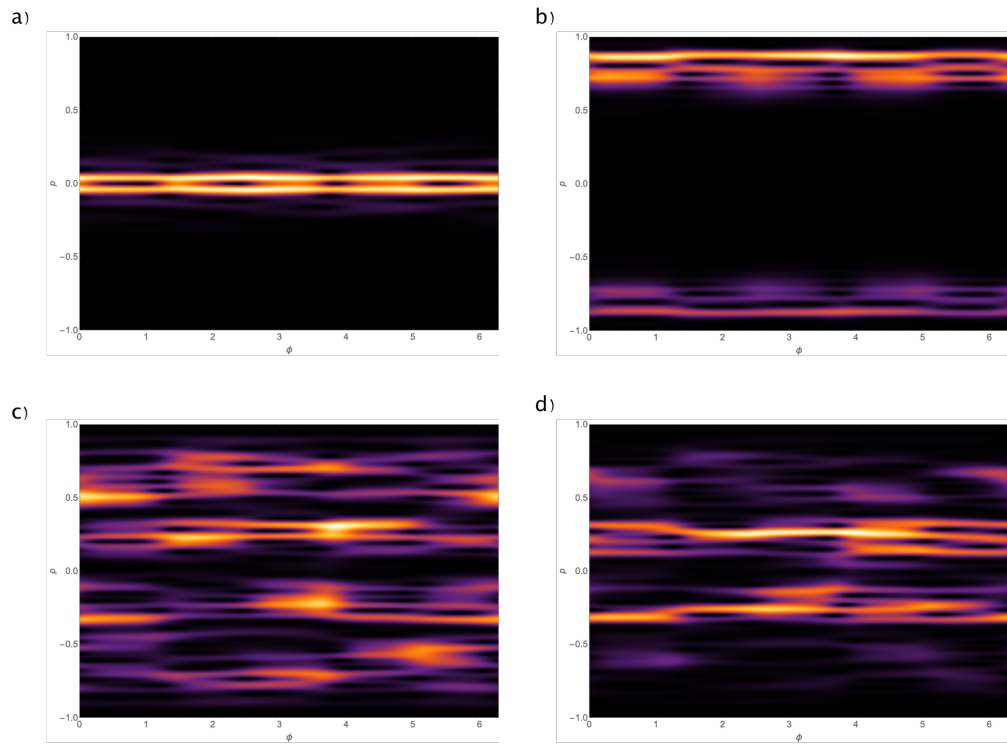


FIGURE 5.6. Husimi distribution for the mode families for the constant width cavity, corresponding to the modes in Fig. 5.5 (a) Barrier KAM mode (b) WGM mode (c) Island mode (d) Hybrid mode

the response should be unchanged. This property is quite useful in the analysis of optical systems such as beamsplitters, couplers, lenses, and so forth [61]. There are some circumstances under which this mostly true assumption can be modified. One form of non-reciprocity involves an external bias such as an externally applied magnetic field in a linear time independent medium. These are commonly called Faraday rotators and have been employed in the construction of optical isolators. Another possibility is a time varying linear medium; in this case there is a time-reversal symmetry that is broken by an external bias, such as an optomechanical modulation. A third possibility is use of linear materials coupled to nonlinear materials, where the system is self-biasing. These nonlinear effects do have some limitations such as a limitation of excitation in one direction at a time, which limits the applications for isolators [62].

Some general conditions are also outlined regarding non-reciprocal optics in [62]. Of these two are important for our discussion of the constant width cavity. First, it is established that a breaking of time-reversal symmetry is always a necessary condition for non-reciprocity. Second, the condition of non-reciprocity is equivalent to time-reversal symmetry breaking in lossless systems, and by extension in systems with negligible loss. The constant width billiard was shown [63] to have chaotic dynamics that spontaneously break time-reversal symmetry. The Bohigas, Giannoni, and Schmidt conjecture [64] posits that the statistical properties of eigenvalue levels of classically chaotic systems follow those of general classes of random matrix ensembles. These ensembles are large numbers of matrices populated with random numbers chosen from a Gaussian distribution. The resulting statistical distributions of eigenvalue level spacing depend on the general matrix properties of the ensemble. If the matrices are constructed to be

real and symmetric, they are part of the Gaussian orthogonal ensemble (GOE). If the matrices are constructed as Hermitian, the ensemble is called the Gaussian unitary ensemble (GUE). For time-reversal invariant systems, one expects statistics to follow the GOE, for a non-rotationally symmetric system with broken time-reversal symmetry, the GUE is expected. A constant width billiard of the type we study here has been shown [63] to have level spacing consistent with the GUE. This demonstrates that although the billiards dynamics are inherently time-reversal symmetric, the chaotic dynamics spontaneously break that symmetry. In the closed cavity experiment with microwave cavities, a modified form of the GUE was constructed to account for the incomplete chaotic dynamics (regular region of KAM tori forming the barrier region). This modified RMT ensemble was properly matched with experimental results. Moreover, the GOE ensemble was not matched against the level spacings or other spectral properties. This is attributed to the unidirectional response of the cavity.

Given the previous results, we can establish that the constant width cavity has the required properties for a non-reciprocal response. The system has been shown to exhibit dynamic time-reversal breaking in the closed cavity. In the context of optical cavities, the openness of the system is controlled by the index of refraction. This allows the transition from a closed to open system to be controlled parametrically. Although the radiation outside the cavity is in some sense a “loss” from the cavity system, it is not lost in the sense of thermal heating or thermodynamic irreversibility. Instead radiative loss is a property of the boundary conditions we impose to establish the resonance condition as in Eq. (2.2). We investigate the form that this non-reciprocity takes. Since the special feature of this system in the ray picture its unidirectional chaotic dynamics, we would expect

unidirectionality to be a factor. In the sections below, we show that this cavity can support chiral modes with radiation from the boundary in regions that differ depending on which chiral mode is present. We argue that this enables a non-reciprocal optical response. Suppose that clockwise chiral light is coupled into the cavity at a boundary location of maximal intensity for the clockwise mode and a sensor placed at another area of maximal intensity. In the case that the source and detector were swapped and the system run in reverse, i.e. the clockwise chiral direction flipped to anti-clockwise, light coupled into the system would not be preferentially radiated at the same locations on the boundary. The anti-clockwise light has maximal intensities in different regions than the clockwise. Therefore the ratios of the transmitted and received fields would be different under this exchange, which is the definition of non-reciprocal optical response in [62]. Although the time-symmetry reversal breaking spectral statistics are seen in the classical dynamics and the wave dynamics in a closed cavity, because these systems are bounded it is not possible to probe a non-reciprocal response to an external detector. In that sense exploring this geometry in an open setting with openness parameterized as a function of index of refraction in the cavity medium is an important extension of the previous studies.

#### 5.4. Constant Width Optical Microcavities

Scanning over regions of  $k$ -space, we were able to identify the nearly degenerate doublets described in the microwave cavity. When looking at superpositions of these modes, we were able to recover the unidirectional chiral modes that can be formed as a superposition of the modes comprising the doublets. By choosing an appropriate phase angle between the doublet modes, superpositions

showing the clockwise and anti-clockwise traveling wave components may be recovered. This is likely to be true with the modes described in [14], however since that study was for closed cavities the radiative pattern outside the cavity was inaccessible. In the open microcavity system, the emission pattern also demonstrates the chiral nature of these superposition modes. Given the small separation of the modes and the width of the resonances themselves, it should be possible to simultaneously excite both modes and therefore establish the counter-propagating traveling waves.

As an example, we will examine the modes found for a constant width cavity with  $n = 1.6$ , with the same curve parameters as for B1 in [14]. One doublet in the WGM regime was found at the closely spaced wavenumbers

$$\begin{aligned}
 k_1 &= 45.730158 - 0.068421i \\
 k_2 &= 45.730187 - 0.068436i.
 \end{aligned}$$

The separation between the two is only  $k_1 - k_2 = (-2.855 + 1.5106i)10^{-5}$ . These have a quality factor of around 300, but other higher Q modes can also be easily found, and by raising the index of refraction the quality factor also rises. Higher Q resonances have a correspondingly smaller doublet spacing, the relatively large spacing here was useful for investigating as it made tracking deformations of the doublet easier to follow. Figure 5.7 shows the wavefunction and Husimi distribution of the quasi-degenerate pair. Although the resonances appear almost identical, they can be combined in a superposition with an additional phase added to show the chiral modes that result. Figure 5.8 shows a superposition of the

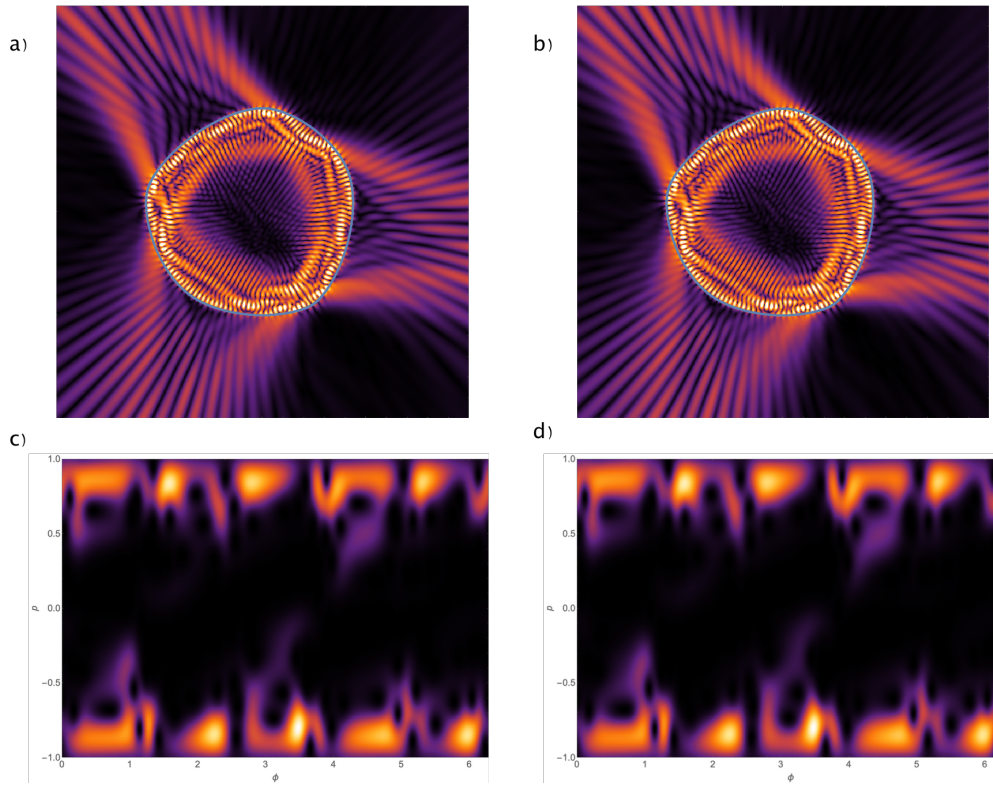


FIGURE 5.7. Wave functions and Husimi distributions for quasi-degenerate doublet at  $k \simeq 45.73$

doublet modes with a phase factor of  $i, -i$  respectively. When combined in this manner, the chiral nature of these modes becomes apparent.

### 5.5. Deformation From Constant Width

In the ray limit where  $k$  becomes large, the constant width of the cavity is linked to its unidirectional property. We examined deformations of the constant width billiard which scaled the vertical axis relative to the horizontal. Since this curve is not symmetric in any way, a deformation in this way serves as a generic deformation. The deformation took the form of

$$x'(t) = \text{Re}(z(t)), \quad y'(t) = (1 + \eta)\text{Im}(z(t)),$$



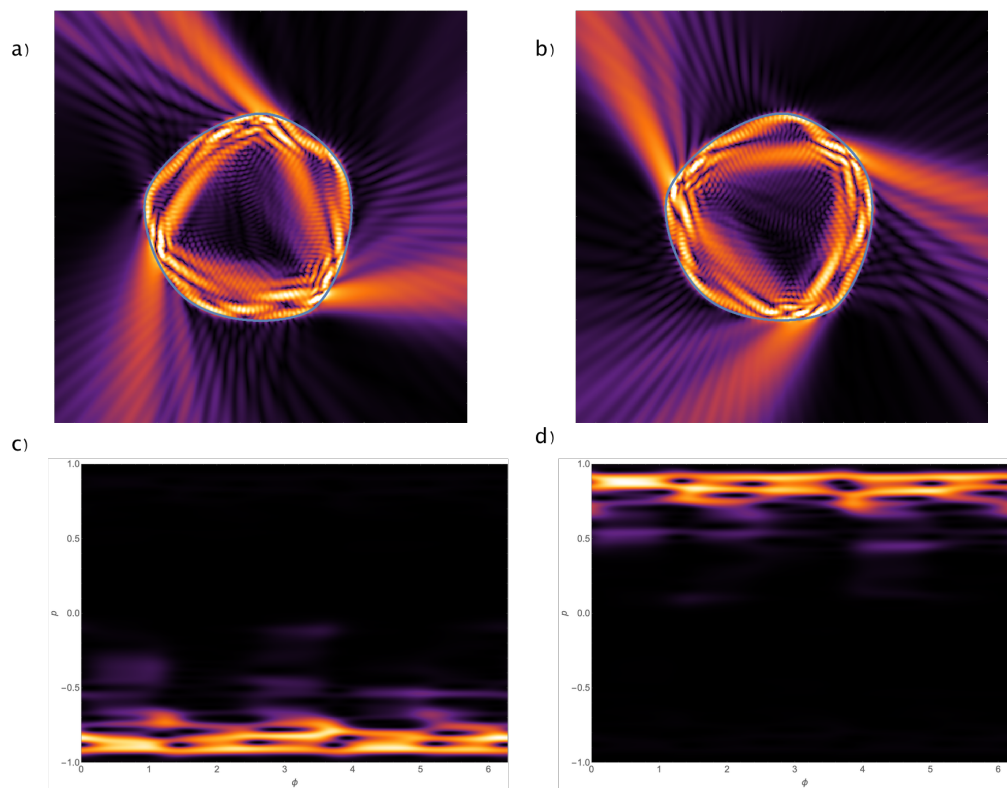


FIGURE 5.8. Wavefunctions and Husimi distributions for superpositions of modes from Figure 5.7 with phase factors  $\phi = i$  in (a), (c),  $\phi = -i$  in (b), (d).

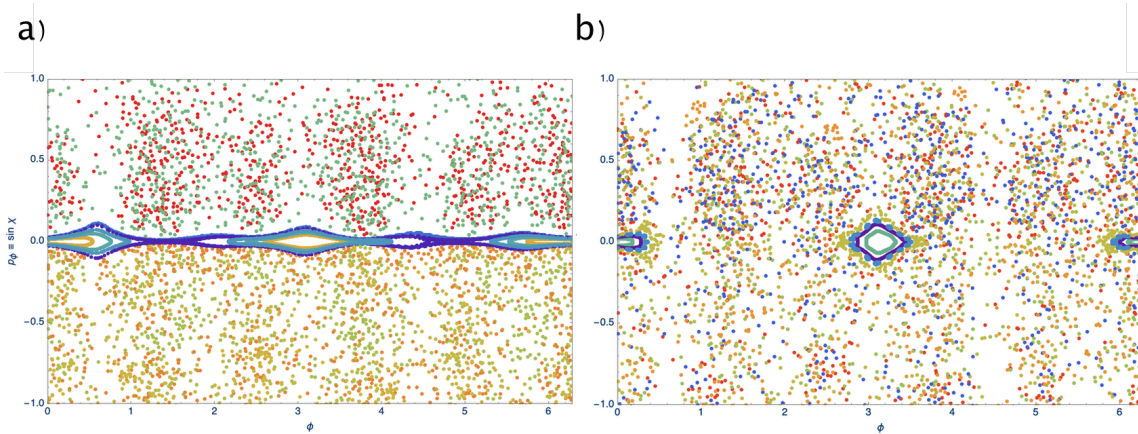


FIGURE 5.9. SOS for vertical deformation of constant width billiard. (a)  $\eta = -0.001$  (b)  $\eta = -0.02$

where  $z(t)$  is as defined in Eq. (5.1) and  $\eta \simeq 1$ . In Figure 5.9 the effects of two small values of  $\eta$  are shown. Very quickly the barrier region at  $\sin \chi = 0$  is destroyed and the unidirectional nature of the system is lost. To see the effects of this on the chiral mode pairs we followed the resonance as  $\eta$  was changed in both the positive and negative direction. At each deformation the doublet pair was resolved and several measures calculated. From the Husimi distributions we calculated the Husimi imbalance which we define as the excess intensity in the upper half of the distribution versus the lower half. This quantity is in arbitrary units based on normalizing the overall distribution at each step. A positive value for this quantity represents more weight in the anti-clockwise circulation and a negative value represents more weight in the clockwise direction. Additionally the wavefunction overlap between the doublet modes was calculated as the inner product of the wavefunction values on the boundary. If the doublet modes are truly orthogonal then this overlap should be zero. We also calculated the difference  $\text{Re}(k_1) - \text{Re}(k_2)$ . Figure 5.10 shows these quantities plotted together. When the modes overlap is at a minimum of zero, this also corresponds to a perfect balance in the Husimi distributions, where the clockwise and anti-clockwise pairs are present in equal balance. As the overlap increases, an imbalance in one direction or the other occurs. There is also an interesting point at a deformation of  $\eta = -.02$ , where the spacing between the modes becomes vanishingly small. In this case, we argue that even an extremely narrow excitation of the resonance would be able to excite both chiral directions at the same time. Although the billiards SOS shows a breakdown of the KAM barrier right at very small deformations, it was still possible to find chiral states with balanced Husimi distributions and distinct unidirectional patterns at larger deformations.

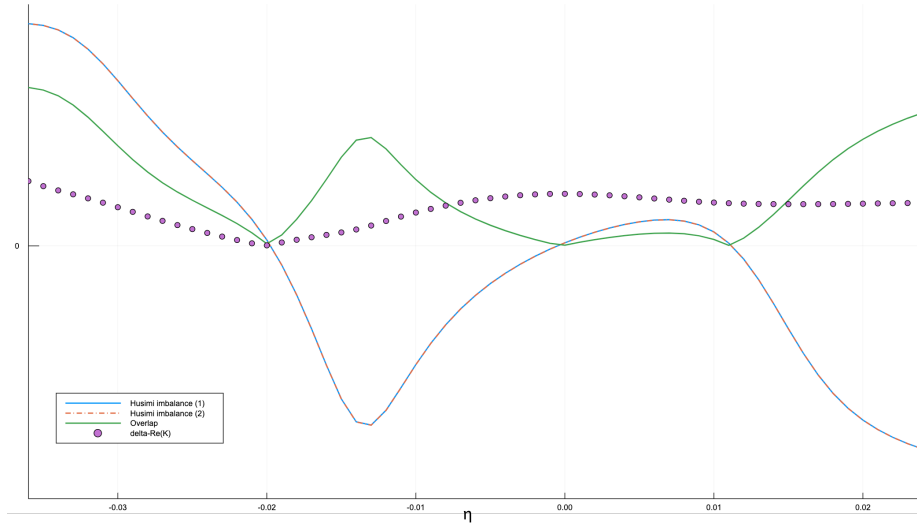


FIGURE 5.10. Combined plot of Husimi imbalance for each mode in the doublet, the mode overlap and difference in wavenumber as a function of deformation parameter  $\eta$

In addition to points of Husimi balance we noticed that deformation away from  $\eta = 0$  can also result in a collapse of the doublet into modes that have a higher amount of overlap. Even though two modes remain at separate wavefunctions, the wavefunctions can coalesce so that the same mode structure is present at both wavenumbers. In this case, the Husimi imbalance also increases so that almost all weight is present in one or other chiral direction. Figure 5.11 shows an example of the resonance followed to a deformation of  $\eta = -0.038$ , here the balance in the Husimi distribution shifts to favor the anti-clockwise chirality in both modes of the doublet. The modes retain a spacing which is comparable to those for  $\eta = 0$ , with a spacing of  $\delta k \simeq (-4.22 - 2.567i)10^{-5}$ . However instead of a wavefunction overlap of approximately 0, the wavefunction overlap approaches unity at overlap  $\simeq 0.87$ . A superposition of the modes reveals an enhancement of the anti-clockwise circulation and a much weaker clockwise component.

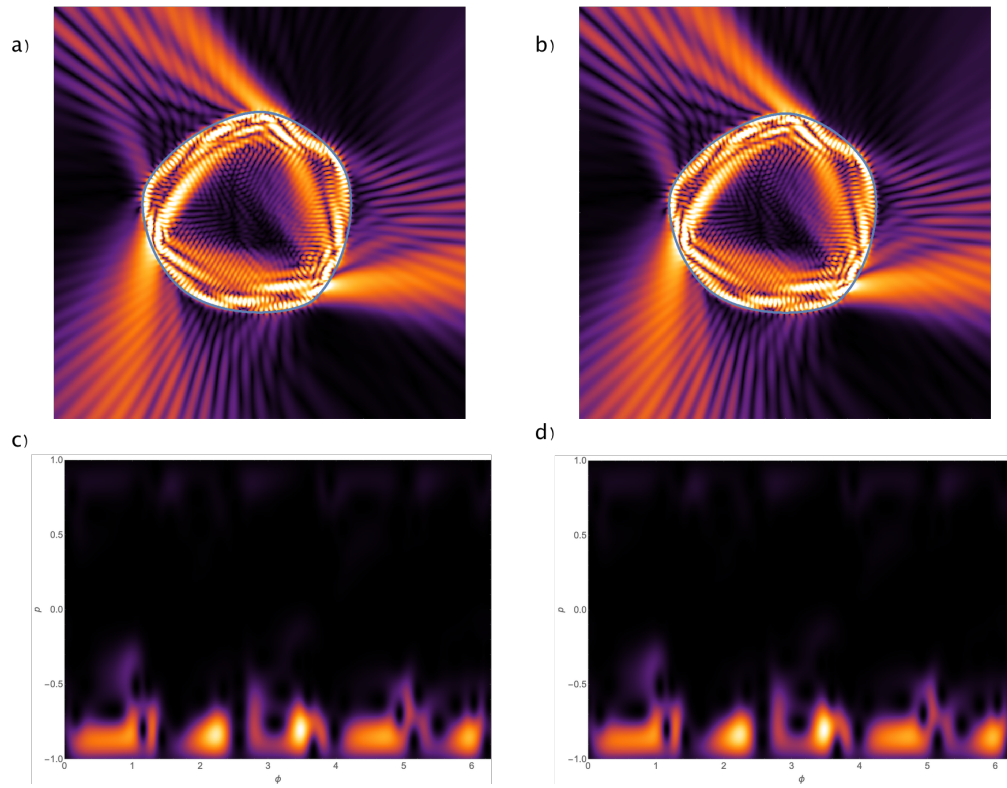


FIGURE 5.11. Wave functions and Husimi distributions for deformed cavity with  $\eta = -0.038$ . Both modes in doublet show increased weight in the anti-clockwise chiral mode.

## 5.6. Spatial Pattern and Far Field Response

As seen in the field plots for the chiral modes, the emission pattern is distinct for the clockwise and anti-clockwise components. This feature distinguishes the constant width billiard from the circle. The circular cavity, as shown in Fig. 2.2, also supports the traveling wave modes with opposite angular momentum. However since the radiation from the cavity is isotropic, there is no way to separate these components. In the case of this geometry, however, the chiral components are emitted at different regions of the boundary. There are locations of high intensity for the clockwise component that have little to no intensity for the anti-clockwise component, and vice versa. This is visible in the near field and is also true in the far field. Figure 5.12 plots the far field response for the clockwise and anti-clockwise modes. This is done using the Green's function approach as for the overall field intensity. This is done at a radius of  $r = 50$  and the field intensities are normalized for comparison with one another. Note that over relatively large angle ranges there are regions of contrast where one chiral mode is approximately 10 times stronger. In smaller angle zones this contrast can be larger. We propose that the constant width geometry and the non-reciprocal response it displays may allow for the separation of left and right circulating waves and the creation of a type of optical "micro-diode". Although in the far field the suppression of the undesired chiral component is only a factor of 10, if the near field output is coupled the suppression may be much larger. The small size of these devices also allows for the possibility of cascaded design, where the suppression factor could be enhanced through multiple stages of cavities, perhaps coupled by waveguides.

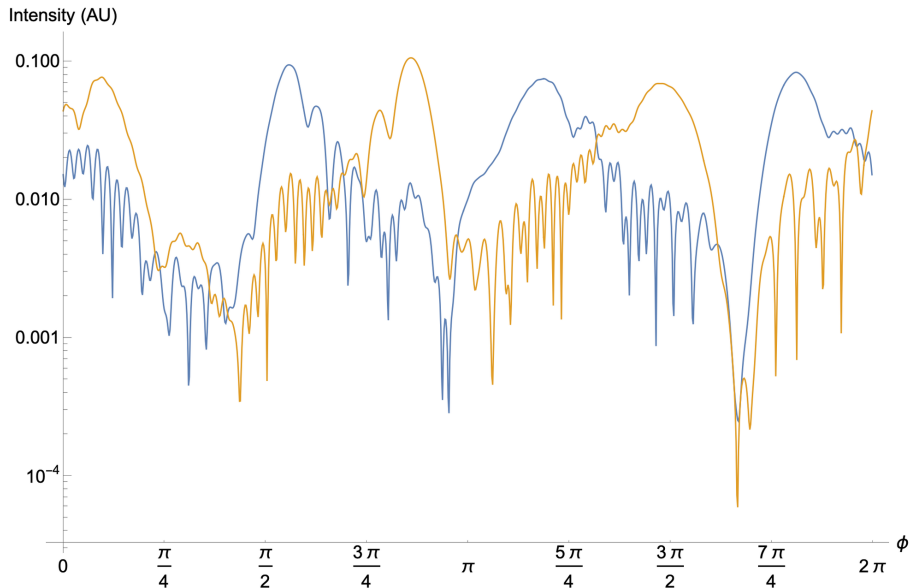


FIGURE 5.12. Far field response for chiral modes in the doublet resonance with  $k \simeq 45.73 - 0.068i$

## 5.7. Conclusion

The constant width boundary has been shown to exhibit non-standard spectral statistics in previous studies of classical billiards and closed microwave cavities. Systems that break time-reversal symmetry have been shown to exhibit eigenvalue spacings that follow the GUE random matrix ensemble. Even though a billiards system has local time evolution which is time-reversal symmetric, the constant width billiard displays global chaotic dynamics which spontaneously break this symmetry. We extend this research into open optical microcavities which allows for understanding the connection between unidirectionality and time-reversal symmetry breaking when coupled to the outside. The general mode families identified in [14] are also found in the open system. We find that the breaking of degenerate modes into quasi-degenerate doublets is also present in the open microcavity.

The conditions for optical non-reciprocity are discussed which at a fundamental level require the breaking of time-reversal symmetry. In the closed systems this requirement is met because there exist time-reversal disconnected regions in the classical phase space [63]. The addition of a index of refraction parameter which can be used to transition from the closed to open system provides the means to probe non-reciprocity generated by purely geometric means. Other mechanisms for the creation of a non-reciprocal optical response involve external magnetic fields, time-dependent media, or optical non-linearities, all of which have some drawbacks. We believe that the ability to produce non-reciprocity through the cavity geometry represents a novel mechanism for separating the chiral components of light and may prove to be useful for the creation of optical micro-diodes which could be an important technology in photonic circuits. The microscopic size of these systems could enable the creation of chip scale optical isolators, in contrast with large scale Faraday rotators that are currently available commercially. The small scale of these cavities allows the potential for a cascaded design which could achieve substantial suppression of counter-propagating light in small spatial regions.

To investigate this phenomenon further, time domain simulations that couple chiral optical modes into and out of these cavities would likely be instructive. An interchange of the source and detector could be made to directly show non-reciprocity in the terms described in [62]. There are also clearly interesting avenues to explore in deforming the constant width cavity, breaking the constant width condition. Initial results show a regime of deformation parameters which reduce the doublet spacing to near zero while retaining a balance of chiral behavior. The extremely narrow mode spacing would allow for an excitation of both doublet modes simultaneously. Further deformation can result in an increase of preferential

chiral circulation. This occurs in contrast to the billiards system where small deformations are shown to destroy the KAM barrier region. The persistence of chiral behavior in the doublets with larger deformations remains unexplained and additional study is warranted.



## CHAPTER VI

### CONCLUSION

The basic properties of optical microcavities have been discussed with an introduction to finding resonances in the simple system of the circular dielectric cavity. This system has a continuous symmetry which conserves angular momentum. Therefore it is integrable and simple analytic solutions may be found in terms of Bessel and Hankel functions. These solutions can be connected to the behavior of a classical system of billiards, where the trajectory of a particle inside a closed boundary is tracked and a projection of the classical phase space onto a Poincaré surface of section demonstrates these solutions as invariant curves with well defined angular momentum. This connection of invariant curves in the SOS with solutions in the wave regime is made and we identify the Husimi distribution as the wave analog to the Poincaré section. The connection between billiards and the resulting wave solutions are part of the methods used in the semi-classical treatment of these systems. In the limit of  $kr \rightarrow \infty$ , the ray approximation becomes valid and closed billiards represent the specular reflection of light within the cavity, as long as the angle of incidence provides for total internal reflection. The critical angle is determined by the index of refraction for the dielectric medium within the cavity.

The circle is one of only a few integrable geometries for the Helmholtz equation, so robust numerical methods are needed to understand the behavior of deformed shapes. The frequency domain method of the boundary integral method is introduced, which uses Green's functions to transform the partial differential equation into an integral equation relating the solution on the boundary

of homogenous regions with the wavefunction at other spatial points. The Green's function acts as the propagator to connect the boundary region with points outside or inside the boundary. For optical microcavities, resonances are defined using boundary conditions for the TE mode where the electric field intensity and its normal derivative are continuous across the boundary and the additional condition of outgoing cylindrical waves at infinity are imposed. Given these conditions the Helmholtz equation may be transformed into a non-linear eigenvalue equation. Since the resonant solutions are quasi-bound modes, a search for a complex wavenumber that provides a non-trivial solution to this matrix equation is needed.

We implement a version of the BIM that has been optimized to guarantee unique solutions free of spurious solutions to the closed Dirichlet boundary conditions and one that mitigates the singularities intrinsic to the integral equations at the origin of the two-dimensional Green's function. Corrections to the original reference and additional details on the derivatives of the resulting matrix equation are given. These are needed for the residual inverse iteration procedure which serves to solve the BIM equations to high precision given a starting estimate of a resonance position. In practice we needed to scan over regions of  $k$ -space to find candidate resonances and use those values as input to the RII procedure. We validate this implementation against known resonance solutions for the circular cavity as well as other deformed cavities and verify the exponential convergence properties as a function of discretization points.

With the tools provided by the BIM implementation, we examined highly deformed concave cavities that demonstrate a new phenomenon which we describe as folded chaotic whispering-gallery modes. These modes exhibit many of the key qualities associated with traditional WGMs but exist within a chaotic region of

phase space and fold over themselves to allow travel over a region of unbounded space within the cavities which can be utilized to attach waveguides. This ability to attach waveguides to a monolithic cavity structure may enable important technological applications as it allows high-Q modes to be coupled to incoming and outgoing light for laser and spectroscopic applications. The high-Q modes exist within certain wavenumber windows and display a peaked spectral structure with successive peaks displaying additional radial nodes similar to the radial nodes in circular WGMs. As an additional validation of the BIM software we use a FDTD method with the arms of the cavity lengthened into the PML region to truly represent the arms as extended waveguides. We find that the resonances identified by the BIM method are easily replicated and display qualitative behavior similar to what is expected from the BIM solutions.

In addition to the waveguide attached folded WGM geometry, we examine smooth boundaries with constant width. These shapes have previously been investigated in billiards and closed microwave cavity settings and intriguing spectral properties consistent with a spontaneous breaking of time-reversal symmetry established. We discuss the connection between the unusual chaotic dynamics in this boundary shape to the unidirectional response of the resonator. We extend these studies by examining optical cavities formed by constant width boundaries. We find that the general mode families identified in the closed cavity [14] are also present in the open system. We discuss the conditions for optical non-reciprocity, which requires time-reversal symmetry breaking as a necessary condition. Examining the doublet modes we find that a superposition of quasi-degenerate modes result in clear chiral modes with weight in one half of the Husimi distribution. The spatial pattern of these modes is distinct depending on chirality.

Both in the near-field and far-field angular separation of these modes is present.

We believe that this cavity shape provides a path towards isolation of chiral modes and technological applications such as optical micro-diodes. We outline some future research directions which could provide further evidence to this claim.

## REFERENCES CITED

- [1] Kerry J. Vahala. Optical microcavities. *Nature*, 424(6950):839–846, 2003. doi: 10.1038/nature01939. URL <https://doi.org/10.1038/nature01939>.
- [2] P. Heider. Computation of scattering resonances for dielectric resonators. *Computers & Mathematics With Applications*, 60(6):1620–1632, September 2010. ISSN 0898-1221. doi: 10.1016/j.camwa.2010.06.044.
- [3] Zhihe Guo, Haotian Wang, Chenming Zhao, Lin Chen, Sheng Liu, Jinliang Hu, Yi Zhou, and Xiang Wu. Spectral modulation of optofluidic coupled-microdisk lasers in aqueous media. *Nanomaterials*, 9(10), 2019. ISSN 2079-4991. doi: 10.3390/nano9101439. URL <https://www.mdpi.com/2079-4991/9/10/1439>.
- [4] E. Noether. Invariante variationsprobleme. *Nachrichten von der Gesellschaft der Wissenschaften zu Göttingen, Mathematisch-Physikalische Klasse*, 1918: 235–257, 1918. URL <http://eudml.org/doc/59024>.
- [5] George B. Arfken, Hans J. Weber, and Frank E. Harris. Chapter 9 - partial differential equations. In George B. Arfken, Hans J. Weber, and Frank E. Harris, editors, *Mathematical Methods for Physicists (Seventh Edition)*, pages 401 – 445. Academic Press, Boston, seventh edition edition, 2013. ISBN 978-0-12-384654-9. doi: <https://doi.org/10.1016/B978-0-12-384654-9.00009-8>. URL <http://www.sciencedirect.com/science/article/pii/B9780123846549000098>.
- [6] R K Chang and A J Campillo. *Optical Processes in Microcavities*. WORLD SCIENTIFIC, 1996. doi: 10.1142/2828. URL <https://www.worldscientific.com/doi/abs/10.1142/2828>.
- [7] Jens U. Nöckel. *Resonances in Nonintegrable Open Systems*. PhD thesis, Yale, 1997.
- [8] George D Birkhoff. *Dynamical systems*. Colloquium publications. American Mathematical Society, Providence, RI, 1927. URL <http://cds.cern.ch/record/2269648>.
- [9] Henri Poincare. *Les methodes nouvelles de la mecanique celeste*. 1892.
- [10] M V Berry. Regularity and chaos in classical mechanics, illustrated by three deformations of a circular 'billiard'. *European Journal of Physics*, 2(2):91–102, apr 1981. doi: 10.1088/0143-0807/2/2/006. URL <https://doi.org/10.1088/0143-0807/2/2/006>.

- [11] George M Zaslavsky. *The physics of chaos in Hamiltonian systems*. Imperial College Press ; Distributed by World Scientific, London : Hackensack, NJ, 2nd ed. edition, 2007. ISBN 1-281-12070-7.
- [12] K. Husimi. Some formal properties of the density matrix. *Proceedings of the Physico-Mathematical Society of Japan. 3rd Series*, 22(4):264–314, 1940. doi: 10.11429/ppmsj1919.22.4\_264.
- [13] Monika A. M. Marte and Stig Stenholm. Paraxial light and atom optics: The optical schrödinger equation and beyond. *Physical Review A*, 56(4): 2940–2953, 1997. ISSN 1050-2947.
- [14] B. Dietz, T. Guhr, B. Gutkin, M. Miski-Oglu, and A. Richter. Spectral properties and dynamical tunneling in constant-width billiards. *Phys. Rev. E*, 90:022903, Aug 2014. doi: 10.1103/PhysRevE.90.022903. URL <https://link.aps.org/doi/10.1103/PhysRevE.90.022903>.
- [15] A Backer, S Furstberger, and R Schubert. Poincare husimi representation of eigenstates in quantum billiards. *Physical Review E*, 70(3), 2004. ISSN 2470-0045.
- [16] Kane Yee. Numerical solution of initial boundary value problems involving maxwell’s equations in isotropic media. *IEEE Transactions on Antennas and Propagation*, 14(3):302–307, May 1966. ISSN 1558-2221. doi: 10.1109/TAP.1966.1138693.
- [17] Ardavan F. Oskooi, David Roundy, Mihai Ibanescu, Peter Bermel, J. D. Joannopoulos, and Steven G. Johnson. Meep: A flexible free-software package for electromagnetic simulations by the fdtd method. *Computer Physics Communications*, 181(3):687–702, 2010. doi: <https://doi.org/10.1016/j.cpc.2009.11.008>. URL <http://www.sciencedirect.com/science/article/pii/S001046550900383X>.
- [18] Vladimir A. Mandelshtam and Howard S. Taylor. Harmonic inversion of time signals and its applications. *The Journal of Chemical Physics*, 107(17): 6756–6769, 1997. doi: 10.1063/1.475324. URL <https://doi.org/10.1063/1.475324>.
- [19] Mark Kac. Can one hear the shape of a drum? *The American Mathematical Monthly*, 73(4):1–23, 1966. ISSN 00029890, 19300972. URL <http://www.jstor.org/stable/2313748>.
- [20] Jan Wiersig. Boundary element method for resonances in dielectric microcavities. *Journal of Optics A: Pure and Applied Optics*, 5(1):53–60, dec 2002. doi: 10.1088/1464-4258/5/1/308. URL <https://doi.org/10.1088%2F1464-4258%2F5%2F1%2F308>.

- [21] Ioan Kosztin and Klaus Schulten. Boundary integral method for stationary states of two-dimensional quantum systems. *International Journal of Modern Physics C*, 08(02):293–325, Apr 1997. ISSN 1793-6586. doi: 10.1142/s0129183197000278. URL <http://dx.doi.org/10.1142/S0129183197000278>.
- [22] S. Prössdorf. Kress, r., linear integral equations. berlin etc., springer-verlag 1989. xi, 299 pp., dm 78,00. isbn 3-540-50616-0 (applied mathematical sciences 82). *ZAMM - Journal of Applied Mathematics and Mechanics / Zeitschrift für Angewandte Mathematik und Mechanik*, 71(12):504–504, 1991. doi: 10.1002/zamm.19910711207. URL <https://onlinelibrary.wiley.com/doi/abs/10.1002/zamm.19910711207>.
- [23] Jeff Bezanson, Alan Edelman, Stefan Karpinski, and Viral B Shah. Julia: A fresh approach to numerical computing. *SIAM Review*, 59(1):65–98, 2017. doi: 10.1137/141000671.
- [24] Jens U. Nöckel and A. Douglas Stone. Ray and wave chaos in asymmetric resonant optical cavities. *Nature*, 385(6611):45–47, 1997. URL <http://dx.doi.org/10.1038/385045a0>.
- [25] Zhao-Pei Liu, Xue-Feng Jiang, Yan Li, Yun-Feng Xiao, Li Wang, Jin-Li Ren, Shi-Jie Zhang, Hong Yang, and Qihuang Gong. High-q asymmetric polymer microcavities directly fabricated by two-photon polymerization. *Applied Physics Letters*, 102(22), JUN 3 2013. ISSN 0003-6951. doi: 10.1063/1.4809724.
- [26] V. F. Lazutkin. *KAM Theory and Semiclassical Approximations to Eigenfunctions*. Springer, New York, 1993.
- [27] C. D. Schwieters, J. A. Alford, and J. B. Delos. Semiclassical scattering in a circular semiconductor microstructure. *Phys. Rev. B*, 54:10652–10668, Oct 1996. doi: 10.1103/PhysRevB.54.10652. URL <https://link.aps.org/doi/10.1103/PhysRevB.54.10652>.
- [28] John N. Mather. Non-existence of invariant circles. 4(2):301–309, 1984. doi: DOI:10.1017/S0143385700002455. URL <https://www.cambridge.org/core/article/nonexistence-of-invariant-circles/F1263804FEA773EA86EC8BE05FD8C3EA>.
- [29] L. A. Bunimovich. On the ergodic properties of nowhere dispersing billiards. *Communications in Mathematical Physics*, 65(3):295–312, 1979. doi: 10.1007/BF01197884. URL <https://doi.org/10.1007/BF01197884>.

- [30] J. U. Nöckel, A. D. Stone, and R. K. Chang. Q spoiling and directionality in deformed ring cavities. *Opt. Lett.*, 19(21):1693–1695, 1994. URL <http://ol.osa.org/abstract.cfm?URI=ol-19-21-1693>.
- [31] S. A. Backes, J. R. A. Cleaver, A. P. Heberle, and K. Kohler. Microdisk laser structures for mode control and directional emission. volume 16, pages 3817–3820. AVS, 1998. doi: 10.1116/1.590415. URL <http://link.aip.org/link/?JVB/16/3817/1>.
- [32] Xiao-Meng Lv, Yong-Zhen Huang, Yue-De Yang, Heng Long, Ling-Xiu Zou, Qi-Feng Yao, Xin Jin, Jin-Long Xiao, and Yun Du. Analysis of vertical radiation loss and far-field pattern for microcylinder lasers with an output waveguide. *Opt. Express*, 21(13):16069–16074, Jul 2013. doi: 10.1364/OE.21.016069. URL <http://www.opticsexpress.org/abstract.cfm?URI=oe-21-13-16069>.
- [33] Bing-Jing Li and Pao-Lo Liu. Analysis of far-field patterns of microdisk resonators by the finite-difference time-domain method. *IEEE Journal of Quantum Electronics*, 33(9):1489–1491, 1997. doi: 10.1109/3.622627.
- [34] Changling Yan, Jianwei Shi, Peng Li, Hui Li, and Jianjia Zhang. Limacon-shaped micro-cavity lasers with directional emission and its performance. *Optics and Laser Technology*, 56:285–289, MAR 2014. ISSN 0030-3992. doi: 10.1016/j.optlastec.2013.08.009.
- [35] Qinghai Song, Li Ge, Brandon Redding, and Hui Cao. Channeling chaotic rays into waveguides for efficient collection of microcavity emission. *Physical Review Letters*, 108(24), JUN 15 2012. ISSN 0031-9007. doi: 10.1103/PhysRevLett.108.243902.
- [36] Shuai Liu, Wenzhao Sun, Yujie Wang, Xiaoyi Yu, Ke Xu, Yongzhen Huang, Shumin Xiao, and Qinghai Song. End-fire injection of light into high-q silicon microdisks. *Optica*, 5(5):612–616, May 2018. doi: 10.1364/OPTICA.5.000612. URL <http://www.osapublishing.org/optica/abstract.cfm?URI=optica-5-5-612>.
- [37] Yue-De Yang, Yu Zhang, Yong-Zhen Huang, and Andrew W. Poon. Direct-modulated waveguide-coupled microspiral disk lasers with spatially selective injection for on-chip optical interconnects. *Optics Express*, 22(1): 824–838, JAN 13 2014. ISSN 1094-4087. doi: 10.1364/OE.22.000824.
- [38] Kai-Jun Che, Jian-Dong Lin, Yong-Zhen Huang, Yue-De Yang, Jin-Long Xiao, and Yun Du. Ingaasp-inp square microlasers with a vertex output waveguide. *IEEE Photonics Technology Letters*, 22(18):1370–1372, SEP 15 2010. ISSN 1041-1135. doi: 10.1109/LPT.2010.2057417.



- [39] Huang YongZhen, Yang YueDe, Wang ShiJiang, Xiao JinLong, Che KaiJun, and Du Yun. Whispering-gallery microcavity semiconductor lasers suitable for photonic integrated circuits and optical interconnects. *SCIENCE IN CHINA SERIES E-TECHNOLOGICAL SCIENCES*, 52(12):3447–3453, DEC 2009. ISSN 1006-9321. doi: 10.1007/s11431-009-0306-y.
- [40] L. Zou, X. Lv, Y. Huang, H. Long, J. Xiao, Q. Yao, J. Lin, and Y. Du. Mode analysis for unidirectional emission alginas/inp octagonal resonator microlasers. *IEEE Journal of Selected Topics in Quantum Electronics*, 19(4): 1501808–1501808, 2013. doi: 10.1109/JSTQE.2013.2244566.
- [41] Takehiro Fukushima, Tomoko Tanaka, and Takahisa Harayama. High-quality lowest-loss-mode lasing in gaas quasi-stadium laser diodes having unstable resonators. *Opt. Lett.*, 32(23):3397–3399, 2007. URL <http://ol.osa.org/abstract.cfm?URI=ol-32-23-3397>.
- [42] R. E. Prange, R. Narevich, and O. Zaitsev. Quantum spectra and wave functions in terms of periodic orbits for weakly chaotic systems. *Physica Scripta*, T90:134–141, 2001. URL <http://stacks.iop.org/1402-4896/T90/134>.
- [43] Claire Gmachl, Federico Capasso, E. E. Narimanov, Jens U. Nöckel, A. Douglas Stone, Jerome Faist, Deborah L. Sivco, and Alfred Y. Cho. High-power directional emission from microlasers with chaotic resonators. *Science*, 280(5369):1556–1564, 1998. doi: 10.1126/science.280.5369.1556. URL <http://www.sciencemag.org/content/280/5369/1556.abstract>.
- [44] V. M. Babic and V. S. Buldyrev. *Short-wavelength diffraction theory*. Springer Verlag, Berlin, 1972.
- [45] M. Fernández Guasti. Analytic geometry of some rectilinear figures. *International Journal of Mathematical Education in Science and Technology*, 23(6):895–913, November 1992.
- [46] Fabian Lackner, Iva Brezinova, Joachim Burgdoerfer, and Florian Libisch. Semiclassical wave functions for open quantum billiards. *Phys. Rev. E*, 88(2), AUG 19 2013. doi: 10.1103/PhysRevE.88.022916.
- [47] J. U. Nöckel and A. D. Stone. Chaotic light: a theory of asymmetric cavity resonators. In R. K. Chang and A. J. Campillo, editors, *Optical Processes in Microcavities*. World Scientific, Singapore, 1996.

- [48] V. A. Mandelshtam. Fdm: the filter diagonalization method for data processing in nmr experiments. *Progress in Nuclear Magnetic Resonance Spectroscopy*, 38(2):159–196, 3 2001. doi: [http://dx.doi.org/10.1016/S0079-6565\(00\)00032-7](http://dx.doi.org/10.1016/S0079-6565(00)00032-7). URL <http://www.sciencedirect.com/science/article/pii/S0079656500000327>.
- [49] A. J. Lichtenberg and M. A. Lieberman. *Regular and Chaotic Dynamics, Second Edition*. Springer-Verlag, New York, 1992.
- [50] J. U. Nöckel and R. K. Chang. 2-d microcavities: Theory and experiments. In R. D. van Zee and J. P. Looney, editors, *Cavity-Enhanced Spectroscopies*, volume 40 of *Experimental Methods in the Physical Sciences*, pages 185–226. Academic Press, San Diego, 2002.
- [51] Jan Wiersig. Formation of long-lived, scarlike modes near avoided resonance crossings in optical microcavities. *Phys. Rev. Lett.*, 97:253901, Dec 2006. doi: 10.1103/PhysRevLett.97.253901. URL <https://link.aps.org/doi/10.1103/PhysRevLett.97.253901>.
- [52] Hui Cao and Jan Wiersig. Dielectric microcavities: Model systems for wave chaos and non-hermitian physics. *Reviews of Modern Physics*, 87(1):61–111, 01 2015. doi: 10.1103/RevModPhys.87.61. URL <https://link.aps.org/doi/10.1103/RevModPhys.87.61>.
- [53] David H. Foster, Andrew K. Cook, and Jens U. Nöckel. Goos-hänchen induced vector eigenmodes in a dome cavity. *Opt. Lett.*, 32(12):1764–1766, 2007.
- [54] Julia Unterhinninghofen, Jan Wiersig, and Martina Hentschel. Goos-hänchen shift and localization of optical modes in deformed microcavities. *Phys. Rev. E*, 78:016201, Jul 2008. doi: 10.1103/PhysRevE.78.016201. URL <https://link.aps.org/doi/10.1103/PhysRevE.78.016201>.
- [55] G. Hackenbroich and J. U. Nöckel. Dynamical tunneling in optical cavities. *EPL (Europhysics Letters)*, 39(4):371–376, 1997. URL <http://stacks.iop.org/0295-5075/39/371>.
- [56] M. Brack and R. K. Bhaduri. *Semiclassical Physics*. Westview Press, Boulder, Co., 2003.
- [57] M. Brack, R. K. Bhaduri, J. Law, and M. V. N. Murthy. Quantum beats and chaos in the h enon-heiles hamiltonian. *Phys. Rev. Lett.*, 70:568–571, Feb 1993. doi: 10.1103/PhysRevLett.70.568. URL <https://link.aps.org/doi/10.1103/PhysRevLett.70.568>.

- [58] Hiromu Ishio, Alexander I. Saichev, Almas F. Sadreev, and Karl-Fredrik Berggren. Wave function statistics for mesoscopic transport through chaotic open billiards: time reversibility, space reciprocity breaking and statistical crossover. *Computer Physics Communications*, 142(1):64–70, 2001. doi: [https://doi.org/10.1016/S0010-4655\(01\)00320-4](https://doi.org/10.1016/S0010-4655(01)00320-4). URL <http://www.sciencedirect.com/science/article/pii/S0010465501003204>.
- [59] Oliver Knill. On nonconvex caustics of convex billiards. *Elemente der Mathematik*, 53(3):89–106, 1998. doi: 10.1007/s000170050038. URL <https://doi.org/10.1007/s000170050038>.
- [60] C. Dembowski, H.-D. Gräf, A. Heine, R. Hofferbert, H. Rehfeld, and A. Richter. First experimental evidence for chaos-assisted tunneling in a microwave annular billiard. *Phys. Rev. Lett.*, 84:867–870, Jan 2000. doi: 10.1103/PhysRevLett.84.867. URL <https://link.aps.org/doi/10.1103/PhysRevLett.84.867>.
- [61] R J Potton. Reciprocity in optics. *Reports on Progress in Physics*, 67(5): 717–754, apr 2004. doi: 10.1088/0034-4885/67/5/r03. URL <https://doi.org/10.1088/0034-4885/67/5/r03>.
- [62] Christophe Caloz, Andrea Alù, Sergei Tretyakov, Dimitrios Sounas, Karim Achouri, and Zoé-Lise Deck-Léger. Electromagnetic nonreciprocity. *Phys. Rev. Applied*, 10:047001, Oct 2018. doi: 10.1103/PhysRevApplied.10.047001. URL <https://link.aps.org/doi/10.1103/PhysRevApplied.10.047001>.
- [63] Boris Gutkin. Dynamical ‘breaking’ of time reversal symmetry. *Journal of Physics A: Mathematical and Theoretical*, 40(31):F761–F769, jul 2007. doi: 10.1088/1751-8113/40/31/f02. URL <https://doi.org/10.1088/1751-8113/40/31/f02>.
- [64] O. Bohigas, M. J. Giannoni, and C. Schmit. Characterization of chaotic quantum spectra and universality of level fluctuation laws. *Phys. Rev. Lett.*, 52:1–4, Jan 1984. doi: 10.1103/PhysRevLett.52.1. URL <https://link.aps.org/doi/10.1103/PhysRevLett.52.1>.